NEAR-SOURCE IMAGING OF SEISMIC RUPTURE

BY

GREGORY CHRISTIAN BEROZA

B.S., UNIVERSITY OF CALIFORNIA AT SANTA CRUZ (1982)

SUBMITTED TO THE DEPARTMENT OF
EARTH, ATMOSPHERIC, AND PLANETARY SCIENCES
IN PARTIAL FULFILLMENT OF THE REQUIREMENTS
FOR THE DEGREE OF

DOCTOR OF PHILOSOPHY

AT THE

MASSACHUSETTS INSTITUTE OF TECHNOLOGY
APRIL 1989

SIGNATURE OF AUTHOR _____
DEPARTMENT OF EARTH, ATMOSPHERIC, AND PLANETARY SCIENCES

CERTIFIED BY _____
THOMAS H. JORDAN
THESIS SUPERVISOR

ACCEPTED BY _____
THOMAS H. JORDAN
CHAIRMAN, DEPARTMENT COMMITTEE

NEAR-SOURCE IMAGING OF SEISMIC RUPTURE

by

GREGORY CHRISTIAN BEROZA

Submitted to the Department of Earth, Atmospheric, and Planetary Sciences
on April 19, 1989 in partial fulfillment of the requirements
for the Degree of Doctor of Philosophy

ABSTRACT

The nature of failure in earthquakes is one of the most fundamental questions in geophysics. We approach this problem using near-source seismic recordings of strong-ground motion to image the rupture process of earthquakes. We apply the technique to three well-recorded earthquakes in California and interpret the results in terms of earthquake rupture dynamics.

To calculate theoretical seismograms we use a high-frequency, near-source approximation that allows the use of geometrical ray theory at distances greater than a wavelength. This approach has several advantages. It is several orders of magnitude faster than techniques that use complete Green's functions. This increase in speed allows us to parameterize the rupture process differently than most previous studies. Ray theory also allows us to include the effects of smooth, laterally-varying structure on near-source seismograms. We have developed the capability to do this using dynamic ray tracing and have applied it to a simple, idealized, fault-zone model.

We parameterize the seismic source as a distributed displacement discontinuity across a planar fault that slips only once, when the rupture front passes, with a spatially varying rupture time and slip intensity. This parameterization results in a nonlinear relation between the observed seismograms and the faulting model. We perform a linearization of the problem and solve the nonlinear inverse problem by iteratively perturbing an assumed starting model. The inversion is performed using a regularized, back-projection technique. The resolution of the method is analyzed using sensitivity tests.

The technique is applied to the 1966 Parkfield earthquake, the 1979 Imperial Valley earthquake, and the 1984 Morgan Hill earthquake. In each of these earthquakes there is evidence for strong heterogeneity in the slip amplitude. In the case of the Imperial Valley and Morgan Hill earthquakes, where the data are sufficient to distinguish between variations in slip amplitude and variations in rupture time, there is evidence for strong heterogeneity in the rupture velocity as well as the slip amplitude.

The observed heterogeneity in the rupture process is attributable to heterogeities in the stress and strength. In the case of the Morgan Hill and Parkfield earthquakes there are features evident in the surface trace of the fault and in the distribution of seismicity with depth that are plausibly related to the large-scale heterogeneities in the rupture process. In the case of the Imperial valley earthquake the relation between large-scale heterogeneity and fault zone structure is less clear.

We also find indirect evidence for complexity of the faulting process at much smaller length-scales. Our estimates of the shear fracture energy in these earthquakes ranges from 5-20 $\times 10^5$ J/m^2. This is several orders of magnitude higher than found for laboratory samples of a simple fracture. The greatly increased surface area of a complex earthquake rupture may account for the high apparent shear fracture energies that we find.

Thesis Committee:

Dr. Thomas H. Jordan	Thesis Supervisor
Dr. Theodore R. Madden	
Dr. M. Nafi Toksöz	
Dr. Vernon Cormier	University of Connecticut at Storrs
Dr. Teng-fong Wong	State University of New York at Stonybrook

ACKNOWLEDGMENTS

I have much to be thankful for and many people to thank. Rob McCaffrey fueled my initial interest in seismology. Soon after Karen McNally provided the opportunity for an unproven, undergraduate physics major to set up an array of seismic instruments in Guerrero. Jose Rial introduced me to strong-motion seismology. The group of graduate students at U.C. Santa Cruz made me eager to go to graduate school myself.

At MIT I have been fortunate to get a solid education and to have the freedom to follow my research interests. A number of people have had a strong, positive impact on my graduate education. Tom Jordan has provided scientific acumen, fascinating research topics, and along with his wife Robin has hosted numerous parties. Both Tom and Bernard Minster gave patient tutorials on inverse theory while we worked on the analysis of space-geodetic data. I have enjoyed working with Vernon Cormier and have benefitted greatly from his seemingly limitless knowledge of the more arcane aspects of wave propagation. Nafi Toksöz is always interested in my work and freely offers his sage advice. I have also benefitted from discussions of various aspects of inverse theory with Ted Madden. Teng-fong Wong provided a good perspective on this thesis based on his expertise in fracture mechanics and made a number of useful comments.

At the U.S. Geological Survey, Paul Spudich–my advisor *in absentia*–has been an outstanding mentor. Many of the ideas developed in this thesis have their origins in conversations with him. His humble exactitude and low humor have both been at once inspiring and unbearable.

I have had the good fortune to know a number of talented and friendly graduate students while at MIT. Mike Prange shared an office with me at ERL and helped me to get around on the computer system there. Kiyoshi Yomogida shared his infectious enthusiasm for all aspects of seismology. I enjoyed working with Jeanne Sauber on aspects of continental tectonics and the analysis of VLBI data. Interactions with Karen Fischer and Steve Hickman

were enjoyable, but too infrequent. I was fortunate to have Karen's thesis as a guide for preparing my own.

John Goff and Peter Puster provided eager golfing partners. Anne Sheehan helped with low-frequency moment tensors and three-point shots. Eugene Lavely always had interesting questions that I couldn't answer. Kurt Feigl cheerfully organized weekly forays for Chinese food. Mike Bergman was the good-humored butt of innumerable jokes. Carolyn Ruppel injected a refreshing overabundance of raw energy into the department.

The people who have had the greatest impact on my graduate school education have been my penecontemporaries on the fifth floor. Bob Grimm lent his cosmic perspective to terrestial geophysics. Lind Gee was always helpful and provided scientific and moral support. Lind's mother, Barbara Gee, has provided a steady stream of simple carbohydrates that kept my afternoons productive. Justin Revenaugh provided inspiration in his surly, but overwhelmingly competent approach to scientific problems and computer recreation. I've enjoyed philosophizing and working on the network adjustment problem with Mark Murray.

Dave Krowitz made this research possible by keeping the geophysical computing facility running smoothly and by patiently answering my many questions. I am also grateful to a number of people for grappling with MIT bureaucracy on my behalf. They include: Debbie Roecker, Sara Brydges, Sharon Feldstein, Donna Martel, Susan Guralnik, Jan Sahlstrom, and more recently Katherine Ware and Marie Sénat.

I would like to thank my parents and family for their constant love and support and for the confidence they have instilled in me. Finally I thank Eva Huala for her unconditional love. She has made this endeavour worthwhile.

TABLE OF CONTENTS

CHAPTER 1

INTRODUCTION

A principal goal of seismology is to infer properties of the seismic source from observations of seismic waves. A more complete description of seismic sources will lead to an increased understanding of earthquake occurrence, which is of more than academic interest. During the 20th century earthquakes have killed nearly two million people. These losses will doubtless increase rapidly as the Earth's explosive population growth leads to increasingly dense development of earthquake-prone regions [*Bilham et al.*, 1989]. In California alone, an earthquake on the Newport-Inglewood fault near Los Angeles has the potential to cause up to 23,000 deaths and $45 billion in damage to buildings [*FEMA*, 1981]. Estimates of death and destruction resulting from a repeat of the 1906 earthquake on the San Andreas fault or a large event in the New Madrid region are comparable [*Hays*, 1981]. Prediction of the time and place at which such earthquakes will happen is an obvious way to mitigate these losses; however, the goal of reliable earthquake prediction remains elusive.

While it is not necessarily true that earthquakes will be rendered predictable by an increased understanding of the dynamics of seismic sources, it is reasonable to expect that such an understanding will be very useful in developing forecast models. In this thesis I develop a new technique for analyzing near-source records of earthquakes, apply it to three moderate earthquakes in California, and from the results attempt to constrain the controlling influences on earthquake rupture dynamics.

A more direct and immediate benefit of understanding earthquake rupture is the ability to better anticipate the severity of strong ground motion in areas of known seismic risk. In socio-economic terms, this is one of the most important problems that seismologists can answer. It is arguably as important to predict the probable effects of an earthquake in

earthquake-prone regions and to design structures that will withstand them, as it is to predict the precise time and place of occurrence.

The fundamental groundwork for the problem of inferring the nature of earthquake rupture from seismic records of ground motion was not firmly established until the early 1960's when *Maruyama* [1963] and *Burridge and Knopoff* [1964] correctly expressed the body-force equivalent of a dislocation. The representation theorem derived in these papers expresses the displacement as a function of space and time resulting from a displacement discontinuity in a general elastic medium by a convolution of a Green's function with a slip function. This concept was generalized by *Backus and Mulcahey* [1976*a*,*b*] to more general seismic sources.

To study earthquake sources, seismologists compare theoretical ground motion, calculated using the representation theorem, with observed seismograms. Thus, the study of the seismic source can be considered to consist of several tasks: calculation of accurate Green's functions to use in the representation theorem, determination of the seismic source behavior from a comparison of theoretical seismograms with observed seismograms, and inference of the physics of earthquake rupture from these observations. Each of these problems is poorly-posed in isolation. A better understanding of any one of them will result in a better understanding of the others.

Calculation of Green's Functions

A great deal of effort has gone into calculating Green's functions and modeling earthquake sources at teleseismic distances [e.g., *Nabelek*, 1984; *Dziewonski and Woodhouse*, 1985] where the Fraunhofer approximation is valid for body waves [*Aki and Richards*, 1980*b*; *Choy and Boatwright*, 1981]. Although the forward problem of calculating theoretical seismograms at teleseismic distances for an assumed faulting model is fairly well understood, the potential resolution of earthquake rupture behavior using far-source observations is limited by interference of waves propagating from different parts of

the fault. In the near-source region, where the Fraunhofer approximation does not apply, the potential resolution is much greater than in the far-source region; however, the inference of earthquake source properties from near-source seismic data is more difficult. There are also complications due to the importance of near-field terms in elastic Green's functions within a few wavelengths of the source.

The calculation of near-source seismograms has not received nearly as much attention as the calculation of far-source seismograms over the past 20 years, but it has seen steady progress. In this section we briefly review the development of increasingly sophisticated methods for calculating Green's functions. For a more exhaustive review of available techniques see *Aki* [1982] and *Spudich and Archuleta* [1987].

Early near-source studies used Green's functions appropriate for an infinite whole space and attempted to correct for the effect of the free surface by using an image source. *Aki* [1968] and *Haskell* [1969] modeled a near-source record of the 1966 Parkfield earthquake using such an approach. The single seismogram studied by these authors was located approximately 80 meters from the surface trace of the fault and the simple pulse-like nature of the transverse component of motion (perpendicular to the fault) was adequately explained by the wholespace model.

More recent studies have used multi-component data from more than one station and, for the more general source-receiver geometries encountered, were compelled to use methods developed for calculating complete Green's functions that include the effects of the free surface and vertical heterogeneity. It wasn't until the mid-1970's that the effect of the free surface on complete near-source seismograms was included [*Niazy*, 1975; *Kawasaki*, 1975]. The effects of vertical heterogeneity were included soon after [*Heaton and Helmberger*, 1977; *Swanger and Boore*, 1978].

The effects of lateral velocity variations on near source seismograms have also received some attention. Several authors have used high-frequency approximations to study the effects of lateral heterogeneity on ground motion from a nearby fault [*Hong and Helmberger*,

1978; *Cormier and Spudich*, 1984; *Cormier and Beroza*, 1987; *Cerveny et al.* 1987]. Finite-difference seismograms have been used to study near-source records of the San Fernando earthquake [*Vidale and Helmberger*, 1988].

A different approach uses small earthquakes as empirical Green's functions [*Hartzell*, 1978]. In this technique small earthquakes are used to determine the response of the Earth to a dislocation below the corner frequency of the small event. By superposition, the response of the Earth to a much larger earthquake can be determined.

All techniques, except those using empirical Green's functions, calculate either exact Green's functions in idealized, laterally-homogeneous Earth models or calculate approximate Green's functions in somewhat more realistic Earth models. Methods based on empirical Green's functions require assumptions of their own: that the mechanism in the smaller event is well known, and that Green's functions from regions of the fault where there were no earthquakes can be determined from parts of the fault where empirical Green's functions are available.

Inferring Seismic Source Behavior

No matter what the techique used for calculating Green's functions, the seismologist is faced with the task of matching an inconsistent, incomplete data set with an imperfect forward model of the effects of faulting on the radiated elastic field. In such a situation the meaningful inference of seismic source behavior is a difficult problem.

It was stated earlier that the resolution of earthquake rupture behavior using far-source observations is limited by interference effects. This results from the fact that in the Fraunhoffer approximation, which is valid at teleseismic differences, the only difference in the propagation of seismic waves from different parts of the fault is a difference in time. The deleterious effect of this fact on resolution could be improved somewhat if it were possible to model high-frequency waves recorded at teleseismic distances. However, the effects of small-scale heterogeneity and attenuation on high-frequency waves, which travel great

distances through the Earth before being recorded, limit the frequency band in which teleseismic data can be used. The effect of this limitation on source modeling is that the short-scale length features of the rupture history of an earthquake can not be recovered [*Aki and Richards*, 1980*b*]. To resolve the seismic source in any detail for all but the very largest earthquakes, it is necessary to use data from the near-source region.

In the near-source region, seismic waves travel very short distances. This substantially reduces the effects of lateral heterogeneities and attenuation on the seismogram. Moreover, waves generated on different parts of the fault are quite different in character and have the potential to resolve greater details of the rupture behavior. On the other hand the wave propagation problem is more complex due to the presence of near-field terms in the Green's functions. The principal obstacle to progress in using near-source records for studying earthquake source behavior; however, is that they are available in sufficient quantity for only a very few earthquakes.

Initial attempts to characterize earthquake rupture from near-source data began by modeling simple earthquake sources characterized by a small number of parameters. *Aki* [1968] and *Haskell* [1969] modeled the 1966 Parkfield earthquake with a simple five-parameter fault model that consisted of the length and vertical extent of the rupture zone, the speed of rupture propagation, and the amount of constant relative offset of the two sides of the fault. *Trifunac and Udwadia* [1974] modeled the same earthquake using least-squares fitting of waveforms to model the direction and magnitude of slip on the fault. *Trifunac and Udwadia* [1974] found it necessary to invoke a non-uniform slip distribution for the Parkfield earthquake to account for observations from different near-source stations.

More recent work on the inverse problem for rupture history on a finite fault has concentrated on the extensive data set generated by the 1979 Imperial Valley earthquake. [*Hartzell and Helmberger*, 1982; *Olson and Apsel*, 1982; *Hartzell and Heaton*, 1983; *Archuleta*, 1984]. Two of these studies [*Hartzell and Helmberger*, 1982; *Archuleta*, 1984] used trial-and-error modeling of near-source seismograms to infer the rupture history and the

other two studies [*Olson and Apsel*, 1982; *Hartzell and Heaton*, 1983] solved a linear inverse problem for the slip distribution.

The results obtained in modeling earthquake rupture are dependent on the initial assumptions and parameterization of the rupture history. In modeling the Imperial Valley earthquake *Olson and Apsel* [1982] and *Hartzell and Heaton* [1983] parameterized the fault as slipping within an assumed time window, but with variable slip amplitude. If the time of rupture is assumed, the relation between slip amplitude on the fault and the observed seismogram is linear. *Archuleta* [1984] parameterized the Imperial and Brawley faults as slipping only once at each point with variable slip amplitude, rupture time, and rise time. Once rupture time and rise time are allowed to be free parameters, the inverse problem becomes nonlinear. As *Archuleta* [1984] points out, the effect of changing rupture time has a very strong effect on the ground motion.

Recently, *Fukuyama and Irikura* [1986] and *Takeo* [1987] have presented linearized inversions for fault rupture parameterized by variable slip and rupture time for the Akita-Oki and Naganoken-Seibu earthquakes. Both methods assign a finite prior covariance to the values of the model parameters and specify the mode of rupture propagation within a series of subfaults that span the ruptured fault surface.

In modeling earthquake rupture the number of unknowns is typically fewer than the number of data. However, because the data are not all linearly independent, the problem is typically underdetermined. In such a situation it is essential to use prior information to constrain the infinite number of possible models. Such prior information can take several forms.

In the case of earthquake faulting prior information can include the direction of relative slip on the fault based on independent evidence such as global plate motion models, teleseismic fault plane solutions, previous observations of fault slip, or geodetic observations of coseismic strain. Constraints on the extent of faulting and the orientation of the fault plane can be obtained by the extent of the surface faulting or the extent of the aftershock zone. In

addition, the location of the earthquake hypocenter provides an initial estimate of the point of rupture nucleation.

Another class of assumptions concerns properties of the derived rupture model. Assuming that the solution be as simple as possible while still maintaining a satisfactory fit to the data is an example of such an assumption. Typically, such constraints amount to minimizing a norm that defines some measure of solution complexity. Such a norm might measure the absolute amount of slip or the size of the difference of slip amplitude on adjacent segments of the fault.

The method for inferring earthquake rupture behavior presented in this thesis is somewhat different from previous studies. We allow the slip amplitude and rupture time to vary over the fault. The resulting problem is nonlinear, and we set up the inverse problem by linearizing with respect to rupture time. The initial rupture model is smooth with very low amplitude. The subsequent model perturbations to the linearized system of equations are constrained to be smooth. The result is a rupture model that is smooth except where required by the data to be rapidly varying.

Another aspect of our modeling procedure that differs from all previous studies is that we do not decompose the total fault plane into subfaults in which the rupture front propagates in a prescribed direction. Instead we specify the time of rupture front passage by a grid of points that spans the fault plane. The result is that directivity effects are properly incorporated since the direction of rupture propagation is a derived rather than assumed quantity. Other methods have assumed the direction of rupture propagation within a subfault *a priori*. As we shall see the local direction of rupture propagation on the fault derived from our modeling is one of the most interesting aspects of earthquake rupture. Our parameterization also has the advantage of decreasing the number of model parameters in a physically plausible way, which will decrease the degree of non-uniqueness.

The resulting inverse problem for fault rupture history is of quite large dimension. The large size of the problem is compounded by the fact that rupture time is nonlinearly related to

the seismogram. The linearized approximation requires incremental perturbations to an assumed starting model so that the inversion must be performed a number of times. It also means that inversions with many different starting models should be performed in order to avoid local minima. The compute-intensive nature of the problem motivates us to use an iterative back-projection technique to calculate the perturbation to the rupture model. Sparse matrix techniques also helped to enhance performance.

We apply the linearized inversion method to the available near-source data for three earthquakes in California: the 1966 Parkfield earthquake, the 1979 Imperial Valley earthquake, and the 1984 Morgan Hill earthquake.

The Dynamics of Earthquake Rupture

Most earthquakes are thought to consist of distributed displacement discontinuities across fault surfaces. Kinematic studies of the seismic source determine the distribution of slip and rupture time on the fault surface without considering the forces that drive the rupture. Kinematic faulting models can fit the data with a rupture model that may be physically implausible. Dynamic models of earthquake rupture consider the forces that are driving rupture, but usually assume highly-idealized fault geometries. Moreover, since the conditions in the Earth are not well known, the boundary or initial conditions for dynamic rupture modeling are uncertain.

The approach we adopt is to model the seismic source kinematically with as few restrictive assumptions as possible, but to take dynamic considerations into account while posing the inverse problem and interpreting the results. We then use the results to infer general properties of earthquake rupture and to place constraints on parameters that are directly relevant to a more complete description of earthquakes.

We attempt to infer properties of the earthquake source in the framework of the slip-weakening model of fracture mechanics. If this is a realistic model of the seismic source and if we can reliably determine the parameters such as the shear fracture energy and the size of

the slip-weakening zone for earthquakes, then we can use these parameters to address important questions such as the severity of ground motion at high frequencies and the size of preseismic nucleation zones.

In addition to direct inference of source properties, we can compare the rupture models obtained with known properties of the source region to infer what properites of fault zones control seismic rupture. For example the variation of rheological properties with depth should have an effect on seismic rupture. Fault zone geometry can also affect the evolution of seismic faulting. The comparison of our faulting models with the occurrence of smaller events, both aftershocks and events during the interseismic period, places additional constraints on the nature of seismic rupture, and the accumulation and release of strain energy during the seismic cycle.

CHAPTER 2

CALCULATING THEORETICAL SEISMOGRAMS

To infer the behavior of an earthquake source from records of ground motion it is first necessary to solve the forward problem–to calculate theoretical seismograms for a hypothetical earthquake. Ideally it would be desirable to calculate theoretical seismograms for the true geologic structure in which an earthquake occurs; however, since we have only a very approximate idea of the true geologic structure, we can only calculate approximate seismograms. Moreover, even if we knew the structure exactly, calculation of exact seismograms in a complicated three-dimensional medium is a daunting computational task. In this chapter the method used to calculate theoretical seismograms is presented. Several approximations are made in the process to render the problem tractable. Our development is cursory. For more detailed developments see *Aki* [1982] and *Spudich and Archuleta* [1987].

The Representation Theorem

The first step in calculating theoretical seismograms is the representation theorem, which relates the observed ground motion to the parameters that describe the seismic source. *Backus and Mulcahy* [1976a,b] present a general form of the representation theorem for the displacement due to volume and surface sources. The vector displacement $\mathbf{u}$ as a function of position $\mathbf{x}$ and time t due to the stress glut Γ_{ij} acting at position ξ is

$$\mathbf{u}(\mathbf{x},t) = \int_{-\infty}^{\infty} dt' \int dV(\xi)\, \Gamma_{ij}(\xi,t)\, \mathbf{G}_{i,j}(\mathbf{x},t-t',\xi,0) \qquad (2.1)$$

where $\mathbf{G}_i(\mathbf{x},t-t',\xi,0)$ is the point source Green's function: the vector displacement at position $\mathbf{x}$ and time $t-t'$, due to an instantaneous force of unit impulse at time $t=0$ applied in the i^{th} direction at position ξ, and a comma denotes the partial derivative, i.e., $\mathbf{G}_{i,j} = \partial \mathbf{G}_i / \partial x_j$.

The stress glut Γ_{ij} is a general description of the seismic source and is defined as the difference between the model stress and the actual physical stress in the Earth. The stress glut is nonzero only in regions of inelastic deformation.

We choose to approximate earthquakes as distributed displacement discontinuities across planar fault surfaces. This is an idealization that is adequate provided the width of the zone of inelastic deformation is very much smaller than the lateral and depth extent of faulting. For this special case of an idealized two-dimensional fault specified by a unit normal vector $\hat{\mathbf{n}}$, the stress glut, neglecting the effects of prestress and gravity, is

$$\Gamma_{ij} = c_{ijkl}\, n_k\, \Delta u_l \tag{2.2}$$

Where c_{ijkl} is the elasticity tensor and $\Delta\mathbf{u}$ is the slip vector that specifies the relative displacement across the fault surface. $\Delta\mathbf{u}$ is general and can include motion both parallel and perpendicular to the fault plane. We will be primarily concerned with shear dislocations where the slip vector is in the plane of the fault. Substituting equation (2.2) into equation (2.1) yields the expression

$$\mathbf{u}(\mathbf{x},t) = \int_{-\infty}^{\infty} dt' \int dA\; c_{ijkl}\, n_k\, \Delta u_l(\xi,t)\, \mathbf{G}_{i,j}(\mathbf{x},t-t',\xi,0) \tag{2.3}$$

A form of equation (2.3), valid when homogeneous boundary conditions do not apply

[*Burridge and Knopoff*, 1964], is

$$\mathbf{u}(\mathbf{x},t) = \int_{-\infty}^{\infty} dt' \int dA\ c_{ijkl}\, n_k\, \Delta u_l(\xi,t)\, \mathbf{G}_{i,j}(\xi,t-t',\mathbf{x},0) \tag{2.4}$$

where the Green's function in (2.4) now refers to the displacement at position ξ due to a point force at the receiver position $\mathbf{x}$. A more convenient form due to *Spudich* [1980] arises from considering the stress tensor acting at the fault associated with the Green's function in equation (2.4). This results in a form of the representation theorem for the $\hat{\mathbf{a}}$ component of displacement that involves traction $\mathbf{T}^a$ acting across the fault due to a point force in the $\hat{\mathbf{a}}$ direction at the observer

$$u_a(\mathbf{x},t) = \int_{-\infty}^{\infty} dt' \int dA\ \Delta\mathbf{u}(\xi,t) \cdot \mathbf{T}^a(\mathbf{x},t-t';\xi,0) \tag{2.5}$$

The simple form of the representation theorem in equation (2.5) is used in the subsequent development.

Green's Functions

Before we calculate seismograms for a faulting model specified by a slip distribution $s(\xi)$, we must address the question of how the Green's functions are calculated. The response of an elastic wholespace to a point force has terms that decay with distance from the source, r, as r^{-1}, r^{-2}, and r^{-3}. The terms that decay as r^{-1} are referred to as far-field terms and the terms that decay more quickly with distance are referred to as near-field and intermediate-field terms. Following *Aki and Richards* [1980*a*] the spectrum of the displacement in the i^{th}

direction due to a body force $X_o(t)$ in the j^{th} direction in an infinite whole-space is

$$u_i(x,\omega) = \frac{X_o(\omega)e^{i\omega r/\alpha}}{4\pi\rho\alpha^2 r}\left[\gamma_i\gamma_j - \frac{\alpha}{i\omega r}(3\gamma_i\gamma_j - \delta_{ij}) + \left(\frac{\alpha}{i\omega r}\right)^2(3\gamma_i\gamma_j - \delta_{ij})\right]$$

$$\frac{X_o(\omega)e^{i\omega r/\beta}}{4\pi\rho\beta^2 r}\left[(\gamma_i\gamma_j - \delta_{ij}) - \frac{\beta}{i\omega r}(3\gamma_i\gamma_j - \delta_{ij}) + \left(\frac{\beta}{i\omega r}\right)^2(3\gamma_i\gamma_j - \delta_{ij})\right] \quad (2.6)$$

where γ_i are the direction cosines

$$\gamma_i = \frac{(x_i - \xi_i)}{r} \quad (2.7)$$

The dimensionless quantity that determines the relative contribution of the near and far-field terms in (2.6) is $\omega r/\alpha$, the number of wavelengths between the source and receiver. When the inequality

$$\omega r/\alpha >> 1 \quad (2.8)$$

is satisfied, the near-field terms can be neglected to a good approximation. For shear waves the condition is not as stringent since shear wave velocities are lower than compressional wave velocities. *Farra et al.* [1986] have shown that the condition (2.8) is conservative, at least for the case of the 1979 Imperial Valley earthquake where the near-field contribution is negligible at distances comparable to a wavelength.

Note that because of the frequency dependence, equation (2.8) can be satisfied near the source as well as far from it. Thus it is possible to use only far-field contributions to the Green's function, provided the wavelengths are sufficiently short, despite the fact that the receiver is close to the fault. This is different from the usual use of the term "far-field" to describe regions where the only difference in Green's functions from different parts of the

fault is a difference in phase. This has led *Spudich and Frazer* [1984] to use the terms "far-source" to denote regions where the Fraunhofer approximation is valid and "near-source" to denote regions where it is not. This contrasts with the terms "far-field" and "near-field," which in the case of an elastic medium refer to the different terms of the Green's function. Moreover, *Wu and Ben Menahem* [1985] point out that although far-field terms become dominant at large distances, there is no distance range for which the near-field terms are dominant–and thus no true near-field region. We refer to the use of far-field terms only in the Green's function at near-source distances as the high-frequency, near-source approximation.

There are other complications. The Earth is not an infinite whole space and surface wave contributions will become important once the receiver is at a distance of several fault depths from the source; however, the high-frequency, near-source approximation is valid over a frequency band and distance range that render it a useful approximation for a great deal of strong-motion data. The approximation has the advantage that it allows the use of ray theory to calculate Green's functions. This is not only a tremendous computational advantage, but it also yields considerable insight into the factors contributing to ground motion, and allows the effects of laterally-varying structure to be incorporated in our analysis. The development of ray-theory Green's functions for three-dimensionally varying media is treated in Appendix A. An application to an example of a laterally-heterogeneous fault zone is presented in Appendix B.

Kirchhoff-Helmholtz Formulation

The representation theorem, equation (2.4), requires the integration of the scalar product of the traction and the slip vector over the fault plane. In evaluating this integral it is possible to exploit the form of the ray-theory Green's functions to develop an efficient method for calculating theoretical seismograms. The method we use is referred to as isochrone integration [*Spudich and Frazer*, 1984; *Bernard and Madariaga*, 1984] and is a time-

dependent form of the Kirchhoff integral method for the case of an elastic medium [*Burridge*, 1963; *Hilterman*, 1975; *Haddon and Buchen*, 1981].

We begin with the Fourier transform of the representation theorem (2.5)

$$u_a(\mathbf{x},\omega) = \int dA\ \Delta\mathbf{u}(\xi,\omega) \cdot \mathbf{T}_a(\mathbf{x},\omega;\xi,0) \tag{2.9}$$

Using equations (A.19-A.22) we can express the high frequency approximation to the tractions, $\boldsymbol{T}$, as

$$\mathbf{T}_a^{\upsilon} = i\omega\, \mathbf{H}_a^{\upsilon}\, e^{i\omega t_{\upsilon}} \tag{2.10}$$

where the superscript υ refers to α or β for compressional and shear waves tractions respectively. If we express the slip distribution as the product of a time dependent function $f(t\text{-}t_r)$ and a spatially dependent slip amplitude vector, $\mathbf{s}(\xi)$

$$\Delta\mathbf{u}(\xi,t) = \mathbf{s}(\xi, t) f(t - t_r(\xi)) \tag{2.11}$$

then we can use the Fourier spectrum of (2.11) in (2.9) to obtain

$$u_a(\mathbf{x},\omega) = i\omega f(\omega) \int dA\ \mathbf{s}(\xi) \cdot \mathbf{H}_a^{\upsilon}\, e^{i\omega(t_r + t_{\upsilon})} \tag{2.12}$$

taking the inverse Fourier transform of (2.12) yields

$$u_a(\mathbf{x},t) = \dot{f}(t) * \int dA\ \mathbf{s}(\xi) \cdot \mathbf{H}_a^{\upsilon}\, \delta(t - t_r - t_{\upsilon}) \tag{2.13}$$

The delta function in the integrand means that the only contributions to the integral come from regions of the fault of equal arrival time at the observer position, **x**, where $t = t_r + t_v$. These regions are called isochrones [*Spudich and Frazer*, 1984; *Bernard and Madariaga*, 1984] and are lines of constant phase on the fault as observed at the receiver. The quantity $t_a = t_r + t_v$ is referred to as the isochrone time and is a function of the wave type, the receiver location and the rupture model. Our fom of the representation theorem (2.13) can be further simplified by the change of variables

$$dA = c\ dl\ dt_a \tag{2.14}$$

where c is the isochrone velocity, which is defined as

$$c = \left|\nabla_s(t_a)\right|^{-1} \tag{2.15}$$

In (2.15) the surface gradient on the fault plane with unit normal $\hat{\mathbf{n}}$ is

$$\nabla_s = (\mathbf{I} - \hat{\mathbf{n}}\hat{\mathbf{n}}) \cdot \nabla \tag{2.16}$$

The change of variables (2.14) allows us to rewrite equation (2.13) as a line integral rather than a surface integral.

$$u_a(\mathbf{x},t) = \dot{f}(t) * \int dl\ c\ \mathbf{s}(\xi) \cdot \mathbf{H}_a^v \tag{2.17}$$

Equation (2.17) is the form of the representation theorem that we use for calculating theoretical seismograms.

Parameterization of the Slip Distribution

The determination of the distribution in space and time of slip on an earthquake fault is one of our principal objectives. In the previous section we specified the slip model as a product of a temporally-varying function and a spatially-varying function. We are concerned with the functional form of the slip rate because the displacement depends on the time derivative of the slip function in (2.17). Several simple functions have been used in previous studies.

Haskell [1964] represented the slip velocity using a boxcar function defined as

$$\dot{f}(t) = H(t - t_r) - H(t_h - t) \tag{2.18}$$

where the function is a constant non-zero value only between the rupture time t_r and the healing time t_h. *Aki* [1968] modeled the 1966 Parkfield, California earthquake with a propagating dislocation across the fault that occurred instantaneously so that the slip velocity function was singular

$$\dot{f}(t) = \delta(t-t_r) \tag{2.19}$$

Hartzell and Helmberger [1982] used a triangular function for the slip velocity in their study of the 1979 Imperial Valley, California earthquake.

More recently an inverse square-root singularity has been used to parameterize the slip velocity function [*Boatwright*, 1980; *Archuleta and Hartzell*, 1981; *Campillo and Bouchon*, 1983]. The general form is

$$\dot{f}(t) = (t - t_r)^{-1/2}[H(t - t_r) - H(t_h - t)] \tag{2.20}$$

where t_h and t_r (Figure 2.1) both vary as a function of position on the fault. This is the parameterization we have chosen to use.

Such a parameterization is attractive because it has the general form of the slip velocity found for a number of analytical and numerical dynamic rupture models of the earthquake source [e.g., *Kostrov*, 1966; *Rice*, 1968; *Freund*, 1979; *Day*, 1982*a,b*]. It is also no more complicated than (2.18), both being specified by the same number of parameters. The slip time function in (2.20) has the units of $t^{-1/2}$, which implies that the spatially-varying slip amplitude, $s(\xi)$, is in fact a slip velocity intensity with units of $l/t^{-1/2}$. Thus when determining the total slip from the slip intensity distribution it is necessary to multiply by the square root of the rise time $(t_h - t_r)^{1/2}$.

At a particular location on the fault, slip begins at the rupture time t_r and ends at the healing time t_h. The time of rupture is interpreted as the time at which the dislocation front passes. The healing time is usually attributed to a healing front, like the rupture front, that propagates inward from the unruptured edges of the faulted area [*Madariaga*, 1976; *Day*, 1982*a*]. Our observations of rupture are consistent with some previous studies [*Bouchon*, 1978; *Archuleta*, 1984] that suggest that this is a poor assumption.

In calculating the slip velocity function in (2.20) we have a singularity in the slip velocity at the instant of rupture. We approximate the behavior of the function in the neighborhood of the singularity by adding a small imaginary part, $i\Delta t$, to the argument of the square root, where Δt is the sampling interval. This procedure removes the singularity from the real axis at the expense of a slight acausality in the function [*Madariaga and Papadimitriou*, 1985]. This is a justifiable procedure because our data are band-limited and the approximation effectively low-pass filters the function. Moreover, (2.20) is an idealization for a medium of infinite strength. The square-root singularity in the slip amplitude behind the rupture front is associated with a square-root singularity in stress ahead of the rupture front. For a material of finite strength the stress and slip velocity singularities will be smoothed by an end-zone

where the finite-valued cohesive strength of the material is exceeded [*Barenblatt*, 1959; *Ida*, 1972].

Our expression for the slip velocity is

$$\Delta\dot{\mathbf{u}} = \mathbf{s}(\xi)(t - t_r)^{-1/2}[H(t - t_r) - H(t_h - t)] \tag{2.21}$$

Thus, once we have specified the fault plane, it remains to determine the parameters $\mathbf{s}$, t_r, and t_h. We simplify the problem further by assuming that the rise time is constant. This will be discussed in greater depth in subsequent chapters, where data from individual earthquakes are analyzed, but it is motivated by observations that the duration of slip at a point on a fault, when independently resolvable from the duration of motion due to the extent of the fault, is quite small [*Aki*, 1968; *Bouchon*, 1978].

In this approximation

$$\Delta\dot{\mathbf{u}}(\xi,t) = \mathbf{s}(\xi)(t - t_r(\xi))^{-1/2}B(t_d) \tag{2.22}$$

where $B(t_d)$ is a boxcar function which is unity for the duration of the rise time, t_d, and zero otherwise. Modeling the rupture history of an earthquake parameterized as in (2.22) reduces to determining the time at which rupture begins $t_r(\xi)$ and the strength at which it occurs $\mathbf{s}(\xi)$, both as a function of position on the fault.

We are now in a position to discuss the effect of the parameterization on the inverse problem. To do this we first rewrite equation (2.17) with the unknown parameters appearing explicitly

$$u_a(\mathbf{x},t) = \dot{f}(t) * \int_{l(t_r + t_v)} dl \left|\nabla_s(t_r + t_v)\right|^{-1} \mathbf{s}(\xi) \cdot \mathbf{H}_a^v \tag{2.23}$$

In equation (2.23) the slip intensity factor appears in the integrand indicating that except for a convolution there is a straightforward linear relationship between the ground motion u observed at $\mathbf{x}$ and the slip intensity, $\mathbf{s}$, at ξ; however, the rupture time enters into (2.23) nonlinearly. The rupture time, t_r, appears both in the isochrone velocity term in the integrand and in the determination of the path of the line integrals or isochrones l. Thus to infer the rupture model from the data we will have to invert a nonlinear system of equations.

Although nonlinear problems are difficult to solve, there are marked advantages to posing the problem this way. Instead of dividing the total area of the fault into areas that rupture in a pre-described fashion, we are able to specify the rupture time on a grid of points without invoking individual subfaults. This formulation properly includes directivity effects because the rupture propagation is a derived property rather than an assumed one. The parameterization that we use also reduces the number of unknowns to a manageable number. Previous studies have allowed subfaults to rupture a number of times, which increases the number of unknowns and increases the degree of non-uniqueness of the problem. Moreover, the interpretation of the behavior of the rupture front is facilitated when rupture occurs only once at each point on the fault. Finally, by specifying a functional form that is consistent with models of the earthquake source based on fracture mechanics, it is possible to estimate the shear fracture energy–a fundamental parameter in the description of earthquakes as propagating shear cracks.

Figure Captions

Figure 2.1 The inverse square root singularity slip velocity time function we have adopted for this study is shown. The quantities t_r and t_h, referred to as the rupture time and the healing time respectively, denote the time that rupture initiates and terminates as a function of position on the fault. The duration of faulting or rise time is defined as $t_d = t_h - t_r$. The functional form is the same as that found for dynamical models of brittle fracture and for numerical simulation of earthquake faulting. We assume that the time dependence is constant over the fault and that only the amplitude varies.

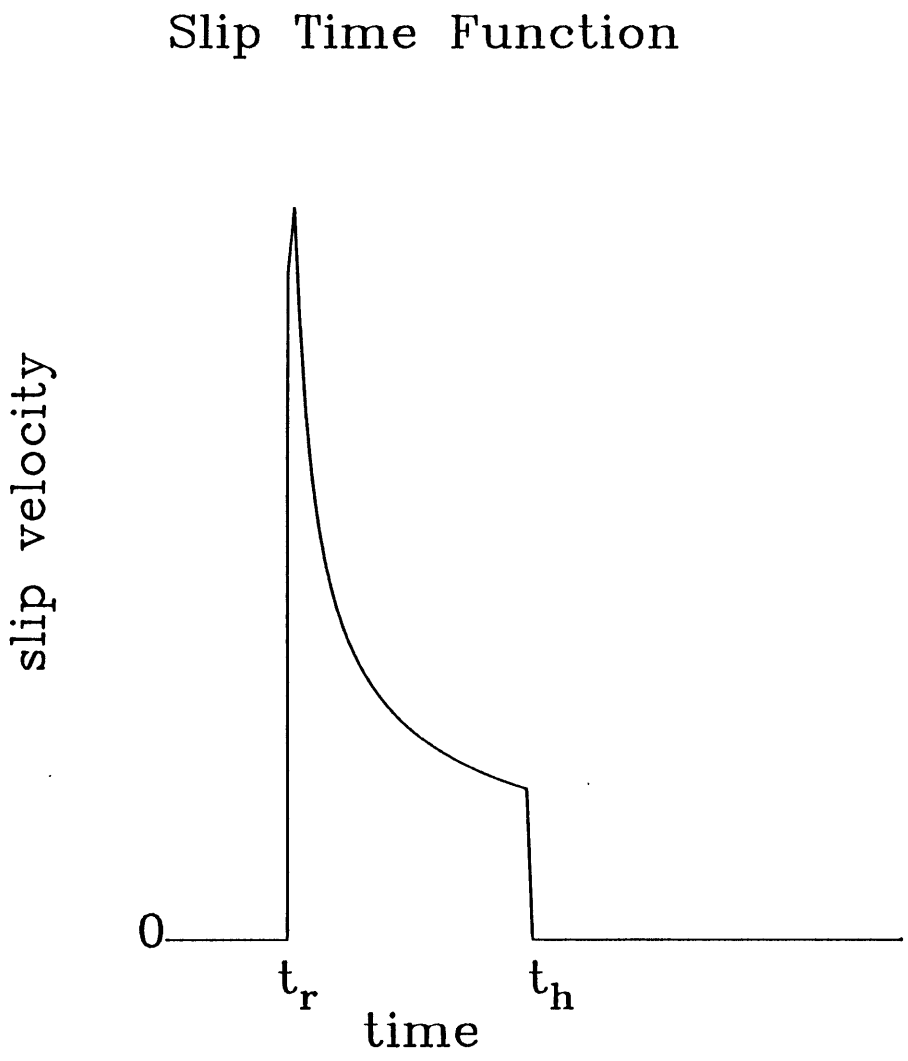

Figure 2.1

CHAPTER 3

THE INVERSE PROBLEM FOR FAULT RUPTURE BEHAVIOR

In this section we formulate and solve the inverse problem for inferring the rupture history of an earthquake from near-source records of the ground motion. The problem as we pose it is a nonlinear one, which we solve using a linearization of the system with respect to rupture time. Because the problem is underdetermined, a regularization condition is added. The utility and implementation of *a priori* constraints on the model such as the direction and extent of slip are discussed. Finally, sensitivity tests, which are used to assess the reliability of the results are described. The presentation of the results for the sensitivity tests are presented in Chapters 4-6 in the context of specific earthquakes.

Linearized Inversion

The model parameters to be estimated are slip intensity **s** and rupture time t_r as a function of position, ξ, on the fault. Because the data are nonlinearly related to rupture time we have chosen to perform a linearized inversion to recover the model parameters. The system of equations to be solved can be written as

$$\mathbf{g(m)} = \mathbf{d} \tag{3.1}$$

The data vector **d** comprises seismograms, the model vector **m** comprises the values of rupture time t_r and components of the slip intensity **s** at a set of points on the fault. The operator **g** represents the method that we use to calculate theoretical seismograms from the model, equation (2.17). Partial derivatives of the theoretical seismograms with respect to the model parameters are calculated using equation (2.17). Partials with respect to slip amplitude are calculated explicitly. The partial derivatives with respect to rupture time, which are simply

time derivatives of the seismograms for a single gridpoint of the current model, are calculated using a central difference method accurate to $O(\Delta t^2)$.

Defining the matrix of partial derivatives **A** by the relation

$$A_{ij} = \frac{\partial g_i}{\partial m_j} \tag{3.2}$$

equation (3.1) can be linearized about the current model **m** as

$$\mathbf{g(m + \delta m)} = \mathbf{g(m)} + \mathbf{A\delta m} \tag{3.3}$$

where $\mathbf{\delta m}$ represents a perturbation to the model parameters. If $\mathbf{g(m + \delta m)}$ satisfies the data, then equation (3.3) can be written as

$$\mathbf{A\delta m} = \mathbf{d} - \mathbf{g(m)} \tag{3.4}$$

The perturbations to the model parameters can then in principle be estimated from (3.4) using a suitable inverse such as the least-squares, minimum-norm generalized inverse of **A** [*Lanczos*, 1961]:

$$\mathbf{\delta m} = \mathbf{A}^{\dagger}[\mathbf{d} - \mathbf{g(m)}] \tag{3.5}$$

Assuming for the moment that it is possible to calculate $\mathbf{A}^{\dagger}$ in a straightforward manner, the problem consists of iteratively perturbing and updating a starting model until some convergence criterion is met. Of course the improvement to the solution depends on how well the linearization of the theoretical seismograms with respect to the model parameters represents the change in the seismograms when the model is perturbed.

In this approach the nonlinear inverse problem is solved by incremental perturbations, calculated from a linearized approximation, to an assumed starting model. Because the problem is nonlinear, there is no guarantee that the procedure will converge to a global minimum-norm solution. To test for convergence to a local rather than a global minimum it is helpful to perform the inversion for a wide range of starting models. Even then convergence to a global minimum is not assured.

The procedure that we use to solve the linearized inverse problem has a nested set of iterations. In the outermost iteration the model is updated by adding the calculated perturbation to the previous model:

$$\mathbf{m}_n = \mathbf{m}_{n-1} + \delta\mathbf{m}_n \tag{3.6}$$

A new partial derivative matrix and residual vector $\mathbf{d} - \mathbf{g}(\mathbf{m}_n)$ are calculated after each iteration using equation (2.17). Iterating on the model is necessary because the relation between model and data is nonlinear. In the inside iteration the perturbation $\delta\mathbf{m}_n$ to the current model $\mathbf{m}_{n-1}$ is calculated with an iterative back-projection technique. The iterative back-projection is made necessary by the large size of A.

Iterative Back-Projection

The tomographic back-projection that we use is a simultaneous, iterative, reconstruction technique (SIRT) that approximates the effect of a generalized inverse with a damping of components associated with small singular values [*Ivanson*, 1983; *Olson*, 1987]. It is especially useful for large systems of equations where conventional matrix inversion is impractical. Using the SIRT technique the K^{th} estimate of the perturbation to the current model is generated by the iterative sequence

$$\delta \mathbf{m} = \sum_{k=1}^{K} \frac{1}{\sigma_k} \mathbf{A}_{n-1}^{\mathrm{T}} \left[\mathbf{d} - \mathbf{g}(\mathbf{m}_{n-1}) - \mathbf{A}_{n-1} \delta \mathbf{m}_n^{k-1} \right] \qquad (3.7)$$

$\mathbf{A}^T_{n-1}$ denotes the transpose of the partial derivative matrix, and $1/\sigma_k$ is the weighting applied to the k^{th} back projection. In equation (3.7) $\delta \mathbf{m}_n^0$ is the null vector, and the perturbation to the model parameters $\delta \mathbf{m}_n$ is calculated by a sequence of K weighted back-projections of the data residual vector, $\mathbf{d} - \mathbf{g}(\mathbf{m}_{n-1})$, onto the rows of $\mathbf{A}^T_{n-1}$. Note that this iterative procedure uses only the transpose of the **A** matrix and only matrix-by-vector operations are required. No matrix-by-matrix multiplications or matrix inversions are performed. In the standard least-squares algorithms it is necessary to form the normal matrix $\mathbf{A}^T_{n-1}\mathbf{A}_{n-1}$, which can be quite large for this problem, and to calculate its inverse. The least-squares solution for the model perturbation is

$$\delta \mathbf{m} = \left[\mathbf{A}^T_{n-1} \mathbf{A}_{n-1} \right]^{-1} \mathbf{A}^T_{n-1} \left[\mathbf{d} - \mathbf{g}(\mathbf{m}_{n-1}) \right] \qquad (3.8)$$

The solution obtained by the SIRT technique approximates the effect of the inverse of the normal matrix, $[\mathbf{A}^T_{n-1}\mathbf{A}_{n-1}]^{-1}$ on the back-projected data residuals $\mathbf{A}^T_{n-1}(\mathbf{d} - \mathbf{m}_{n-1})$.

The choice of the weighting $1/\sigma_k$ is crucial in determining the properties and convergence rate of the solution. We use a Chebyshev weighting scheme developed by *Olson* [1987]. This algorithm has the virtue of calculating the eigencomponents of the solution to a uniform precision over a prescribed range of eigenvalues with much more rapid convergence than other algorithms such as the Dines-Lytle algorithm [*Dines and Lytle*, 1979]. For a specified bandwidth and accuracy the Chebyshev technique features a square root reduction in the number of iterations required to attain a given accuracy over other methods [*Olson*, 1987]. The technique differs from other tomographic techniques in that σ_k changes with each iteration. The values of σ_k depend on the range of eigenvalues over which convergence is to

be enforced and the desired accuracy. Once these quantities are specified, the number of required iterations is known [*Olson*, 1987].

Many different eigenvalue ratios and numbers of iterations were tested for synthetic data sets and for the earthquake data. We found that the eigenvalue ratio of 25 and K = 16-32 iterations, which corresponds to about 2.5 digits of accuracy across the bandwidth, fit the data well, and converge quickly without introducing a very irregular rupture model.

The relatively narrow bandwidth and small number of iterations are chosen due to the nonlinearity of the problem. Because the problem is nonlinear, the partial derivatives in the **A** matrix vary as the model parameters in $\boldsymbol{m}$ vary with iteration, and excessive accuracy in determining finite perturbations to the model is not warranted. The SIRT method described above was developed for linear problems, but we find that it works well for the linearized problem in the present application.

Weighting

Because rupture time and slip amplitude represent quantities with different physical dimensions, we weighted the partial derivative matrix **A** and the perturbation to the model vector $\delta\mathbf{m}$ in equation (3.5) with a diagonal scaling matrix appropriate for the units of rupture time expressed in s and slip intensity expressed in $m/s^{1/2}$. For the case of the Morgan Hill earthquake with an assumed rupture velocity of 0.8 times the local shear wave velocity, we found that a relative weighting of 1 for slip amplitude derivatives to 0.003 for rupture time derivatives yields perturbations to the model parameters that fit the data well and allow both rupture time and slip amplitude to vary substantially.

Equation (3.5) is also normalized by a diagonal data covariance matrix. The elements of the data covariance matrix are chosen to be equal to the power per unit time for each seismogram multiplied by a scalar coefficient. The normalization by the power is performed so that seismograms with large amplitudes will not dominate the model, and the scalar

coefficient is used to give greater weight to data for which the Green's functions are thought to be more accurate.

Regularization

In practice, we find it necessary to introduce an inequality constraint to ensure that the resulting model agrees with the expected sense of relative motion on the fault. This is necessary for several reasons. Strong trade-offs can occur between changes in rupture time and changes in slip intensity [*Madariaga*, 1983; *Spudich and Frazer*, 1984] and effects that are caused by rupture time variations could be mapped into infeasible slip variations. Additionally, the data are band-limited in frequency so that the low-wavenumber components of the source will be difficult to recover. Finally, our Green's functions are only approximate, and the data incomplete so that the exclusion of infeasible solutions helps to reduce the degree of non-uniqueness in the problem.

We enforce the inequality constraint on the sign of the slip intensity using a penalty function that increases parabolically as the solution violates the inequality constraint [*Luenberger*, 1984]. For the earthquakes we have studied, the constraint causes the slip intensity to be consistent with right-lateral strike-slip motion across the fault. It is implemented by adding a row to the **A** matrix and an element to the **d** vector for each model parameter that violates the constraint. The new row of the **A** matrix is zero except for a single element which multiplies the infeasible parameter. The added element of the **d** vector is zero, damping components of the solution that include the infeasible model parameter. Thus the inequality constraint is satisfied approximately with some of the parameters slightly violating the constraint.

For the penalty function approach to work effectively it is desirable to limit the strength of the perturbation to the constrained variable. This is a consequence of the constraint not becoming active until a model parameter is within the infeasible region. If a model parameter grossly violates the constraint on one iteration, the subsequent damping makes it difficult to

change its value substantially. Ideally the infeasible parameter will approach the feasible region from the infeasible side of the constraint. In practice due to a limited number of computational effort the inequality constraints are slightly violated.

To limit the strength of the perturbation we have invoked a smoothness constraint on the model perturbation. Smoothness constraints on slip amplitude have been used previously in this application by *Hartzell and Heaton* [1986] and have been used by *Shaw and Orcutt* [1985] and *Constable et al.* [1987] as a practical constraint in the solution of nonlinear systems. We impose smoothness constraints on both the perturbations to the slip amplitude and the perturbations to rupture time. The constraints are implemented by adding a weighted first-differencing operator to the partial derivative matrix and additional zeroes to the data vector. The differencing operator equates the difference in two adjacent model parameters to zero, which has the effect of damping components of the solution which are spatially rapidly-varying. Representing the penalty operator as $\mathbf{P}_{n-1}$, which in general changes with each iteration as the constraint becomes active on different parameters, and the smoothing operator as $\mathbf{D}$, the system of equations that we solve using the SIRT technique (3.7) is

$$\begin{pmatrix} \mathbf{A}_{n-1} \\ \gamma \mathbf{P}_{n-1} \\ \varepsilon \mathbf{D} \end{pmatrix} \delta \mathbf{m}_n = \begin{pmatrix} \mathbf{d} - \mathbf{g}(\mathbf{m}_{n-1}) \\ 0 \\ 0 \end{pmatrix} \tag{3.9}$$

In equation (3.9) the scalars γ and ε are the weights of the inequality and smoothness constraints. The larger the values of γ or ε are, the greater the importance assigned to satisfying the constraints at the expense of fitting the data. We have found it advantageous to begin with large values of γ and ε, decreasing them somewhat as a solution is approached, similar to the Levenberg-Marquardt method [*Levenberg*, 1949].

The model and data dimensions of the problem are quite large. As an example for the study of the Morgan Hill earthquake presented in chapter 4, the assumed fault plane covers an area of 300 km^2. The grid spacing is 1 km in the along-strike and downdip directions.

When we invert for both strike-slip amplitude and rupture time, the model dimension is 748. The number of points in data space before smoothing is 1749. For the Imperial Valley earthquake the fault plane covers an area of nearly 600 km^2 and the model dimension approaches 1500.

In the present problem, since the ray theory Green's functions are non-negligible for only a short time for each source-receiver combination, the **A** matrix is composed largely of zeroes or values of negligible amplitude. The small percentage of nonzero elements in **A** allows the application of sparse matrix techniques. We use a scheme where the nonzero elements of the **A** matrix and the associated column and row indices of the matrix are stored in randomly packed vectors. For the case of the Morgan Hill earthquake treated in the next section, the **A** matrix is composed of only 15% nonzero elements and the decrease in computational overhead is substantial.

The efficiency of the method is important for several reasons. One reason is that due to the nonlinear nature of the problem the **A** matrix must be inverted several times. The efficiency is also important because we can include higher-frequency data and a denser grid in the analysis, allowing the possibility of finer resolution of the rupture behavior.

Perhaps the most difficult part of the inverse problem, particularly in a large nonlinear system such as the one treated here, is an assessment of the reliability the results. To carry out a meaningful interpretation of the results it is necessary to determine some estimate of the errors associated with the estimation of the model parameters as well as possible correlations between different model parameters. To do this we resort to sensitivity tests in which we calculate synthetic data from a known model, add appropriate amounts of realistic noise, and perform the inversion with the same amount of data and the same station geometry as is available for each earthquake. Sensitivity tests have proven quite useful in the interpretation of results from other large tomographic systems [*Spakman and Nolet*, 1988]. The results from the sensitivity tests allow us to make statements about the limits of spatial resolution,

the amount of non-uniqueness, and the trade-off between variations in slip and rupture time in the modeling procedure.

We use sensitivity tests that consist of calculating theoretical seismograms for a known faulting model. As these are are calculated we add a smoothed perturbation to the rupture time for each station. This has the effect of changing the phase of signals from different parts of the fault and allows us to simulate the effect of lateral heterogeneity. The amplitudes will also be affected since the rupture time strongly affects the amplitude (2.17). We have also added Gaussian random noise, but find that this does not provide a realistic test of the method.

The sensitivity tests depend on the data available for each earthquake and the fault and station geometry. For this reason we present them in the context of the interpretation of derived rupture models in Chapters 4-6.

CHAPTER 4

THE 1984 MORGAN HILL EARTHQUAKE

In this chapter we apply the techniques developed in the previous two chapters to determine the rupture history of the 1984 Morgan Hill earthquake from near-source records of the ground motion. We discuss the available data, the approximations and constraints used in the inversion, sensitivity tests used to explore the model resolution, the comparison of our results with other studies of the same earthquake, and the interpretation of our derived rupture models.

Background

The Morgan Hill earthquake (M_L = 6.2) began at 2115:18.9 UTC on April 24, 1984, at (37.317°N, 121.682°W, d = 9 km) [*Cockerham and Eaton*, 1987] near the junction of the Calaveras and Hayward faults east of San Jose, California. The aftershocks were located along the Calaveras fault from approximately 5 km to the northwest to 25 km southeast of the hypocenter [*Bakun et al.*, 1984]. The location of the aftershocks with respect to the hypocenter suggests that rupture propagation was primarily unilateral to the southeast (Figure 4.1). The aftershock distribution suggests that the fault dips approximately 85° to the northeast [*Cockerham and Eaton*, 1987], and that the fault at depth is displaced to the east of the surface trace. The aftershock zone is immediately to the northwest of the aftershock zone of the August 5, 1979, Coyote Lake earthquake (M_L = 5.9).

Damage caused by the earthquake was concentrated at the southeast end of the aftershock zone near the town of Morgan Hill. The accelerograph at the Coyote Lake Dam Abutment (CLD), also at the southeast end of the aftershock zone, recorded an acceleration of 1.29 g on the horizontal component N285°E. Ground cracking was observed near the CLD station

after the event (R. Sherburne, personal communication, 1984), suggesting that there may have been nonlinear site behavior during the earthquake. Some surface cracks were observed in the fault zone near Anderson Reservoir after the earthquake; however, they are thought to represent secondary failure as a result of strong shaking rather than slip on the fault during the earthquake [*Bakun et al.*, 1984]. No recognizable short-term precursors were noted for this event [*Bakun et al.*, 1984], although it did fill a region deficient in microearthquake activity [*Bakun*, 1980].

The extent of the rupture zone considered in our analysis is based on the distribution of aftershocks (Figure 4.1). It extends from 5 km to the northwest to 25 km to the southeast of the hypocenter. The location of the fault is assumed to follow the surface trace with a dip of 85° to the northeast. This is contrary to the aftershock locations of *Cockerham and Eaton* [1987], which are displaced up to 1.5 km to the east of the surface trace. *Cockerham and Eaton* [1987] argue that the displacement of the hypocenters to the east of the fault is not an artifact because the location of a refraction shot to within 0.5 km of its true origin suggests that the discrepancy is real. We have attempted to fit the strong motion data for both possible fault positions. The results indicate that a fault defined by the surface trace fits the data slightly better than a fault defined by the aftershock zone. However, the effect on the fit to the data is not large enough to distinguish between the two possible fault plane locations.

Another interesting aspect of the aftershock data is that the principal fault plane defined by the aftershocks is simpler than would be expected from the surface trace (Figure 4.1). The surface trace near the hypocenter is poorly defined, but farther south in San Felipe Valley it bends to a more southerly orientation. Several kilometers to the north of Anderson Reservoir the surface trace returns to an orientation of about N30°W before undergoing a complex eastward-stepping series of offsets near Anderson Reservoir. In contrast, the aftershock zone can be well represented by two planes, one with an orientation of N35°W over the northwest end of the aftershock zone and the other with an orientation of N29°W over the southeast end of the aftershock zone [*Cockerham and Eaton*, 1987]. The bend in the

aftershock zone is opposite in sense to the offset in the surface trace. Aftershocks that occurred off the main trace of the Calaveras fault, particularly those at the southern end of Anderson Lake, are thought to be on subsidiary faults that have been mapped in the region [*Cockerham and Eaton*, 1987].

Data

The earthquake was well recorded by film-recording, analog, strong-motion instruments, most of which had WWVB time code [*Shakal et al.*, 1984; *Brady et al.*, 1984]. We obtained the acceleration data after they had been corrected for instrument response and resampled at a uniform time interval. We performed our own filtering and integration to velocity and displacement in order to have a data set that was uniformly filtered and as broadband as possible. We band-pass filtered all the data with a two-pole Butterworth filter with low- and high-cut corner frequencies at 0.2 and 4.0 Hz. The filter is run both forward and backward in time so that the resulting filter is effectively a four-pole filter with zero phase. The horizontal components were rotated into a coordinate system with the x axis parallel to the strike of the fault (150°), the z axis pointing downward, and the y axis forming a right-handed system (240°). In this system we represent right-lateral strike-slip as a negative quantity.

Strong motion accelerometers located near the rupture and the transverse (240°) component of acceleration are shown in Figure 4.2. The accelerograms are arranged such that the ordinate offset corresponds to the observed trigger time, except for the IBM station which did not record absolute time. The IBM record is offset so that the S wave pulse from the hypocenter has the expected arrival time. The Coyote Lake Dam station (CLD), which recorded the large acceleration, has a complex record with several strong pulses. Other stations show a complexity inconsistent with smooth rupture propagation. The Hall's Valley station (HVR) in particular exhibits a large late pulse which occurs approximately 8 s after the hypocentral S wave arrival.

In the 240° (y component) displacement records (Figure 4.3) the second pulse is more readily apparent at the other stations. From the timing of the pulse it is apparent that it originates near the Anderson Dam station (ADD) [*Bakun et al.*, 1984; *Uhrhammer and Darragh*, 1984; *Abrahamson and Darragh*, 1985; *Hartzell and Heaton*, 1986]. It is worth noting that the duration of the second pulse at HVR is only about a second. For rupture propagating unilaterally away from HVR the short duration of the pulse implies that the source of the second zone is extremely compact. Such a model is inconsistent with the rest of the data.

The data contain several features that are inconsistent with our assumptions of a simple fault geometry and a laterally-homogeneous velocity structure. For the fault geometry assumed, the 150° or x component of displacement (Figure 4.4) should be nearly nodal for S waves at stations HVR, CLD, and G06. However, these records show large-amplitude arrivals at the same time that large S waves can be seen on the y component of motion (Figure 4.3). A likely cause is lateral heterogeneity. Several authors [*Mayer-Rosa*, 1973; *Mooney and Luetgert*, 1982; *Cormier and Spudich*, 1984; *Blümling et al.*, 1985; *Mooney and Colburn*, 1985] have documented the existence of a zone of low velocity associated with the fault zone in this region. Such a zone may act as a waveguide and refract waves horizontally into the fault zone [*Cormier and Spudich*, 1984; *Cormier and Beroza*, 1987]. Focusing of waves by the zone of low velocity may account for the observed large amplitudes of S waves on the x component at stations in the fault zone. A simple application of dynamic ray tracing to the calculation of seismograms for a shallow source in a low-velocity fault zone is given in Appendix B.

An example of the effects of lateral heterogeneity associated with the fault zone can be seen in records from the Gilroy array. The Gilroy array runs transverse to the Calaveras fault approximately 13 km to the southeast of the end of the aftershock zone (Figure 4.3). The southern extension of the assumed fault plane for the Morgan Hill earthquake bisects the Gilroy array between stations G04 and G06. The y component of displacement for the

Gilroy array data is very different for G06 and G07 (Figure 4.5). G06 has several pulses of approximately one second duration, whereas G07 is almost entirely deficient in high-frequencies. A possible interpretation is that G07 is in a shadow zone for direct *S* wave arrivals from the Morgan Hill earthquake.

The data used to infer the rupture model consist of the *x* and *y* components for stations HVR, IBM, ADD, CLD, and G06, as well as the vertical component of the BKS ultra-long-period seismograph, which was on scale for the earthquake [*Uhrhammer and Darragh*, 1984]. The G07 record was not included in the analysis because it exhibited strong effects, apparently due to lateral heterogeneity, that could not be modeled. Other stations such as those in the Gilroy array other than G06 and station SJH at the San Jose 101/280/680 freeway interchange, are not used because they are located on sediments in the Santa Clara Valley where the velocity structure is different from the source region [*Blümling et al.*, 1985; *Mooney and Colburn*, 1985]. Seismograms recorded at these stations were of much longer duration than those used in the inversion [*Hartzell and Heaton*, 1986], and the arrival times of *P* and *S* waves can only be accounted for by invoking a laterally-varying velocity model.

The vertical components were not used for the local stations because the Green's functions did not predict vertical motion very well. Even with complete seismograms, the fit to the vertical data obtained by *Hartzell and Heaton* [1986] was not nearly as good as for the horizontal data. Because the *x* component of the data for the available stations was primarily *P-SV* whereas the y component was primarily *SH*, the *y* component is given a greater weight in the inversion than the *x* component. This compensates for our inability to predict the amplitude of the *x* component accurately assuming a laterally-homogeneous structure.

We use a high frequency approximation in (2.17) to calculate seismograms, and we are now in a position to determine how good the approximation is for a real data set. There are several studies of seismic velocity structure in the vicinity of the Morgan Hill earthquake. The study that most closely overlaps the source region of the Morgan Hill event is that of *Blümling et al.* [1985]. We have adopted a smoothed version of this model (Figure 4.6).

Our model also closely resembles that of *Ellsworth and Marks* [1980] derived for the Calaveras fault farther to the north. We approximate the structure using layers of constant velocity gradient having no discontinuities in velocity at layer boundaries. We also omit the low-velocity zone found by both *Blümling et al.* [1985] and *Ellsworth and Marks* [1980].

For the comparison of asymptotic and complete seismograms we use two simple sources of small extent. Both sources are vertical, right-lateral, strike-slip faults with constant slip, a moment release of 10^{15} Nm, and a rupture velocity of 0.8 times the local shear wave velocity. The faults are circular with a diameter of 1 km. The slip rate has a box-car time dependence $\dot{f}(t) = [H(t - t_r) - H(t_h - t)]$ where t_h is the time at which slip ceases and $t_h - t_r$ is the rise time. The rise time is assumed to decrease linearly with radius from a maximum value of 0.375 s at the center to 0 s at the edges of the fault. The shallow fault extends from 4 to 5 km, and the deeper fault extends from 8 to 9 km depth. The depth of the fault centered at 4.5 km is shallower than most of the slip during the Morgan Hill earthquake as determined by *Hartzell and Heaton* [1986], and shallower than most of the aftershocks located by *Cockerham and Eaton* [1987]. The depth in this example is chosen to illustrate the effect of converted *SV* to *P* diffracted waves at the free surface in the presence of a steep velocity gradient. This effect is poorly modeled by the ray theory method. The deeper fault corresponds to the depth at which most of the slip during the earthquake occurred. The shallow fault should show the greatest difference between the two methods since free surface effects will be stronger and the fault will be closer to the receiver resulting in a larger contribution from near-field waves. The results for the deep source are more representative of the error in the high-frequency, near-source approximation for most of the fault.

We calculate seismograms using equation (2.17) for direct *P* and *S* waves and compare them with seismograms calculated using the discrete-wavenumber / finite-element method [*Spudich*, 1981; *Olson et al.*, 1983] for receivers at 2, 6, 10, 15, and 20 km from the fault. In the "*SH*" case the receivers are directly along the strike of the fault, and in the "*P-SV*" case the receivers are 45 degrees off the strike of the fault. The terminology "*P-SV*" and "*SH*"

refers to the body wave contributions in the far-field for the two geometries. The seismograms are band-pass filtered the band-pass filter at 0.2 and 4.0 Hz described above.

The comparison of the high-frequency, near-source seismograms with complete seismograms for the velocity structure adopted in this study is generally favorable, even in the shallow fault case (Figure 4.7). The near-field terms show up most clearly as precursors to the *S* waves on the *SH* component for the receivers at 2 and 6 km distance and are characterized by small amplitudes and low frequencies. The other point at which the ray-theory Green's functions are inadequate is for rays that depart the fault as *SV* waves and convert to *P* waves at the free surface. For S waves that depart the fault nearly horizontally (a source receiver distance of 10 to 15 km for the shallow fault) the horizontal slowness is nearly equal to that of a horizontal converted *P* wave at the free surface. This results in *SV* to *P* diffracted waves at the free surface which are not accounted for by simple ray theory. For *SV* waves that leave the fault at a steeper angle, a *P* wave refraction in the shallow sediments arrives shortly after the direct *S* wave. These two cases in which the approximation fails should not significantly affect our results for the Morgan Hill earthquake. Near-field contributions will be small since the rupture did not extend to the free surface [*Bakun et al.*, 1984].

The comparison for the deep source (Figure 4.8), which is more representative of the radiation from most of the fault [*Hartzell and Heaton*, 1986], is more favorable. Near-field contributions are only appreciable for the closest receiver. The *SV* to *P* diffracted wave is not present since the slowness at the source is smaller than that of a horizontally travelling *P* wave at the free surface. The fault-receiver geometry for the Morgan Hill earthquake is such that stations do not record much *SV* radiation from most of the fault. Those stations or components of motion that are dominated by *P-SV* are assigned a lower weight when the inversion is performed to reflect the greater uncertainty associated with the determination of their Green's functions.

We have also compared our ray-theory Green's functions with complete Green's functions obtained by *Hartzell and Heaton* [1986] for subfaults in a similar velocity structure that includes the zone of low velocity. The omission of the low-velocity zone has no noticeable effect on the seismograms since rays bottom at depths shallower than the top of the low-velocity zone for the source-receiver distances considered. For the station BKS the rays propagate through the low-velocity zone and the amplitudes of the seismograms may be affected; however, the predicted travel-time for the direct *P* wave is very close to the observed first arrival time, so the phase should be correct.

Thus far we have not discussed the effect of lateral velocity variations. Several studies of the velocity structure in the region indicate that the amount of lateral velocity variation is substantial [*Mayer-Rosa*, 1973; *Mooney and Luetgert*, 1982; *Cormier and Spudich*, 1984; *Blümling et al.*, 1985; *Mooney and Colburn*, 1985]. Each of these studies found a low velocity zone associated with the Calaveras fault. We assume that the velocity structure is laterally homogeneous; however, we find evidence of lateral velocity variations affecting the strong motion data. The only correction we make is to allow offsets in the trigger times for each station as discussed in a subsequent section. The effects of a smoothly-varying, laterally-heterogeneous structure could be included using techniques outlined by *Cerveny et al.* [1987] or *Cormier and Beroza* [1987], (Appendices A, B).

To account for time delays caused by the apparent lateral velocity variations, we allow the trigger times of the instruments to vary. The trigger times are adjusted so that the initial *S* wave from the hypocenter arrives at the time predicted by the assumed velocity structure. The resulting trigger times and the actual trigger times expressed in seconds after the origin time are listed in Table 4.1. The BKS instrument is continuously recording, and no trigger time correction was applied. Most of the differences between the observed and calculated trigger times are small. The exception is station HVR located in Halls Valley, a pull-apart basin [*Page*, 1982]. The low seismic velocities of the sedimentary fill of the basin account

for the large delay in arrival time. Similar large delays were found by *Mayer-Rosa* [1973] for *P* waves from local earthquakes recorded at stations along the Calaveras fault in this region.

TABLE 4.1 Trigger Times

Station	Observed	Calculated
ADD	4.35	4.22
CLD	5.60	6.00
G06	7.70	7.48
HVR	3.10	1.83
IBM	-	3.70

The data we use exhibit effects that are apparently due to lateral heterogeneities in seismic velocities. We have chosen to model these records because they have relatively simple waveforms and are close enough to the source that the approximation in equation (2.17) should be valid. Because we do not completely account for the effects of lateral heterogeneities, there is the possibility that the source model that we obtain is inaccurate or biased. This is particularly true for data obtained from stations in the fault zone where focusing may occur. It is hoped that by modeling data both from stations within the fault zone and from stations adjacent to it, the effects of lateral heterogeneities on pulse amplitudes will not destroy our resolution of the rupture behavior. In our sensitivity tests we apply our technique to synthetic data sets with large random perturbations to arrival time that simulate the effects of lateral heterogeneities.

In this study we have not attempted to resolve dip-slip motion on the fault plane. The assumption that relative slip during the main shock was primarily right-lateral strike-slip is

supported by the fault plane solution for the main shock based on first motions [*Cockerham and Eaton*, 1987], the teleseismically determined moment tensor [*Ekstrom*, 1984], the focal mechanisms of aftershocks [*Michael*, 1988], and the geodetic data [*Prescott et al.*, 1984].

In equation (2.22) we assumed that the slip velocity function can be represented as a product of a spatial dependence $s(y)$ and a temporal dependence $\dot{f}(t)$. This allows the time dependence of slip after the rupture front passes to be taken out of the integrand in equation (2.23). In order to simplify the data reduction, we deconvolve the assumed time function from the displacement records. This procedure removes the convolution from equation (2.23) when calculating theoretical seismograms.

The source time dependence that we choose to deconvolve is the truncated inverse square root of time singularity (2.22). The source time dependence is calculated as described in chapter 2 and the deconvolution is performed before decimation so that the introduced acausality is negligible.

Figure 4.9 shows the results of such a deconvolution applied to the y (240°) component of the HVR and CLD displacement records. For different values of the rise time the shape of the pulses differs substantially. For very short rise times, $\dot{f}(t)$ is of very short duration, and the data look similar to the displacement data. For longer values of the rise time, $\dot{f}(t)$ is more broad so that after deconvolution the data are richer in high frequencies. In the limit of an infinite rise time the deconvolution is equivalent to a half-order derivative [*Spudich and Frazer*, 1984].

The stations CLD and HVR are located very close to the fault plane (Figure 4.3) but beyond the limits of most of the faulting, as indicated by the extent of the aftershock zone. The initial S wave from the hypocenter is the first large positive pulse at about 2 s after trigger time at HVR and at about 3 s after trigger time at CLD. The S waves from the second source [*Bakun et al.*, 1984; *Uhrhammer and Darragh*, 1984; *Abrahamson and Darragh*, 1985; *Hartzell and Heaton*, 1986] arrive about 10 s after the trigger time at HVR and 4 s after trigger time at CLD. For right-lateral slip, S-wave displacement pulses at these stations for

the y component should be one-sided (positive for HVR and negative for CLD) once the source time function is deconvolved. However, for rise times longer than about 0.2 s, the pulses become two-sided when the deconvolution is performed (Figure 4.9). The swings in the two-sided pulses are opposite to the expected sense of motion and are too sharp to be attributed to errors in the instrument response or to side lobes of the band-pass filter. A source time function with a longer rise time and stronger healing phase might fit the data, but this would disagree with crack models of $\dot{f}(t)$ [e.g., *Rice*, 1980]. Another possible explanation is that the Green's functions are two-sided for these receivers; however, we find that a short rise time is consistent with the teleseismic estimate of the seismic moment.

We have attempted to satisfy both considerations by choosing a rise time with the form of the time dependence of slip after rupture based on crack models and the polarity expected from right-lateral faulting at stations HVR and CLD. This is done by using a 0.2-s rise time. The data are sensitive to the effect of rise time only for regions of the fault where the two pulses seen at HVR and CLD originate. It is difficult to constrain the rise time for the rest of the fault. In addition, if the rupture is strongly heterogeneous, the fault may slip more than once, and our assumption about the time dependence of slip would be violated. However, we can check the validity of our assumption by comparing the seismic moment estimated by our technique with the teleseismically estimated seismic moment. The seismic moment that we obtain for the faulting model will be too large if we assume too long a rise time and too small if we choose a rise time that is too short. The results from the inversion discussed below indicate that a rise time of 0.2 s is consistent with teleseismic estimates of the moment.

This is not the first time that very short rise times have been inferred from strong motion data. *Aki* [1968] was able to model successfully a near-field record of the Parkfield earthquake using an infinitesimal rise time. *Bouchon* [1978] noted that a rupture consisting of many small cracks with a short rise time fit the San Fernando earthquake records better than a smoothly propagating crack. *Hartzell and Heaton* [1986] used a triangular slip-velocity function of 0.3-s duration to model the Morgan Hill earthquake.

The rise time on an earthquake fault is often assumed to be limited by the extent of the slipping region. A 0.2-s rise time suggests that the rupture zone was very narrow. Assuming the width of the fault controls the rise time, the approximate relation of *Day* [1982*a*] for a rectangular fault of width W and rupture velocity v_r is

$$t_d = \frac{W}{2v_r} \tag{4.1}$$

Using a value of the rupture velocity that we obtain in the next section and applying equation (4.1) to the Morgan Hill earthquake indicates that the width of the fault at the sources of the two pulses is about 1 km. This is significantly less than the 10 km width of the aftershock zone [*Cockerham and Eaton*, 1987]. In our rupture models we have found that the width of the region of large slip is of the order of 6 km, which is still considerably larger than the estimate based on the rise time.

A possible explanation of this observation is that there are barriers distributed over the fault that do not rupture in the earthquake [*Das and Aki*, 1977]. In this model the distance between barriers, rather than the total fault width, determines the rise time. If barriers are distributed uniformly over the fault, the rise time will be approximately uniform and very short. For wavelengths longer than the barrier interval, a simple delta function will describe the slip rate function adequately.

Another possibility is that the width of the rupture zone does not control the rise time. An alternative explanation is that the heterogeneity of the rupture is causing the rise time to vary. In spontaneous rupture models of a prestressed shear crack, *Day* [1979] found that slip functions in regions of high prestress were of shorter duration than those in regions of low prestress. This would suggest that the short rise times inferred for the Morgan Hill earthquake reflect the higher stress before the earthquake at the hypocenter and at the source of the second pulse.

It should be emphasized that the although short rise times are required by the data, the nature of the time dependence that we have chosen in equation (2.22) is not. We could probably fit the data as well with a boxcar time dependence. We adopt the time dependence in equation (2.22) because it is no more complicated than the boxcar time dependence used by previous investigators and because it is consistent with crack models of rupture propagation and can be used to estimate a physically important quantity, the shear fracture energy (Chapter 5).

Sensitivity Tests

Before inverting the data to obtain a rupture model, we applied the inversion technique to a set of synthetic data generated for two known faulting models and tried to recover the original models. The stations and fault geometries are identical to those for the Morgan Hill earthquake. The degree to which the original models are recovered gives us some idea of the resolution of the method and the degree to which trade-offs occur between slip amplitude and rupture time for the source-receiver geometry. In each test case the assumed starting model had the correct average rupture velocity; however, the initial estimate of the slip distribution was smooth with a very small slip amplitude.

To make the simulation more realistic, we added two kinds of noise. The first kind of noise is a random component of isochrone time that varies smoothly over the fault and is different for each station. This was introduced when the synthetic data seismograms were calculated by equation (2.17). It simulates errors in the velocity model and the effect of an irregular rupture front. The amplitude of the random component is $\pm$ 0.5 s. In addition, a component of white noise with half the power of the synthetic data seismograms was added. Thus the overall signal to noise ratio in the test cases is less than 2:1.

In the first model, rupture propagates smoothly out from the hypocenter at 0.8 times the shear wave velocity to fill the aftershock zone (Figure 4.10). A region of high slip is centered 15 km along strike from the hypocenter and has a peak slip of 270 cm compared

with 27 cm of slip for most of the rest of the fault. Very little slip occurs to the northwest of the hypocenter. The total seismic moment is 2.2 x 10^{18} Nm.

For the first test case the region of high slip is recovered in approximately the correct location along the fault, although the vertical extent is not well resolved (Figure 4.11). The magnitude of the highest slip recovered is 180 cm, which is substantially less than the highest slip in the original model of 270 cm. The region of high slip is broader in the inversion result, compensating for the lower peak slip values. Most of the region of uniform slip is recovered, although it is somewhat irregular. The region of low slip to the northwest of the hypocenter is recovered in the model. The seismic moment of the model is 2.8 x 10^{18} Nm compared with 2.2 x 10^{18} Nm for the original model. Perturbations to rupture time are not substantial, although they tend to be larger near the region of high slip.

In the second model the slip distribution, seismic moment, and average rupture velocity are the same, but the rupture front is temporarily delayed at the region of high slip (Figure 4.12). The rupture front encircles the high slip region and then ruptures inward. This model is somewhat similar to what may have happened during the real earthquake.

For the second test case the region of high slip and the delay in rupture time are recovered at approximately the correct position along the fault (Figure 4.13). The deviation from smooth rupture is centered the correct distance along strike but is not well resolved vertically and is of smaller amplitude than in the original model. Also, the horizontal extent of the perturbations is not as large as in the original model. As a result, the anomaly appears pinched in the along-strike direction relative to the original model. The variation of the model parameters with depth is slower than in the original model, and the variation with distance along strike is more rapid. The reason for the poor vertical resolution is that isochrones for most of the fault are nearly vertical. Data residuals are back projected as perturbations to model parameters onto isochrones and tend to be smeared out vertically. When this happens, the amplitude of the perturbations to rupture time decreases because the pulse is broadened by the larger extent of the slip anomaly. Larger perturbations to the rupture time for the resolved

slip distribution would not fit the data. The problem of poor vertical resolution has been encountered before in seismic ray tomography [e.g., *Humphreys et al.*, 1984]. In that case, velocity anomalies were smeared out vertically on rays. For the seismic source problem the vertical resolution would be improved if we had more stations located close to the fault or used stations at teleseismic distances [*Hartzell and Heaton*, 1983]. The maximum value of slip in the model is 160 cm, which is less than the maximum slip of 270 cm. However, the total moment of 2.1×10^{18} Nm is in close agreement with the original model.

Although it is much more irregular than in the original model, the large region of uniform slip is recovered for parts of the fault that are not near the large slip anomaly in both test cases. For regions of the fault near the slip anomaly the smoothly varying component of the slip is not as well resolved. This is due to trade-offs between slip amplitude and rupture time and to the fact that the data are band-limited. There is also a region from 20 to 25 km along strike that has substantially larger slip in the second test case than in the original model.

The two test cases demonstrate the ability of the method to distinguish variations in slip from variations in rupture time. Variations in slip and rupture time trade off strongly for a single station [*Spudich and Frazer*, 1984]. The ability of the method to distinguish between these two quantities is probably a reflection of the good azimuthal coverage of stations for the Morgan Hill earthquake. This is important because models that we obtain using the real earthquake data indicate that there are strong variations in both slip and rupture time.

In each of the test cases the principal features of the original model were recovered, and variations in slip were distinguishable from variations in rupture time. Although these results are encouraging, they are not necessarily conclusive. The problem is underdetermined, and recovery of the original model depends on the correct choice of the norm to minimize [*Olson and Anderson,* 1988]. The first-derivative norm that we minimize is a reasonable one for the test cases that we have analyzed. If this smoothing norm is not appropriate for the earthquake, the resolution will be poorer than the the test cases indicate. The approach of

minimizing spatial gradients in slip is essentially a minimization of the static shear stress change.

Constant Rupture Velocity Model for the Morgan Hill Earthquake

We first attempt to fit the data for the Morgan Hill earthquake with a model in which the rupture front propagates smoothly away from the hypocenter at a fixed fraction of β, the shear wave velocity, to fill the aftershock zone. In this model the rupture velocity is held constant, while the slip intensity is allowed to vary. Such a problem is linear since the rupture time is assumed *a priori*. The inversion procedure is a weighted back-projection of the data residuals onto isochrones in exactly the same manner as ray tomography back-projects travel time residuals along the ray path.

Values of rupture velocity used ranged from 0.5β to 1.0β. We define the weighted variance reduction as

$$\Delta\sigma^2 = \left(1 - \frac{(d - g(m))^T C_d^{-1} (d - g(m))}{d^T C_d^{-1} d} \right) \text{x } 100\% \qquad (4.3)$$

where C_d^{-1} is the inverse of the data covariance matrix. The model that best fits the data has a rupture velocity of 0.7β and a variance reduction of 41% (Figure 4.14). The rupture model for this case is shown Figure 4.15, and the fit to the data is shown in Figure 4.16. The model has a seismic moment of 2.4 x 10^{18} Nm. The seismic moment determined from the strong motion data is similar to that obtained from the teleseismic data of 2.0 x 10^{18} Nm [*Ekstrom*, 1984], indicating that our assumption of a short rise time is appropriate. The fit to the data tends to be better for the y component than it is for the x component. This is probably due to the fact that for most of the stations the x component is nearly nodal, whereas the y component is on a lobe of the radiation pattern. For this reason the x component will be much

more sensitive than the y component to a small change in the take-off angle or orientation of the fault.

The slip distribution consists primarily of a zone of large slip extending from the vicinity of the hypocenter to about 8 km along strike at depths ranging from 8 to 12 km. There is a small region of concentrated moment release that is approximately 1 km wide located 13 km along strike from the hypocenter. This region of large slip generates the large, late pulse at HVR. The pulse is much broader in the theoretical seismograms than it is in the data. This is a consequence of strong directivity that occurs because the rupture front is assumed to propagate uniformly away from the hypocenter. Directivity broadens and lowers in amplitude the pulses at BKS and HVR. Using the assumption of a uniform rupture velocity, it is very difficult to produce large second pulses at these stations, although it is possible to fit the data at the other stations fairly well. The model obtained by *Hartzell and Heaton* [1986] does not fit the second pulse at HVR very well. This is probably because they assumed that the direction of rupture was away from HVR, and although they did allow each subfault to slip up to 3 times, they assumed that each time it was rupturing in the same direction, away from HVR. We conclude that smooth rupture propagation is inconsistent with the HVR and BKS data.

Variable Rupture Velocity Model for the Morgan Hill Earthquake

We attempted to fit the data with a variable rupture velocity model in which both the rupture time and slip intensity are allowed to vary. The starting model in each case was smooth in both slip intensity and rupture time. Since this problem is nonlinear, the result will be sensitive to the starting model. Different starting models were tried with the value of rupture velocity ranging from 0.5 to 1.0 times the local shear wave velocity. The model that best fit the data had an average rupture velocity of 0.8β. This is a higher average rupture velocity than in the best fitting model for the constant rupture velocity inversion. The

variable rupture velocity model obtained from the linearized inversion is shown in Figure 4.17. The fit to the data is shown in Figure 4.18.

The model in Figure 4.17 fits the data with a weighted variance reduction of 56%, indicating that the fit to the data is considerably better than for the variable slip inversion for which the weighted variance reduction was 41%. The difference is due in part to the enhanced fit to the large late pulse at HVR and BKS (Figure 4.18). The second pulse at HVR is now reproduced in the theoretical seismograms. The seismic moment of the model is 2.7 x 10^{18} Nm, which is in approximate agreement with the teleseismic estimate of 2.0 x 10^{18} Nm.

A second pulse is also evident in the theoretical seismograms for BKS, although it is smaller in amplitude than the data. This may be due to an inadequate upper mantle velocity structure. BKS is also located near a radiation pattern node for *P* waves, and a small change in the strike at the southeast end of the rupture zone, as suggested by the surface trace and the aftershock zone, would strongly affect the *P*-wave amplitudes at BKS.

The slip distribution in the model is strongly heterogeneous. A region of substantial slip extends from the hypocenter to about 10 km along strike at 6-12 km depth. It is similar to a more compact region of large slip in the variable slip model (Figure 4.15).

A small region 14 km along strike has a peak slip of over 200 cm. The region from 14 to 17 km along strike and 8 to 12 km in depth represents 4% of the total fault area but is responsible for 12% of the total moment released in the earthquake. The region of low slip surrounding this area may be an artifact of poor resolution as in the synthetic test case (Figure 4.13), but the lack of slip at depths less than 6 km is probably real. A region of large slip from 20 to 25 km along strike may be an artifact since excessive slip was obtained there in the synthetic test case. In our model, rupture propagates smoothly away from the hypocenter for 13 km. The rupture front is delayed from a depth of about 7-12 km. Rupture occurs ahead of the region of high slip as can be seen in Figure 4.17 where the closed 5.25-s contour surrounds a local minimum of rupture time. The region of high slip ruptures when

the surrounding fault has ruptured. This causes strong directivity back toward the hypocenter, consistent with the large late pulses at HVR and BKS.

Such a rupture model is similar to numerical simulations of shear rupture on a heterogeneous fault plane. *Das and Aki* [1977] modeled rupture on a fault plane with high strength barriers and found that rupture could occur discontinuously beyond the strong regions which may subsequently rupture or remain unbroken. *Day* [1982*b*] modeled the rupture of a fault with constant strength but nonuniform prestress. He found that rupture was very complex and that at some points on the fault the rupture jumped, leaving unbroken areas behind, which subsequently rupture. *Das and Kostrov* [1983] modeled the failure of a slip resistant asperity. They found that when rupture began at the edge of the asperity, it proceeded first around the edge and then failed inward in a "double encircling pincer movement." In their model the asperity was a strong region surrounded by a stress free crack surface. *Boatwright and Quin* [1986] modeled dynamic rupture of a fault characterized by variable stress and strength. They found that rupture was occasionally discontinuous but for the most part was simply connected.

In the rupture model that we have obtained the asperity (region of large slip and delayed rupture) is encountered by a propagating rupture front. Because the asperity is encountered during unilateral rupture propagation, the directivity effects on the seismic radiation are more easily observed than if rupture had initiated at the edge of an asperity. In the model shown in Figure 4.17 the rupture front jumps discontinuously as observed in the spontaneous rupture models; however, because of the large uncertainties in our model we can not distinguish between a rupture front that encircles the asperity and ruptures inward and a rupture front that jumps across the asperity and subsequently ruptures backward.

Discussion

Although we can not resolve the details of the rupture front, the models for all choices of the rupture velocity in which the rupture time was allowed to vary exhibited similar behavior.

In each case the rupture front was temporarily impeded near Anderson Reservoir but eventually ruptured bilaterally with a large slip intensity. For this reason we believe that the strong second source of seismic radiation in the Morgan Hill earthquake represents the failure of a relatively strong section of the fault which retained more of the strain energy accumulated during the interseismic period than the surrounding regions of the fault. This hypothesis is supported by seismicity data and the fault zone geometry.

Bakun [1980] studied the seismicity of the southern Calaveras fault zone. On the segment of the fault that ruptured energetically in the Morgan Hill earthquake there was a very low level of seismicity compared with the rest of the fault. This segment of the fault was also relatively devoid of aftershocks (Figure 4.19). *Bakun* [1980] suggested that the fault might be pinned by the geometrical obstruction caused by the left step in the surface trace of the fault (Figure 4.19). Such a left step would act to increase the normal stress acting across the fault and allow greater strain energy to accumulate. When that region ruptured in an earthquake, it would be expected to have more slip. The location and extent of the region of large slip in our rupture model is somewhat uncertain due to lateral heterogeneity in the velocity structure and imperfect resolution, but it is clearly situated below the same complex segment of the fault.

Most of the aftershocks are more shallow than the regions of high slip (Figure 4.19). Regions that underwent large slip during the earthquake tend to have fewer aftershocks than regions with little or no slip. This suggests that regions of the fault that underwent large displacements during the earthquake become regions of very low stress after the earthquake. The aftershocks may have accommodated slip on regions of the fault that did not slip during the earthquake.

An interesting aspect of our rupture model is that much of the aftershock zone, especially at shallow depths, exhibits little or no slip. This observation may account for geodetic line length changes observed in the postseismic period which indicate that the amount of postseismic slip equals 130% of the coseismic slip as of February, 1986 (*W. H. Prescott,*

personal communication, 1987). The large postseismic slip may be due in part to aseismic slip of regions of the fault that did not rupture during the earthquake.

The rupture model that we obtained for this earthquake is similar in most respects to that obtained by *Hartzell and Heaton* [1986]. In our model we found a region of high slip near the hypocenter extending for 10 km along-strike. *Hartzell and Heaton* [1986] also found a region of high slip near the hypocenter, although it extended for only 5 km along strike. The location that we obtained for the strong second source coincides with the location found by *Hartzell and Heaton* [1986]. Because they allowed the fault to rupture three times as the rupture front passed, they found that the region of highest slip continued to rupture after adjacent segments of the fault had ruptured. This is similar to our observation of delayed rupture. Their model differs from ours in that rupture in their model propagated away from the hypocenter each time it occurred instead of back toward the hypocenter as in our model. In addition, the relatively late slip at the second source was at a depth of 3-6 km in their model and at a depth of 6-12 km in our model. A significant difference between the two models is the values of the peak slip amplitudes. The values of slip obtained by *Hartzell and Heaton* [1986] are systematically lower than the values that we obtained. This may be due to a stronger smoothing constraint placed on the problem by Hartzell and Heaton. The peak slip at the second source found by Hartzell and Heaton was half the peak value that we obtained; however, the extent of the region of high slip is greater in their model. The seismic moments are 2.1×10^{18} Nm for the Hartzell and Heaton model and 2.7×10^{18} Nm for our model.

Figure Captions

Figure 4.1 Aftershocks of the Morgan Hill earthquake are shown with a map of the surface trace of the Calaveras fault *Radbruch-Hall* [1974]. The hypocenter of the main shock is shown with a hexagon. From the distribution of the aftershocks [*Cockerham and Eaton*, 1987] with respect to the hypocenter it is apparent that the rupture was primarily unilateral to the southeast. The surface trace of the fault near the hypocenter is fairly linear, but approximately 15 km along strike, near ADD, the surface trace undergoes a complex left-stepping offset. Aftershocks were systematically located to the east of the surface trace of the fault. The fault plane as determined by the aftershocks appears simpler than the surface trace, and may have a change in trend from N35°W to the north of Anderson Reservoir to N29°W to the the south.

Figure 4.2 The extent of the Morgan Hill earthquake aftershock zone on the Calaveras fault is shown as a vertical line. The distance of the hypocenter along the surface trace is shown with a hexagon. The three letter station codes identify stations used in the inversion. The *y* (240°) component of acceleration for each of these stations is plotted. The accelerograms are plotted such that the offset horizontally corresponds to an offset in absolute time. The first large pulse at HVR is the *S* wave from the hypocenter which was quite close to the station. The second, larger, pulse approximately 8 seconds later originates from a zone of high slip 15 km farther away from the station. The fact that the distant source is much larger in amplitude than the closer one indicates that it is much more energetic.

Figure 4.3 The geometry is the same as Figure 4.2 except that *y* (240°) component of displacement is plotted instead of acceleration. The displacement is processed as described in the text. A second pulse that originated near ADD is apparent in stations other then HVR for the displacement records. The hypocentral *S*-wave arrival and the *S*-wave pulse from the second source are shown with arrows.

Figure 4.4 The *x* (150°) component of displacement is plotted for the stations used in the inversion. For a vertical strike-slip fault in a laterally homogeneous medium, this component should be nearly nodal for *S* waves at HVR, CLD, and G06.

Figure 4.5 The y (240°) component of displacement is plotted for the stations in the Gilroy array. G02 - G04 are located on sediments in the Santa Clara Valley. Although G06 and G07 are only a few km apart, the records at the two stations are markedly different.

Figure 4.6 The *P*-wave velocity model used in this study is a piecewise linear gradient model (solid line), which approximates the model found for the region by *Blümling et al.* [1985] (dashed line). A Poisson solid is assumed to derive S-wave velocities.

Figure 4.7 A comparison of displacement seismograms calculated using the discrete-wavenumber, finite-element method (dashed lines) with the ray theory seismograms used in this study (solid lines) is shown for a distribution of distances from a vertical strike-slip fault with a diameter of 1 km, centered at 4.5 km depth for SH and P-SV geometries. The seismograms are band-pass filtered with a 2 pole, zero-phase Butterworth filter at 0.2 and 4.0 Hz.

Figure 4.8 The same comparison as in Figure 4.7 is made for the deeper fault centered at 8.5 km depth.

Figure 4.9 The results of deconvolving an assumed value for the source time function from the displacement records at HVR and CLD are shown for different values of the rise time. For rise times longer than about 0.2 s the pulses become distinctly two-sided. Because the sign of the Green's function for this geometry is positive for HVR and negative for CLD for nearly the entire fault, such a two-sided pulse is impossible to reproduce. We have analyzed the data assuming a rise time of 0.2 s. The use of such a short rise time is substantiated by our final model because the seismic moment we obtain is similar to that obtained from GDSN data. Had we assumed a longer rise time, our estimate of the moment would have exceeded teleseismic low frequency estimate.

Figure 4.10 A side view of the slip and rupture time distribution for the variable slip model used to generate a synthetic data set. Distance units are in km. The rupture propagates outward from the hypocenter at 0.8 times the shear wave velocity to fill the rupture zone. The slip shown is the final relative offset of the two sides of the fault. Each shade covers a slip range of 40 cm. Slip is smoothly varying except for a region of high slip about 15 km along strike. Seismograms were calculated for the velocity structure and stations we used in modeling the Morgan Hill data. Noise was added to the data as described in the text such that the signal to noise ratio was less than 2:1. The data generated by the variable slip model were then inverted for slip and rupture time in an attempt to recover the original model. The degree to which the original model is recovered provides a measure of the resolution obtainable from the available data, and the deviation of the rupture time from the original model is indicative of trade-offs between rupture time and slip amplitude.

Figure 4.11 The rupture model resulting from the inversion is shown for the first test case. The vertical extent of the slip anomaly, and the slowly varying features of the slip model are fairly well resolved. The slip anomaly is somewhat broader and of lower peak amplitude than in the original model. There are small variations in rupture time, but no large anomalies.

Figure 4.12 The rupture model used for the second test case is shown. The slip model is the same as in the previous test case, but the rupture time in the region of the slip anomaly is delayed in such a way that the slip anomaly is encircled by the rupture front prior to failure.

Figure 4.13 The model of rupture time resulting from the inversion is shown for the second test case. The anomaly in slip and rupture time is spread out vertically and is of lower peak amplitude than the original model; however, a region of delayed rupture and high slip is recovered, and the estimated seismic moment is in close agreement with that of the original model (Fig. 4.12). The azimuthal coverage of stations is sufficient to distinguish between variations in slip (Fig. 4.12) and the variations in slip and rupture time shown here.

Figure 4.14 The data residual for the variable slip - constant rupture velocity inversions is shown for a range of rupture velocities with a taut cubic spline interpolation between points where it was calculated. The horizontal axis is the ratio of the assumed rupture velocity to the local shear wave velocity. A broad maximum in the variance reduction is apparent between 0.65β and 0.8β. The best fitting model was for a rupture velocity of 0.7β.

Figure 4.15 The best fitting variable slip - constant rupture velocity model is shown for an assumed rupture velocity of 0.7β. The rupture time is unchanged from the starting model. Most of the slip occurs near the hypocenter to about 8 km the the southeast. A compact zone of high slip is resolved. This results in a broad pulse in the theoretical seismograms due to the effect of directivity. The large second pulse of short duration in the data can not be fit by a model which requires uniform rupture propagation.

Figure 4.16 The fit to the deconvolved data is shown for the rupture model in Figure 4.15. The top traces are the deconvolved data, and the bottom traces are the theoretical seismograms calculated from our rupture model. The second pulse at stations HVR and BKS is not well reproduced. The amplitude of the BKS seismograms is multiplied by a factor of 40 with respect to the other records. The short duration of the second pulse can not be generated by a smoothly propagating rupture. The weighted variance reduction is 41%.

Figure 4.17 The result of the linearized inversion for slip and rupture time is shown. The best-fitting model has an average rupture velocity of 0.8β. The slip now reaches a maximum in a region about 14 km to the southeast of the hypocenter. The closed contour 15 km along strike on the rupture time plot is a local minimum of rupture time. The rupture time indicates that propagation is no longer unilateral to the southeast, but instead has a component back towards the hypocenter.

Figure 4.18 The fit to the deconvolved data is shown for the rupture model in Figure 4.17. The second pulse at HVR is reproduced with this model and is present, although quite small, at BKS as well. The weighted variance reduction for this model is 56%.

Figure 4.19 A plan view of the surface trace of the Calaveras fault [*Radbruch-Hall*, 1974] is shown above a side view of the aftershocks [*Cockerham and Eaton*, 1987], projected onto the assumed fault plane, and a side view of the slip distribution estimated in this study. The region of highest slip corresponds to a segment of the fault for which the surface trace is quite complex. Regions of high slip tend to have fewer aftershocks than regions where little or no slip occured.

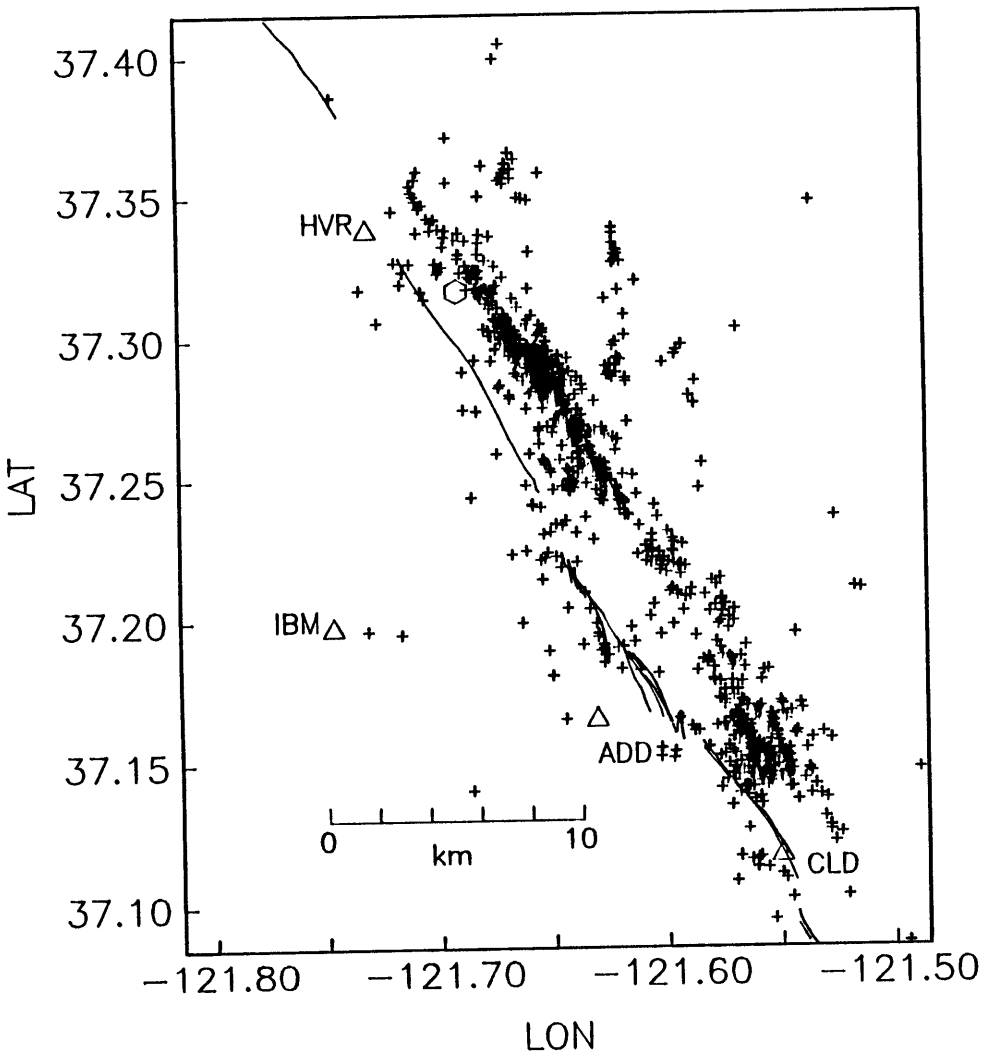
37.40
37.35
37.30
37.25
37.20
37.15
37.10
LAT
HVR
IBM
ADD
CLD
0
km
10
−121.80
−121.70
−121.60
−121.50
LON

Figure 4.1

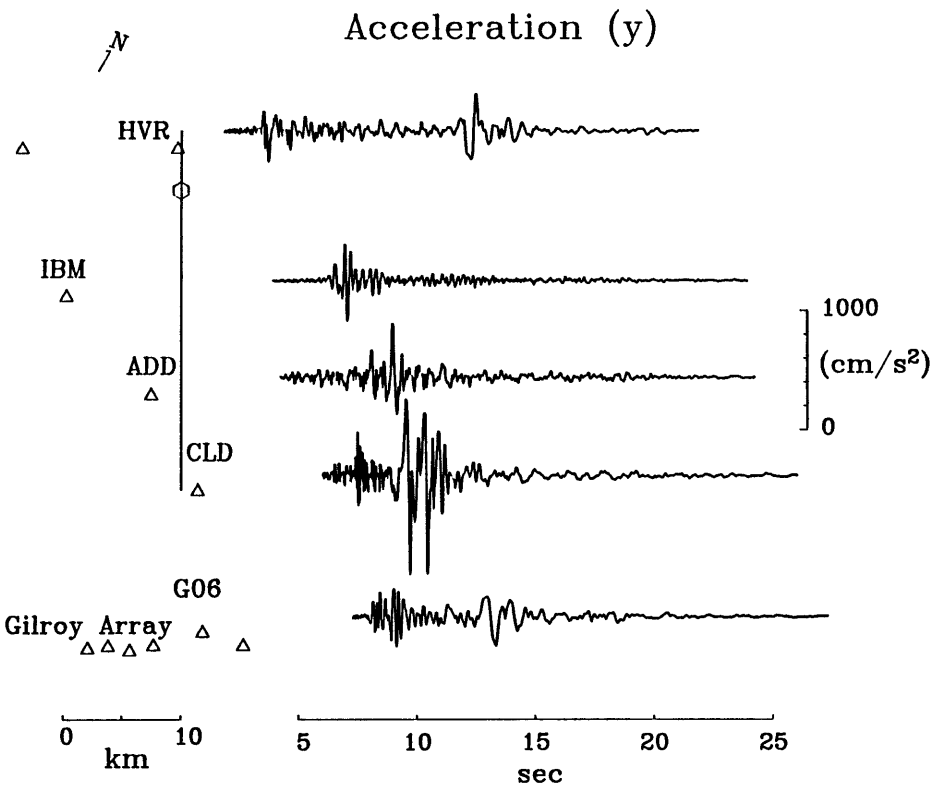
Acceleration (y)
N
HVR
IBM
ADD
CLD
G06
Gilroy Array
1000
(cm/s²)
0
0
10
km
5
10
15
20
25
sec

Figure 4.2

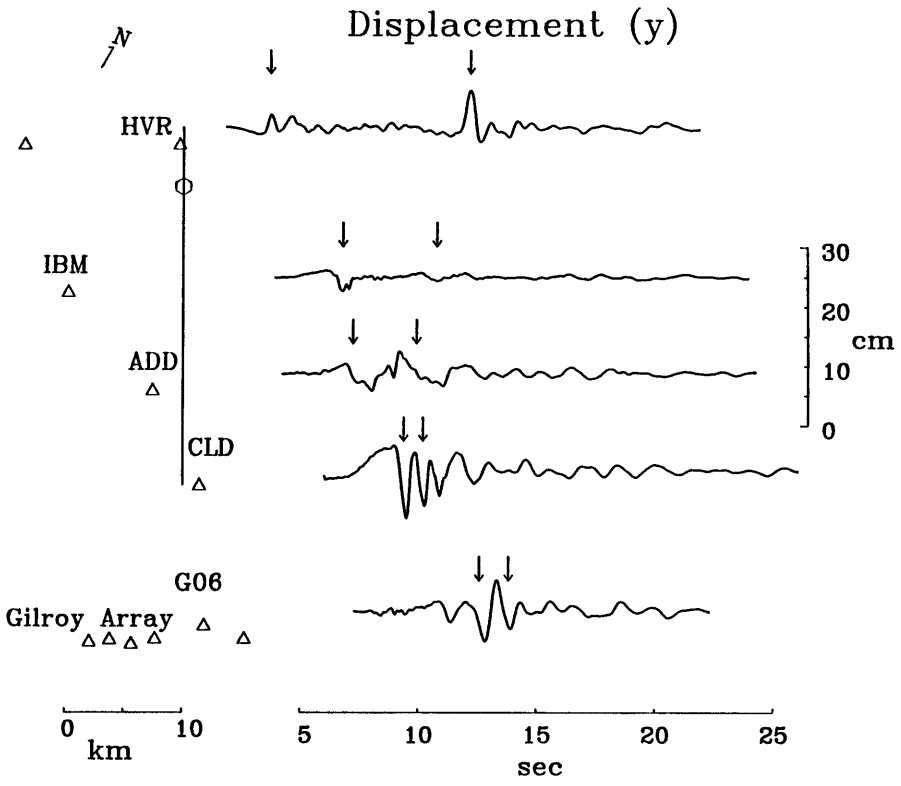
Displacement (y)
N
HVR
IBM
ADD
CLD
G06
Gilroy Array
30
20
10
0
cm
0
10
km
5
10
15
20
25
sec

Figure 4.3

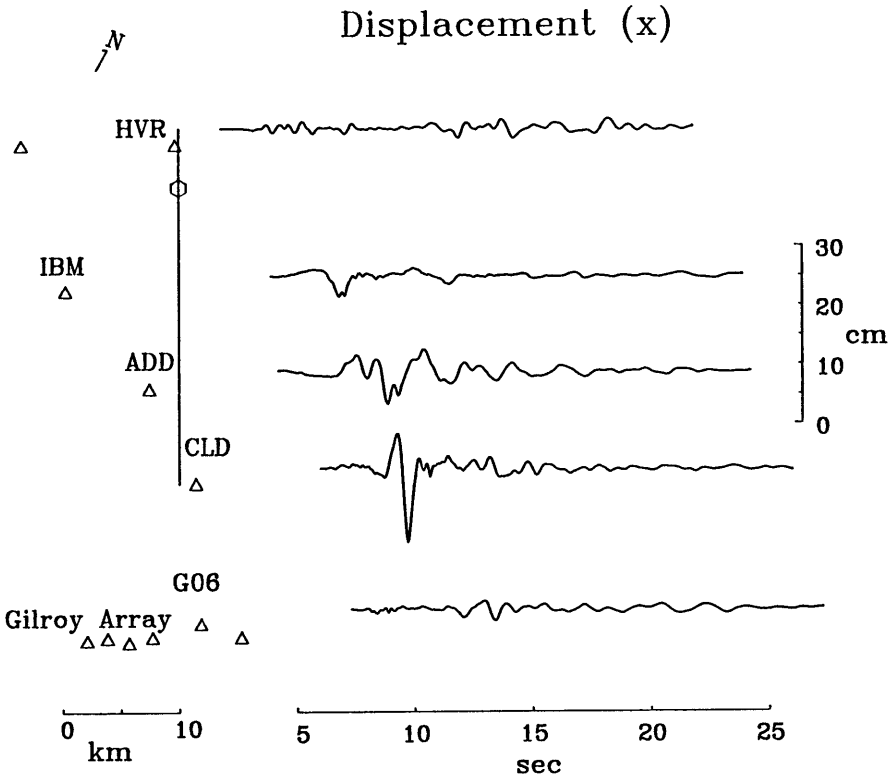
Displacement (x)
N
HVR
IBM
ADD
CLD
G06
Gilroy Array
30
20
cm
10
0
0
10
km
5
10
15
20
25
sec

Figure 4.4

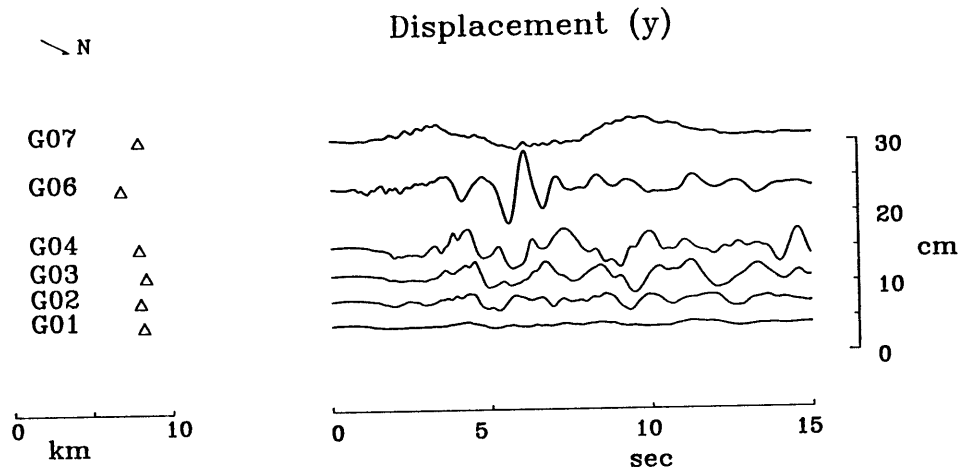
Displacement (y)
N
G07
G06
G04
G03
G02
G01
0
10
km
0
5
10
15
sec
30
20
10
0
cm

Figure 4.5

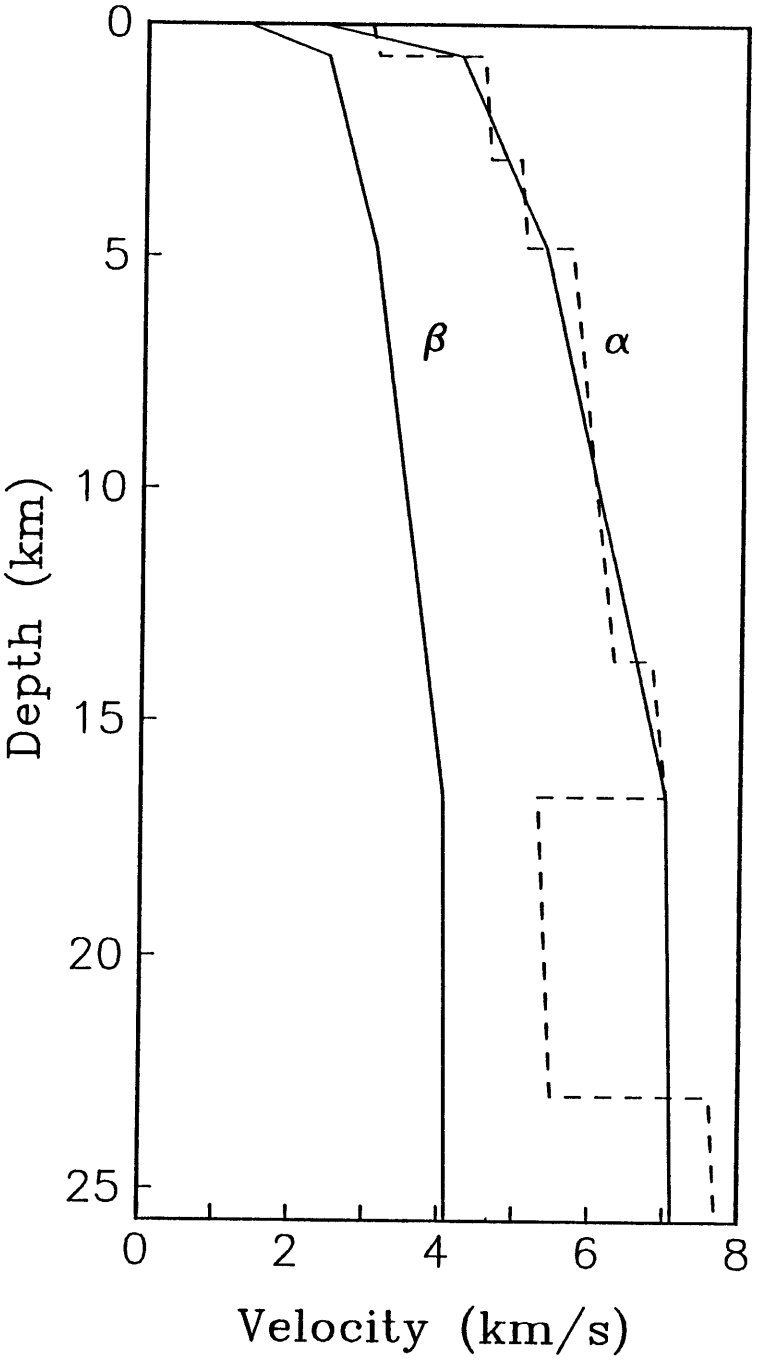

Figure 4.6

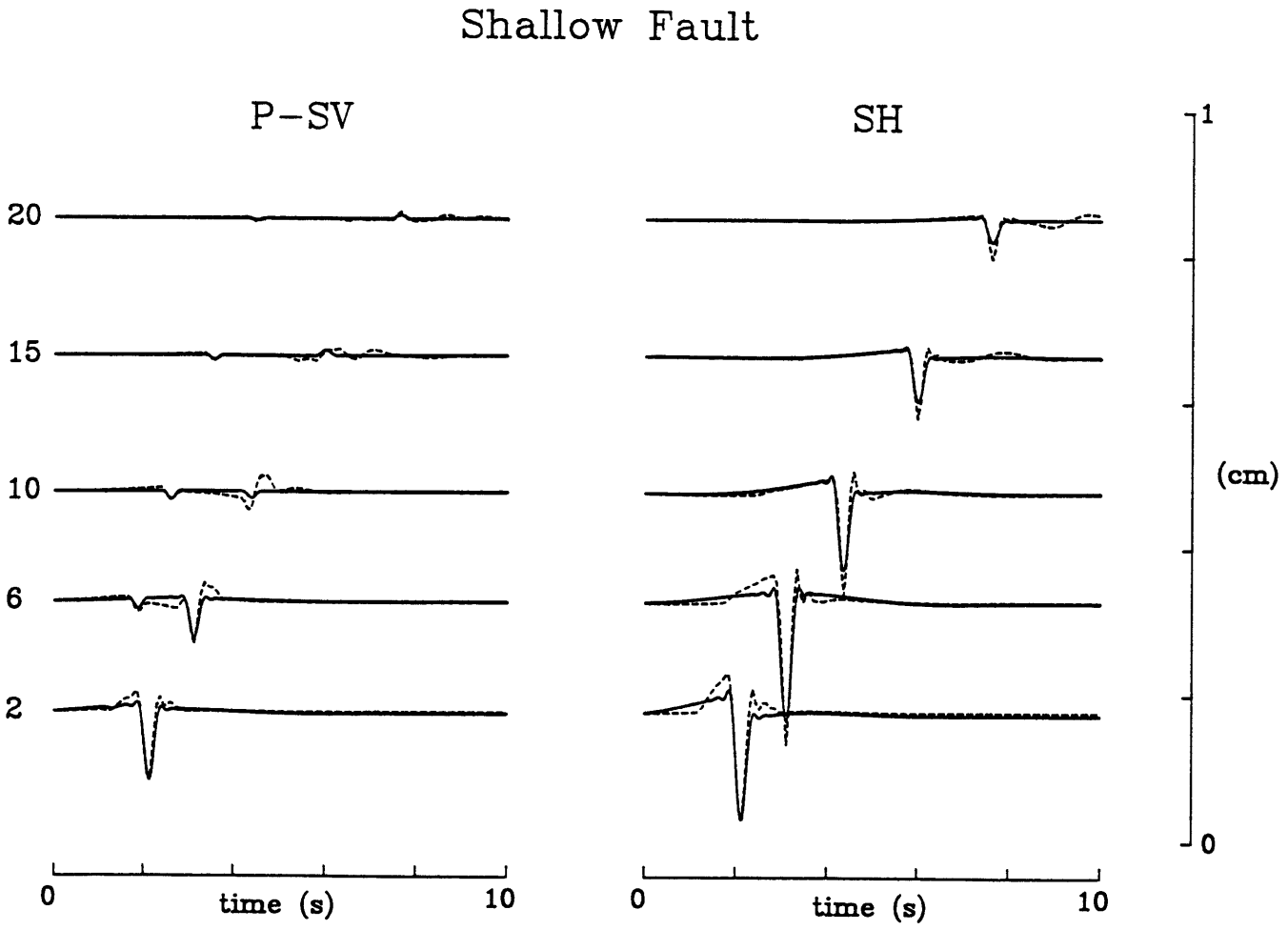

Figure 4.7

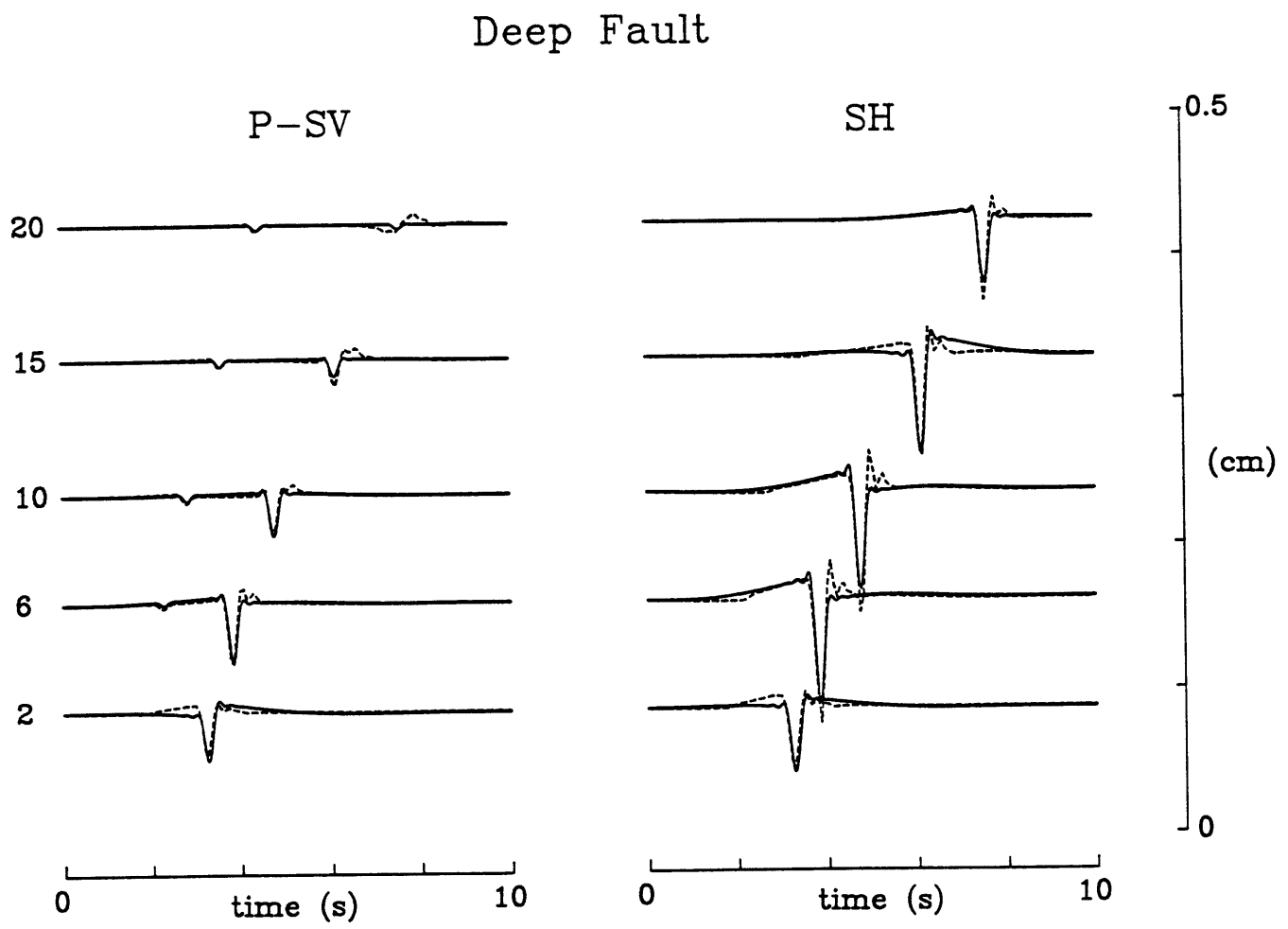

Figure 4.8

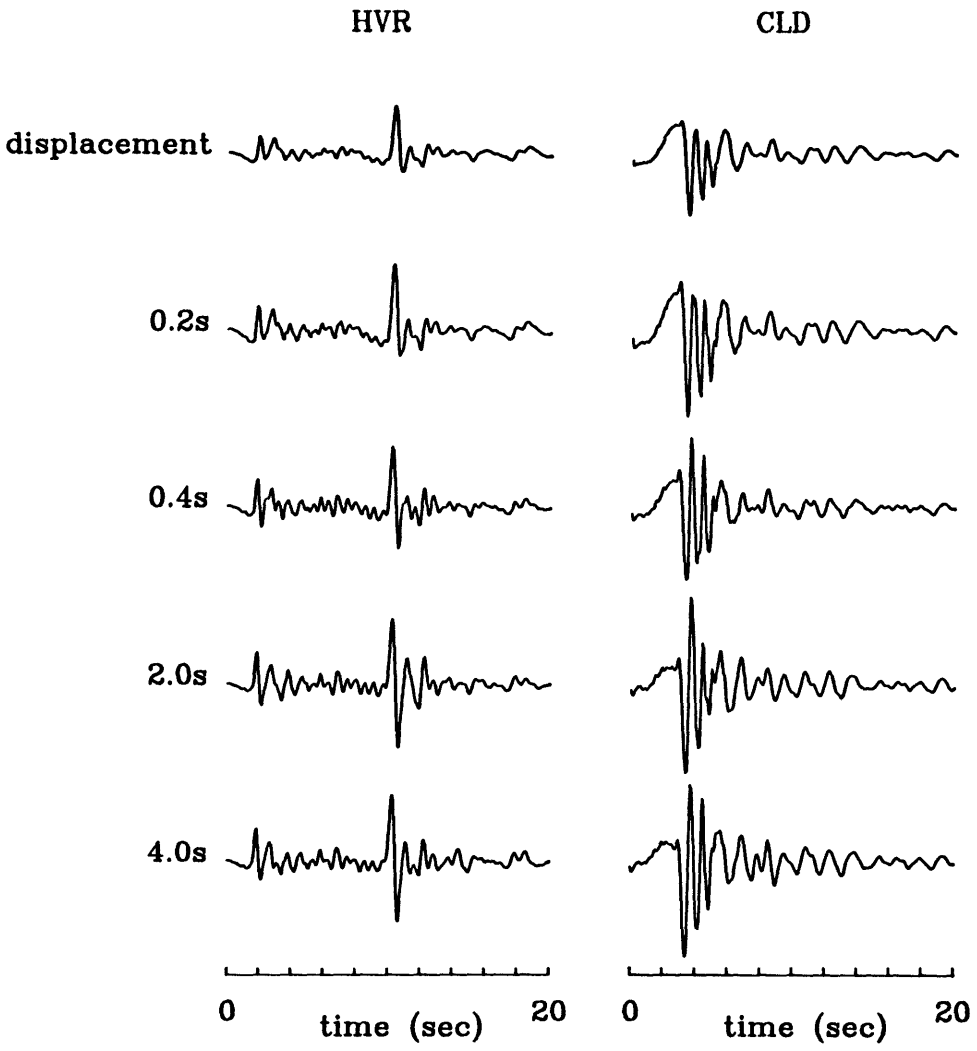
HVR
CLD
displacement
0.2s
0.4s
2.0s
4.0s
0
time (sec)
20
0
time (sec)
20

Figure 4.9

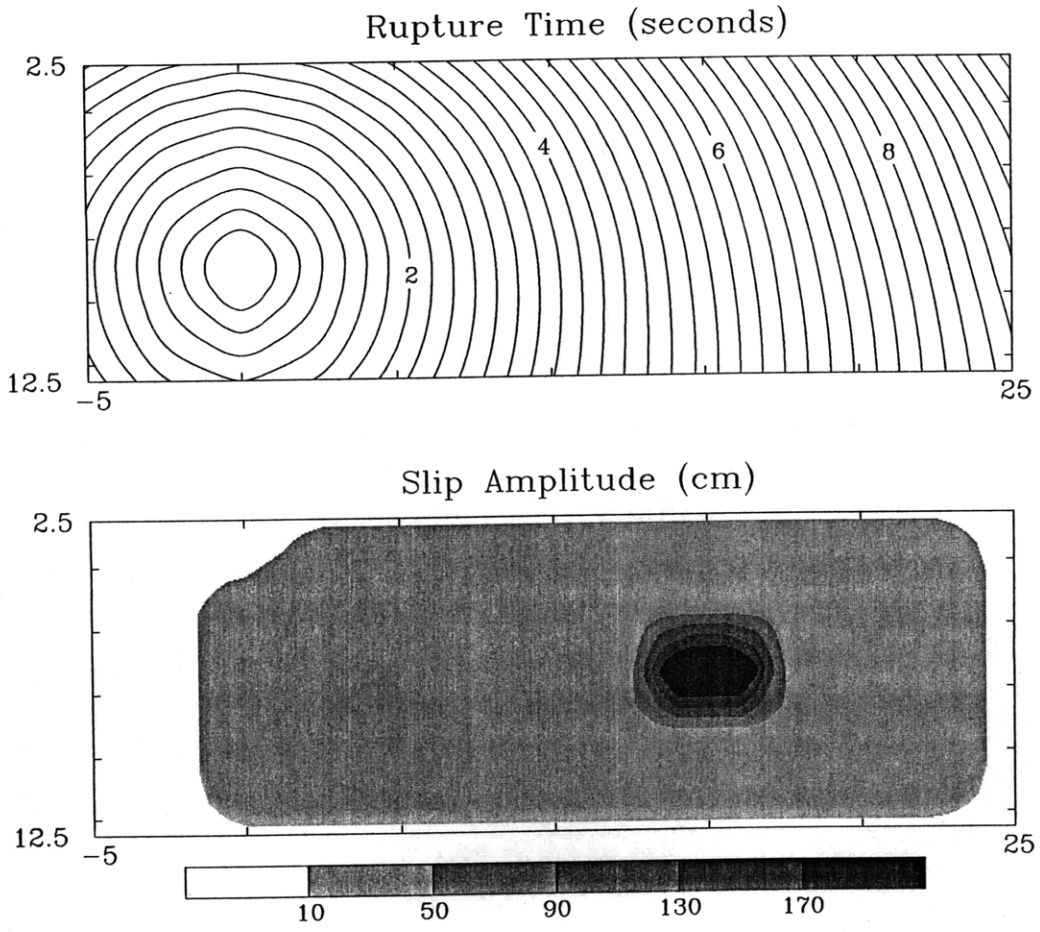
Rupture Time (seconds)
2.5
12.5
-5
25
2
4
6
8
Slip Amplitude (cm)
2.5
12.5
-5
25
10
50
90
130
170

Figure 4.10

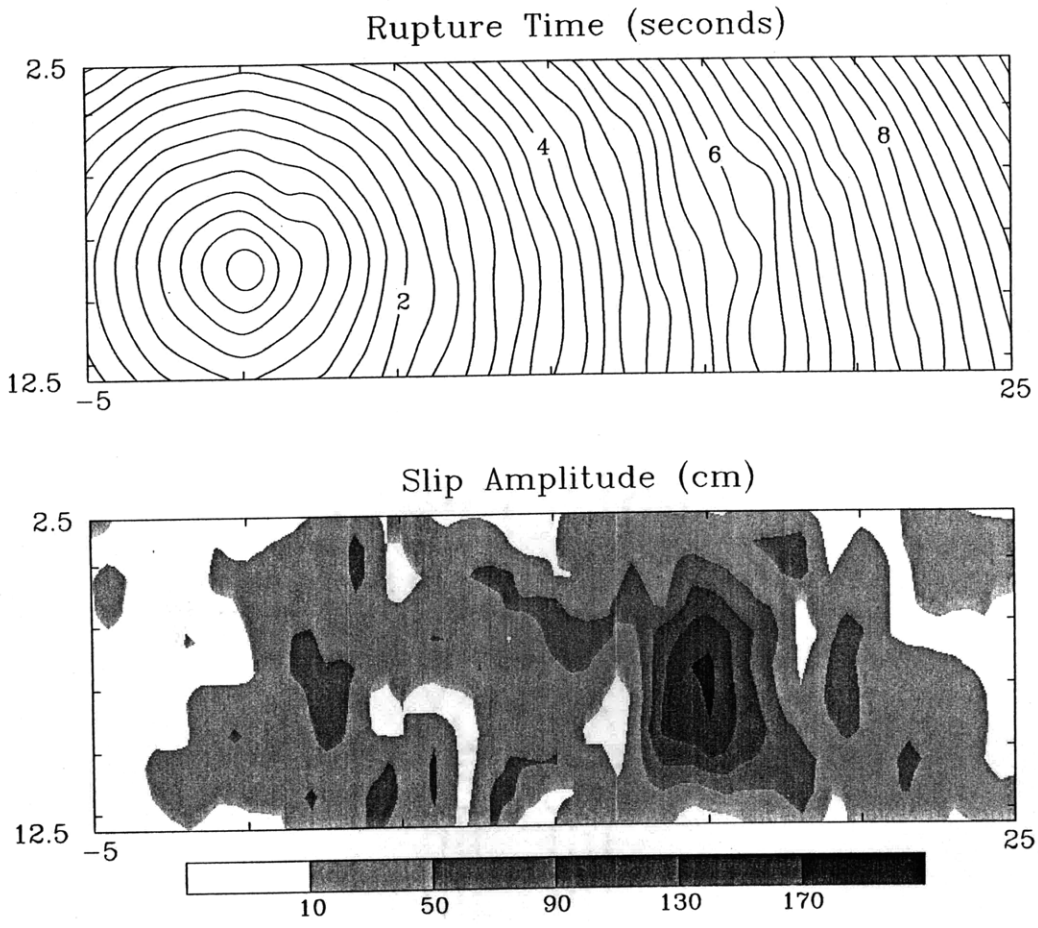
Rupture Time (seconds)
2.5
12.5
−5
25
2
4
6
8
Slip Amplitude (cm)
2.5
12.5
−5
25
10
50
90
130
170

Figure 4.11

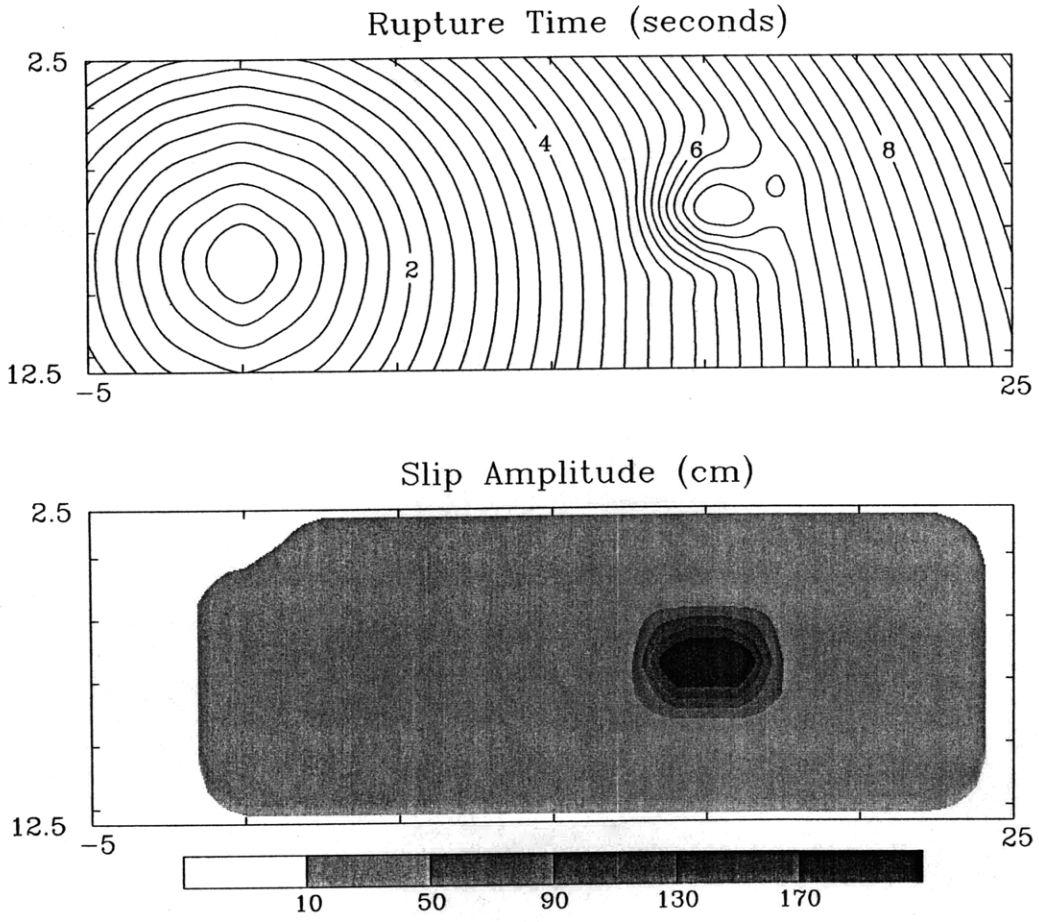
Rupture Time (seconds)
2.5
12.5
−5
25
2
4
6
8
Slip Amplitude (cm)
2.5
12.5
−5
25
10
50
90
130
170

Figure 4.12

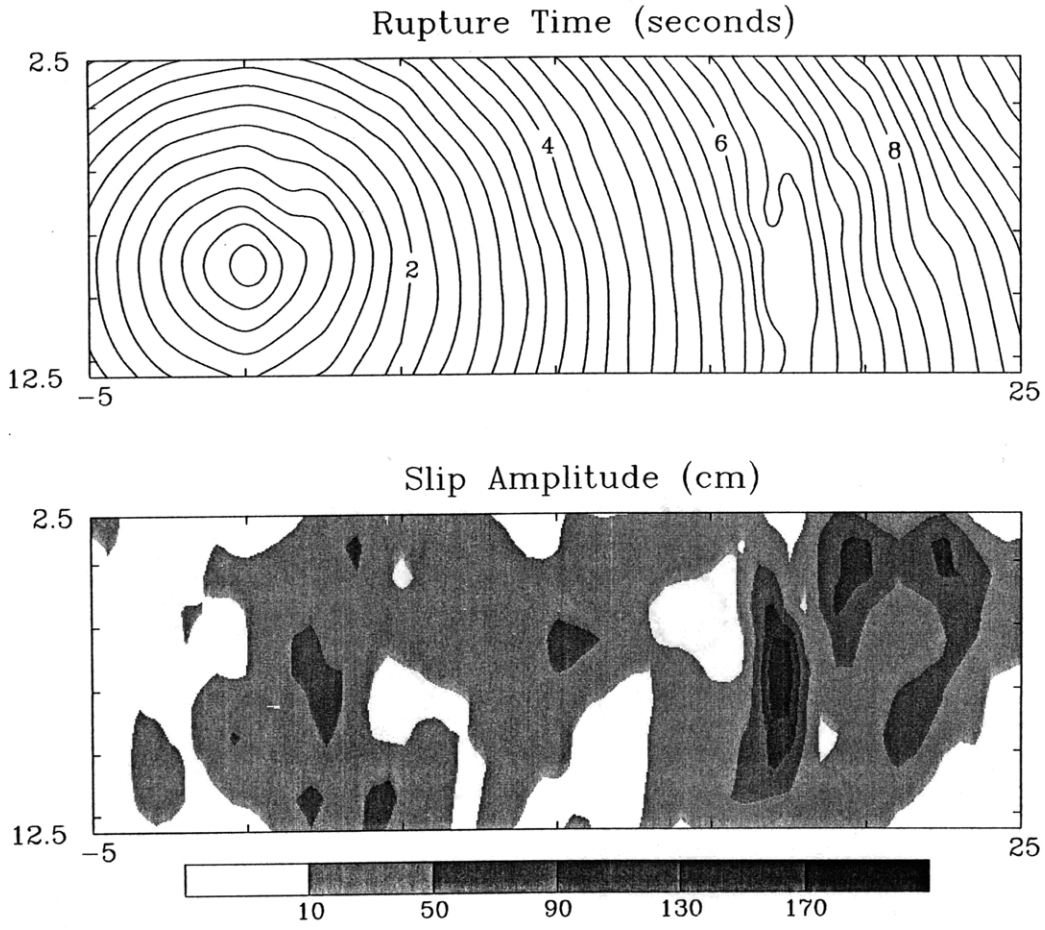
Rupture Time (seconds)
2.5
12.5
−5
25
2
4
6
8
Slip Amplitude (cm)
2.5
12.5
−5
25
10
50
90
130
170

Figure 4.13

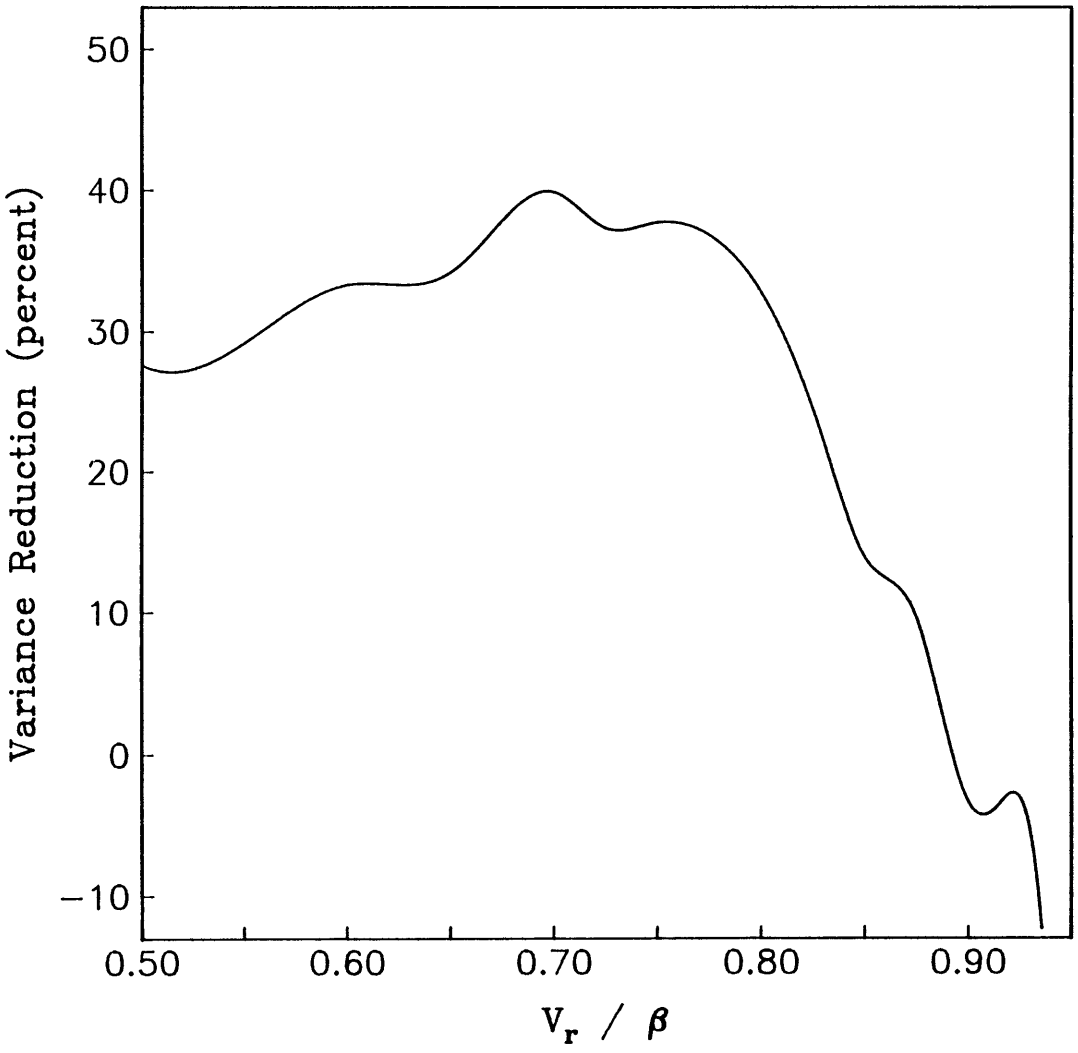
50
40
30
20
10
0
−10
Variance Reduction (percent)
0.50
0.60
0.70
0.80
0.90
V_r / β

Figure 4.14

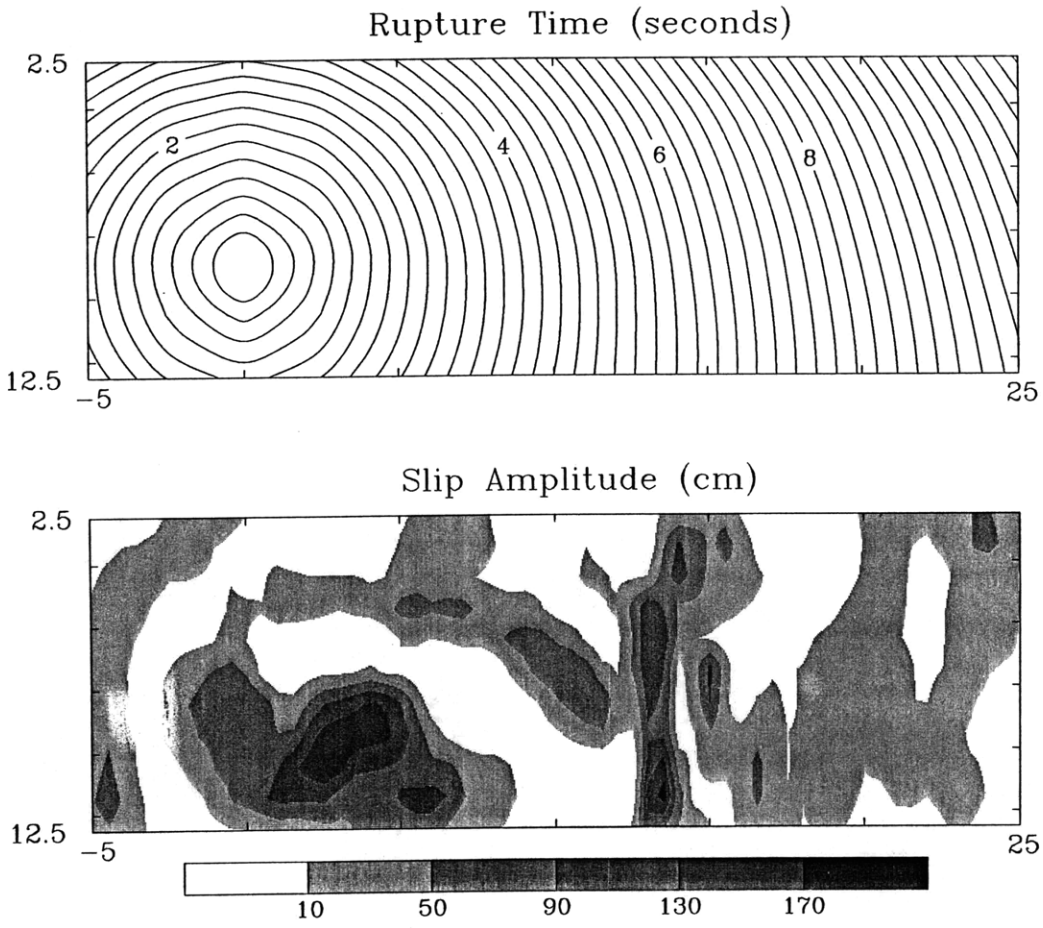
Rupture Time (seconds)
2.5
12.5
−5
25
2
4
6
8
Slip Amplitude (cm)
2.5
12.5
−5
25
10
50
90
130
170

Figure 4.15

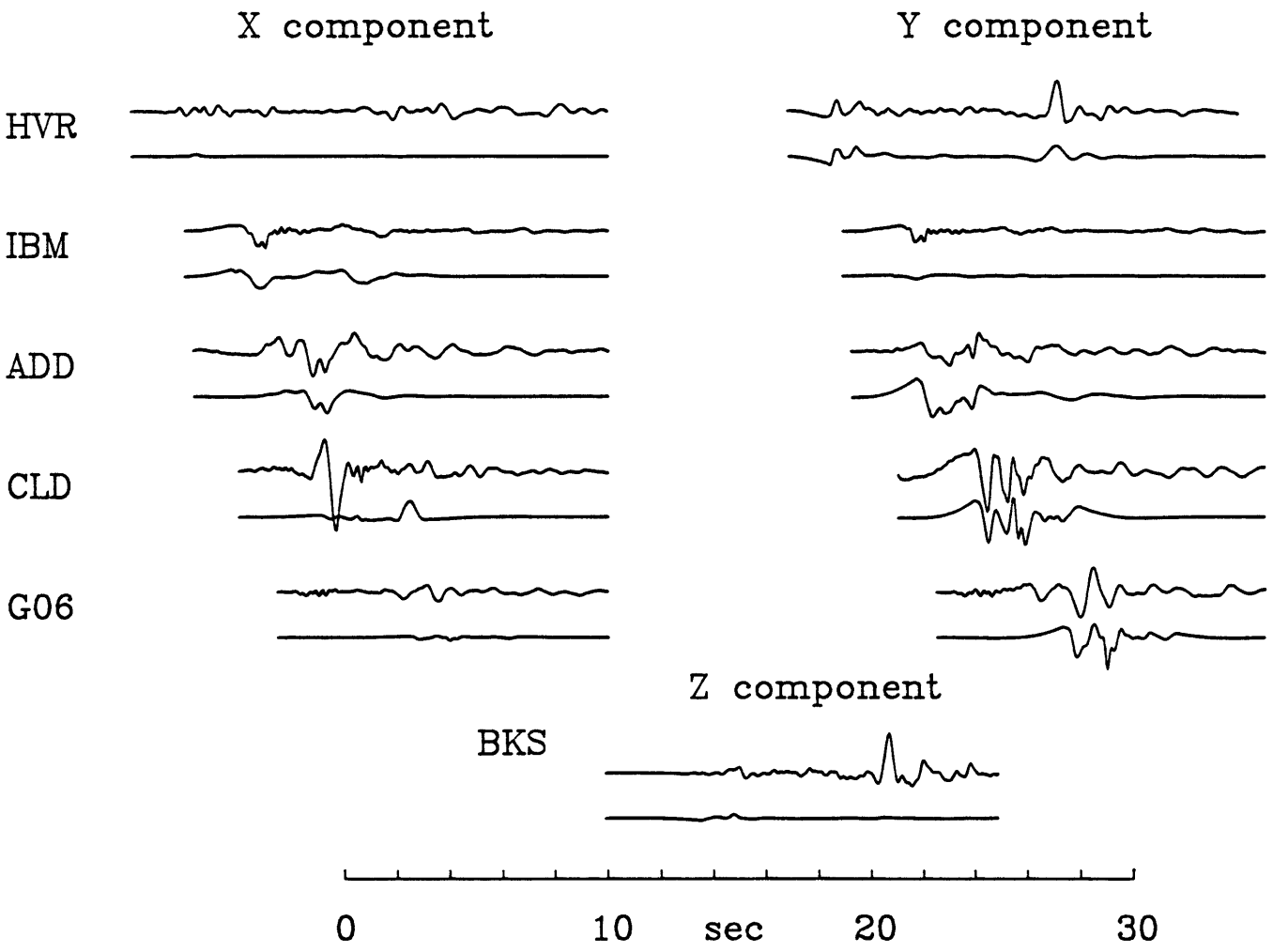
X component
Y component
HVR
IBM
ADD
CLD
G06
Z component
BKS
0
10
sec
20
30

Figure 4.16

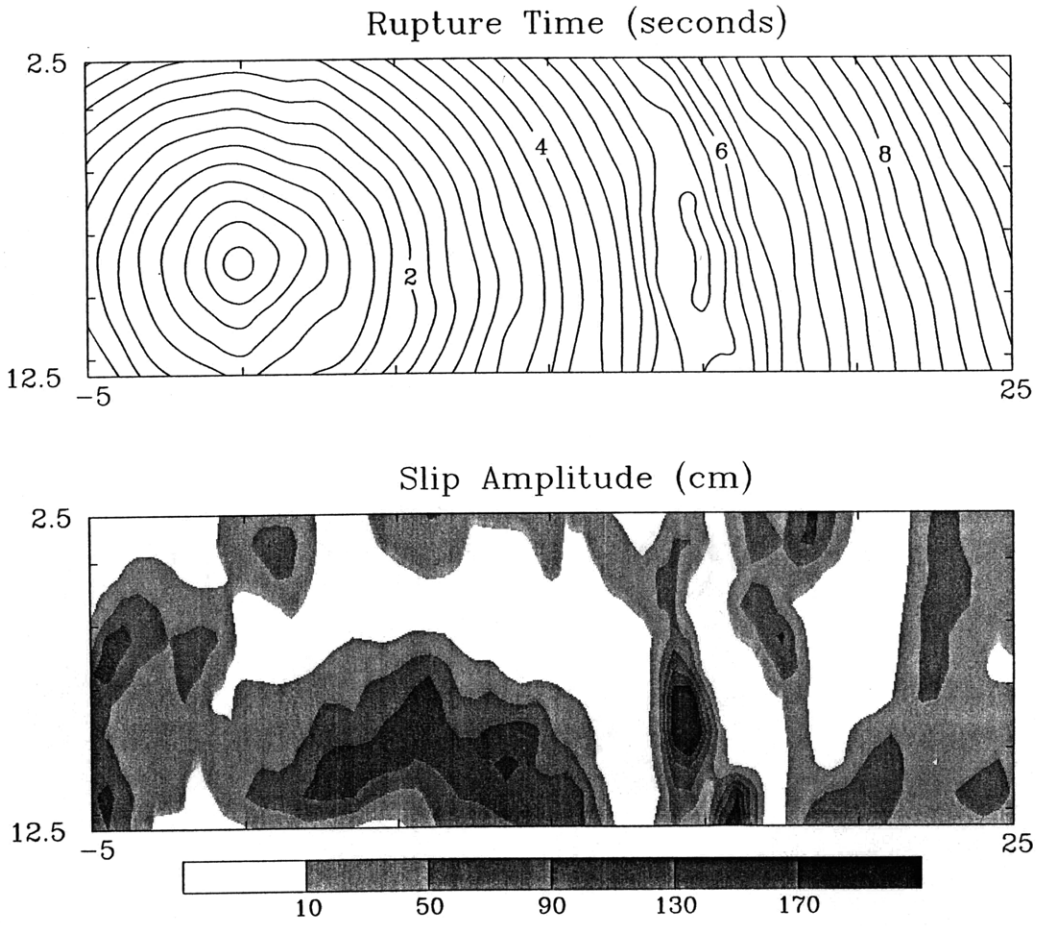
Rupture Time (seconds)
2.5
12.5
-5
25
2
4
6
8
Slip Amplitude (cm)
2.5
12.5
-5
25
10
50
90
130
170

Figure 4.17

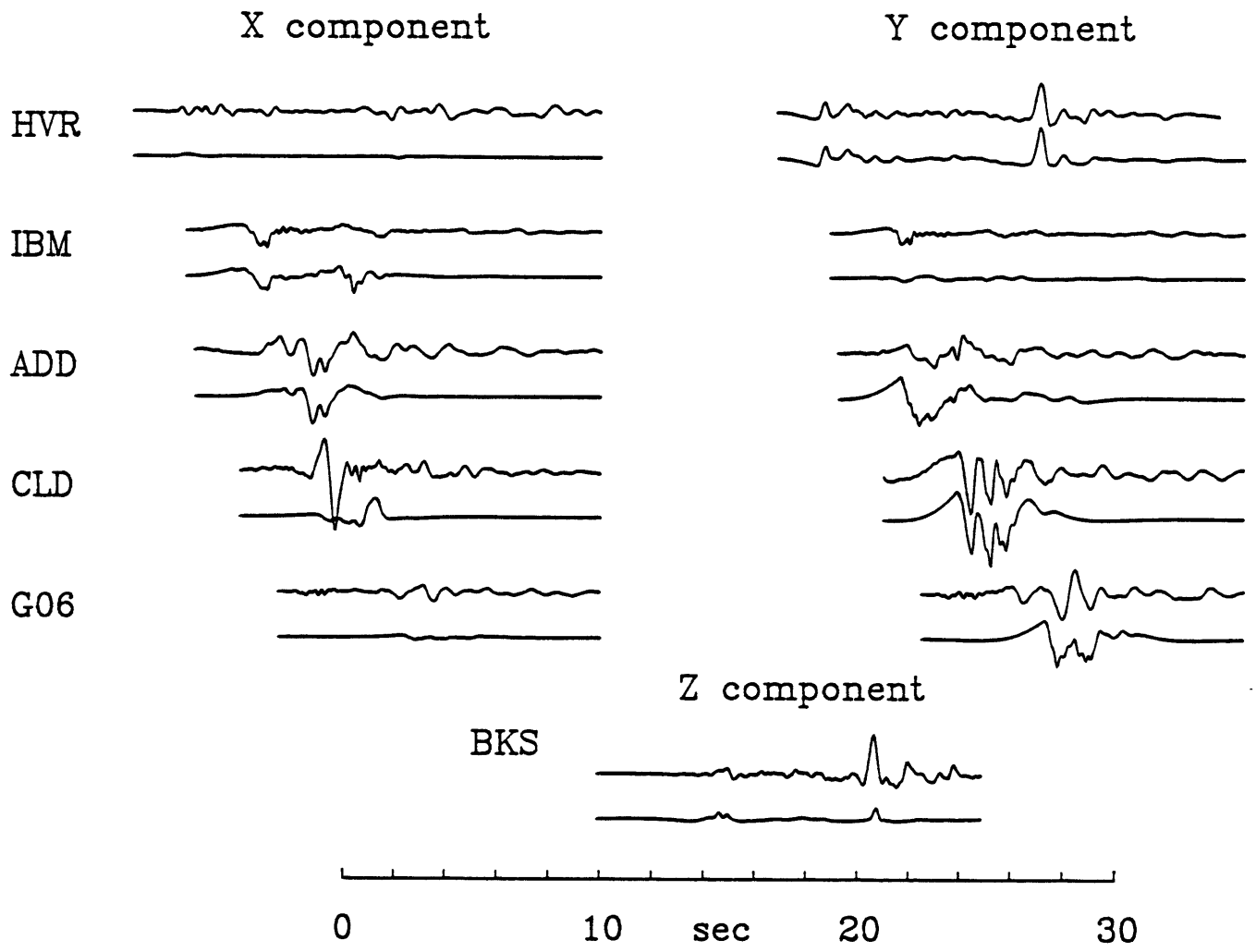
X component
Y component
HVR
IBM
ADD
CLD
G06
Z component
BKS
0
10
sec
20
30

Figure 4.18

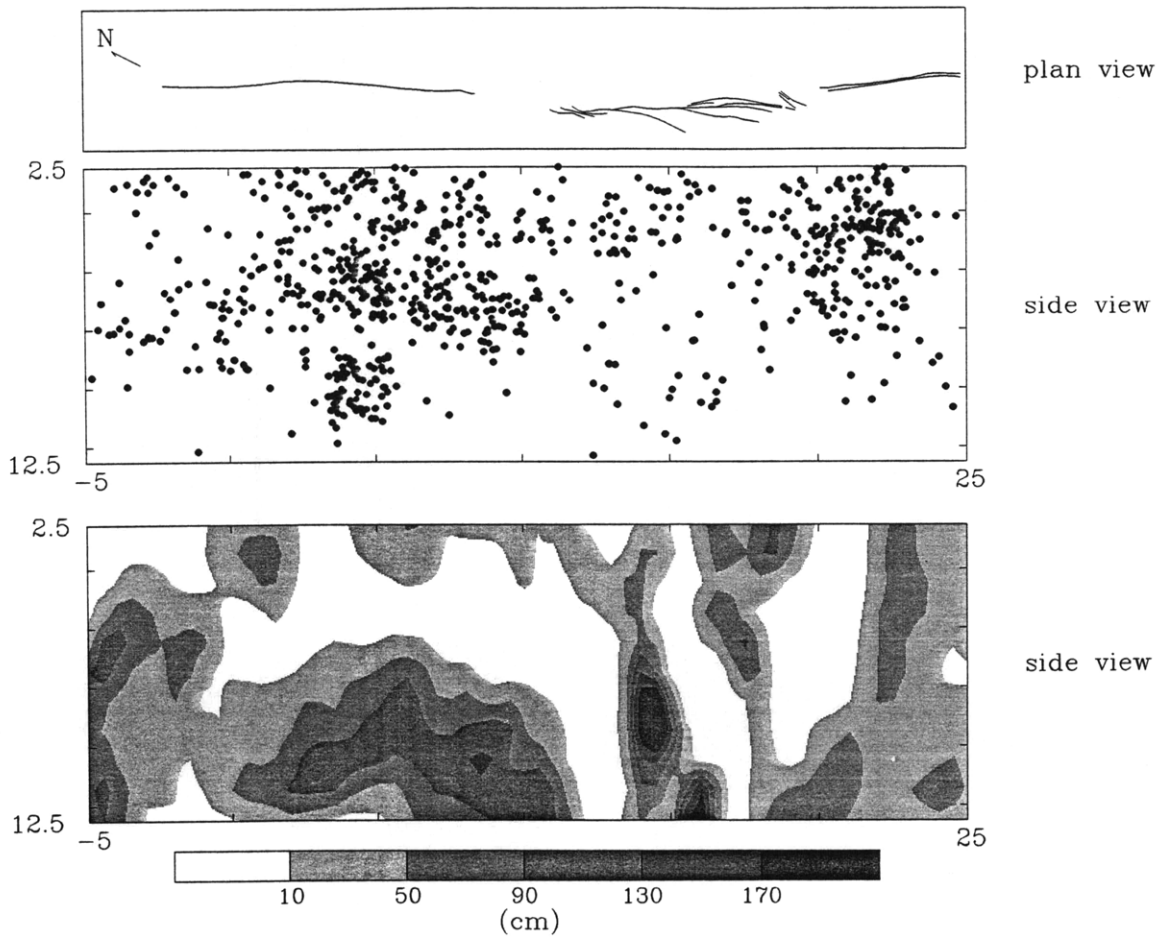
N
plan view
2.5
12.5
−5
25
side view
2.5
12.5
−5
25
side view
10
50
90
130
170
(cm)

Figure 4.19

CHAPTER 5

THE 1979 IMPERIAL VALLEY EARTHQUAKE

The 1979 Imperial Valley, California earthquake was recorded by a large number of strong-motion instruments in the immediate near-source region and has been studied in great detail. Despite careful analysis of the strong-motion data by a number of investigators there is substantial disagreement on the nature of rupture propagation during the earthquake. In this chapter we apply our technique to the strong-motion data for the Imperial Valley earthquake, derive a rupture model, and compare our results with those of previous investigators. We also attempt to explain the origin of the differences in previous interpretations of this earthquake.

Background

The Imperial Valley earthquake (M_L = 6.6) began at 2316:54.4 UTC on October 15, 1979, at (32.658°N, 115.330°W, d = 8 km) [*Archuleta*, 1982*a*] approximately 5 km south of the United States-Mexico border on the Imperial fault. Damage caused by the earthquake amounted to $21.1 million. Surface rupture extended along the Imperial fault from 10 to 35 km northwest of the hypocenter [*Sharp et al.*, 1982]. There was also surface displacement across the Brawley fault for a distance of approximately 10 km to the north of its intersection with the Imperial fault. The area of most intense aftershock activity was located at the extreme northern end of the rupture and extends into the Brawley seismic zone (Figure 5.1). A cluster of aftershocks also occurred approximately 20 km to the northwest of the hypocenter. Only a few aftershocks occurred near the hypocenter and to the south in the Cerro Prieto seismic zone suggesting that rupture propagation was primarily unilateral towards the northwest. The location of the hypocenter with respect to the surface trace of the fault [*Archuleta*, 1982*a*], basement offsets in refraction profiles [*Fuis et al.*, 1982], and the

systematic location of hypocenters to the northwest of the fault [*Johnson*, 1979] all suggest that the fault dips slightly to the northeast.

The large amount of high-quality strong-motion data and the importance of this data for earthquake engineering and seismic source studies has made the 1979 Imperial Valley earthquake one the most extensively studied earthquakes to date. Before discussing the data and our results for this event, we briefly review the rupture models of previous investigators as well as other studies that are directly relevant to our analysis of the rupture history.

Several studies of particle motion at strong-motion stations in the Imperial Valley place useful constraints on the evolution of the rupture. *Niazy* [1982] studied the horizontal components of acceleration and was able to determine that the rupture velocity over the first several seconds propagated to the north at about 2–3 km/s. *Spudich and Cranswick* [1984] used the same data set to determine the evolution of *P* and *S* wave slowness across the array during rupture and interpreted the results as being due to an average rupture velocity of 2.8 km/s with an episode of rupture propagation at nearly the *P* wave velocity over a 7-km region of the fault. *Spudich and Cranswick* [1984] found no evidence for surface waves in the frequency band 1.6–25 Hz despite the fact that there was surface rupture within 5.6 km of the differential array. The absence of dispersed arrivals was also noted by *Hartzell and Helmberger* [1982]. The lack of surface waves suggests that most of the moment release occurred below the sedimentary layers despite the fact that there was an average of 40 cm offset on the surface trace of the Imperial fault [*Sharp et al.*, 1982]. *Spudich and Cranswick* [1984] also observed that only a small portion of the fault contributed to the high-frequency radiation at any one time, consistent with the radiation of direct body waves from a compact, propagating source zone. This observation concurs with crack models of seismic rupture in which the dominant contribution to high-frequency ground motion comes from the vicinity of the crack tip.

A number of investigators have modeled the rupture history of the Imperial Valley earthquake [*Hartzell and Helmberger*, 1982; *Olson and Apsel*, 1982; *Hartzell and Heaton*,

1983; and *Archuleta*, 1984]. Substantial discrepancies remain in the amount and spatial distribution of slip on the fault as well as in the variations in rupture velocity determined in these studies. At first glance the large differences in the rupture models seem to indicate a discouraging amount of non-uniqueness inherent in the problem–even for such a well-recorded earthquake; however, the differences are not that great and can be seen to result from differing parameterizations of the rupture process.

The model of *Hartzell and Helmberger* [1982] was derived by forward modeling of displacement records at frequencies below 1 Hz. Their preferred model assumed a constant rupture velocity of 2.5 km/s (0.8β) and a constant rise time of 1 s with a triangular slip velocity function. Their model of the slip distribution included three regions of high slip from 5-10 km depth: a region of over 1.5 m of slip near the hypocenter, a region of over 2.5 m of slip 8 km to the northwest, and a region of over 2.5 m of slip 18-20 km to the northwest of the hypocenter. Slip at depths less than 4 km was everywhere less than 0.25 m.

The model of *Olson and Apsel* [1982] was the result of a stabilized, constrained inversion of low-pass filtered acceleration data in the band 0-0.33 Hz. Their study included data from Mexico, which allowed better resolution of slip near and to the south of the hypocenter. They also inverted for slip on the Brawley fault. In their inversion slip was allowed to occur several times on each subfault so that the rupture velocity effectively was allowed to vary about an assumed average value. They found that an average rupture velocity of about 0.9 times the local shear wave velocity fit the data well with a suggestion of a region of very high rupture velocity, between 4 and 5 km/s, for a 20 km segment of the Imperial fault. They also found that the rupture velocity approached the compressional wave velocity from 20 to 30 km to the northwest of the hypocenter. To fit the data at the stations in Mexico to the south of the hypocenter they found it necessary to allow a second rupture that propagated southwards beginning about 10 km to the north of the international order. The inferred slip distribution is

heterogeneous, but smoothly-varying. The peak value of slip was approximately 1.65 m and occurred at 5–10 km depth from 15–20 km to the northwest of the hypocenter.

Hartzell and Heaton [1983] studied the earthquake using near-source velocity records in the frequency band 0-1 Hz and teleseismically-recorded *P* and *SH* waves. They inverted for the slip distribution and, like *Olson and Apsel* [1982], allowed each point on the fault to rupture several times. They found that the average rupture velocity was 0.85 times the local shear wave velocity with a suggestion of some acceleration of the rupture front north of the hypocenter. They found a maximum value of slip of 1.8 m located 17 km to the northwest of the hypocenter.

Archuleta [1984] performed forward modeling of near-source velocity records to infer the slip amplitude, rupture time, and duration of faulting. In the modeling he assumed that the slip velocity function was a boxcar with variable duration. In his preferred model rupture propagated unilaterally to the northwest for a distance of 35 km. Rupture propagation began slowly at about 1.5 km/s and rapidly accelerated to 4 km/s 10 km northwest of the hypocenter. At a distance of 17 km the rupture accelerated briefly to 9.8 km/s, then decelerated to 1.9 km/s in the 22-27 km range, and accelerated again to 3.0 km/s to the northwest end of the fault. The slip-rate distribution, had three areas of concentrated slip rate: one at the hypocenter, one 20 km along strike and one 30 km along strike. Nearly all of the slip occurs below 5 km depth. The final offset has a maximum of 1.6 m at a distance of 20 km northwest of the hypocenter. The rise time varies from 0 s to 1.9 s over the fault plane.

Data

The earthquake was recorded by over 40 strong-motion instruments including film-recording, analog instruments in the United States [*Porcella et al.*, 1982; *Porter*, 1982], and digital instruments in Mexico [*Brune et al.*, 1982]. Figure 5.2 shows the horizontal components of the displacement data for a selection of stations. The horizontal components

are rotated into a coordinate system with the x axis parallel to the average strike of the fault (143°), the z axis pointing downward into the Earth, and the y axis forming a right-handed system (233°).

Vertical-component accelerograms recorded on the elements of the El Centro array are shown in Figure 5.3. The El Centro array consists of 13 stations laid out across the Imperial Valley, perpendicular to the Imperial fault. The accelerograph at E06 recorded an extremely large vertical acceleration of 1.74g [*Porcella et al.*, 1982]. Other stations in the El Centro array near the fault trace: E05, E07, E08, and EDA also recorded large vertical accelerations in excess of 0.5 m/s^2 [*Archuleta*, 1982b]. This is especially surprizing because these stations should be nearly nodal for high-frequency *P-SV* radiation from a vertical strike-slip fault. The presence of the large amplitude vertical accelerations at these stations due to direct *P* waves may indicate complex faulting that deviates from our assumption of an idealized planar fault.

Figures 5.4-5.5 show the horizontal components of displacement recorded by the El Centro array. As noted by *Hartzell and Helmberger* [1982] the y component (233°) seismograms on opposite sides of a vertical strike-slip fault are ideally symmetrical about the fault. The deviations in asymmetry can be caused by a deviation of the fault plane from the vertical; however, the effect is too large to be accounted for solely by this mechanism. *Hartzell and Helmberger* [1982] attributed this observation and the anomalous vertical motions at the El Centro array stations to corrugations in the fault plane. *Archuleta* [1982*b*] attributed the deviations from asymmetry in the x components to slip on the Brawley fault during the main rupture on the Imperial fault.

The data were uniformly sampled and instrument corrected. We band-pass filtered all the data with a two-pole zero-phase Butterworth filter run forward and backward over the data to affect a four-pole, zero-phase filter. We used low- and high-cut corner frequencies at 0.33 and 2.0 Hz. The relatively high frequency of the low-cut filter was chosen based on the

results of *Farra et al.* [1986], who found that frequencies below 0.33 Hz had substantial contributions from near-field waves for this earthquake.

As in the study of the Morgan Hill earthquake we deconvolve the slip velocity function from the data. Unlike the Morgan Hill earthquake there are no stations that allow us to constrain directly the rise time. Instead we perform the inversion with a 0.4-s rise time that is a compromise between the value found for the Morgan Hill earthquake and a value that yields the teleseismically estimated seismic moment for this event.

The data used to infer the rupture model consist of the horizontal components for 15 stations: BCR, CXO, EMO, E03, E04, E05, E08, E10, E11, EDA, HVP, and BMA in the United States, and AGR, CHI, and MCF in Mexico (Figure 5.6). Several elements of the El Centro array: E01, E02, E12, and E13 were not considered because they lie on the edge of the Imperial Valley where seismic velocities change substantially [*Fuis et al.*, 1982]. Other stations including SMC and CPO were excluded because of structural complexities [*Olson*, 1982]. The stations E06 and E07 were excluded due to the close proximity of both stations to the fault zone and the possibilities of strong path or sites effects at E06 [*Mueller et al.*, 1982; *Rial et al.*, 1986].

Seismograms were calculated using the *P*-wave model of the Imperial Valley structure of *McMechan and Mooney* [1980] based on refraction profiles and the *S*-wave model based on a study of aftershocks [*Archuleta et al.*, 1979] The assumed velocity model is shown in Figure 5.7. Lateral variations in velocity structure are less serious in the case of the Imperial Valley earthquake than in the Morgan Hill earthquake. The trigger times of instruments without absolute time are adjusted so that the initial *S* wave from the hypocenter arrives at the time predicted by the assumed velocity structure. The actual and assumed trigger times for the stations used in our analysis, expressed in seconds after the origin time (2316:54.4 UTC), are listed in Table 5.1.

Because we our method for calculating seismograms incorporates only direct *P* and *S* waves we have excluded data for which *SS* is a prominent phase. This has the effect of

limiting the time windows in stations in the El Centro array and decreases our resolution of faulting on the northernmost segment of the fault. The Imperial Valley structure shown in Figure 5.7 also has a triplication associated with the steep rise in velocity at 12 km depth. By comparing complete theoretical seismograms [*Archuleta*, 1984] with our asymptotic seismograms it was found that retaining only the direct arrival was a reasonably good approximation.

The rupture zone considered in our analysis extends from 35 km to the northwest to 10 km to the southeast of the hypocenter (Figure 5.7). The location of the fault is assumed to follow the surface trace at an azimuth of 323° and a dip of 80° to the northeast [*Archuleta*, 1984]. In our starting models, rupture is assumed to initiate at the instrumental hypocenter (2316:54.4 UTC, 32.658°N, 115.330°W, d = 8 km) [*Archuleta*, 1982*a*] and to propagate outward at a fixed fraction of the shear wave velocity over the assumed fault zone.

Sensitivity Tests

To determine the extent to which we can resolve different aspects of the rupture history of the 1979 Imperial Valley earthquake, we have performed sensitivity tests on synthetic data with a realistic amount of correlated noise. The station set and weights are the same as those used in the eventual modeling of the strong-motion data.

As a test case we have adopted a model derived from that of *Archuleta* [1984], described above, for the Imperial Fault (Figure 5.8). This model is particularly good for the sensitivity tests because it includes several features that we would like to be able to resolve. The slip rate is highly variable over the fault plane. In the model there are three areas of concentrated slip: one at the hypocenter, one 20 km along-strike near EMO, and one 30 km along strike beyond the El Centro array. There is no slip to the south of the hypocenter. The rupture time behavior is also strongly heterogeneous. Rupture velocity is quite slow near the hypocenter, accelerates for 10 km, briefly decelerates, and from 17-22 km exceeds the P wave velocity,

before decelerating and eventually stopping. By using the extensive data set available for this earthquake, we hope to be able to resolve these kinds of features using our technique.

Theoretical seismograms were calculated for the true model with noise added as in the sensitivity tests for the Morgan Hill earthquake described in Chapter 4. The stations used in the analysis are listed in Table 5.1.

For the sensitivity test we assume a starting model in which the rupture velocity is a constant fraction of the shear wave velocity, the slip is only 10 cm at depths less than 5 km, and the slip is 40 cm at depths greater than 5 km (Figure 5.9). The rupture velocity is a constant 0.8 times the local shear wave velocity, which is substantially slower than the average rupture velocity of the true model, 0.95β. The initial slip distribution is everywhere smoothly varying.

We first attempt a linear inversion for slip over the fault with the constant rupture velocity model. The results of this inversion are shown in Figure 5.10. The model correctly recovers the lack of slip to the south of the hypocenter; however, near the hypocenter itself, the slip amplitude is too low. This was a region of relatively high slip in the original model. The only slip near the hypocenter in the model is recovered at the correct depth, but is several km to the south. The reason that so little slip is resolved near the hypocenter is that the rupture velocity in the true model is quite low and the slip, although large, occurs while rupture is growing slowly and hence occurs where the isochrone velocity is lower than for the starting model. In this situation the data can be fit with a smaller slip amplitude than would otherwise be possible.

A region of very high slip is also resolved 15-20 km along the strike of the fault. In this case the fit to the data is obtained by making the slip larger than it is in the original model (Figure 5.8). The large area that the slip covers in the estimated model is caused by the discrepancies in arrival time when the rupture time does not match that in the original model. The region of high slip at 30 km is resolved, but is of lower amplitude. Only the station

BMA lies to the north of this section of the fault, resulting in poor resolution of the rupture model there.

If we allow the slip to vary as well as the rupture time, the results improve markedly. Figures 5.11-5.12 show the results for the linearized inversion for slip and rupture time. As before the slip to the southeast of the hypocenter is correctly determined to be negligible. Slip near the hypocenter is somewhat larger and correctly located to the north of the hypocenter, although it is still less than in the original model. The region of high slip 20 km along-strike is recovered in the inversion at the correct depth and location. This feature is recovered with much more fidelity and underscores the necessity of making rupture time a free parameter in modeling earthquake rupture. The depth extent of the region of high slip is fairly well resolved over the length of the fault. As in the previous test case, the high-slip region at 30 km is not well resolved.

The results of the inversion for the rupture time are also encouraging (Figure 5.12). The region of high rupture velocity from 17-22 km in the true model is recovered in the estimated model. Rupture time is perturbed in this region sufficiently to compensate for the slower average rupture velocity overall and the region of high rupture velocity is recovered in the correct location. In regions where there is little slip amplitude or in regions beyond most of the stations 25-35 km along-strike, the rupture time is not well recovered. However, the primary failing in the rupture time calculation is that the very slow rupture velocities in the vicinity of the hypocenter are not recovered. This is due to several factors. The hypocentral region is fairly small compared the other regions of heterogeneity that were successfully recovered. In addition, the inversion algorithm satisfied the noisy data adequately by decreasing the slip amplitude rather than the rupture velocity. Because the rupture time was not properly recovered, the estimate of the slip near the hypocenter was far too low. Had there been more data from the southern part of the rupture zone, better resolution of the hypocentral behavior would have been possible.

Constant Rupture Velocity Model for the Imperial Valley Earthquake

We are now in a position to apply the technique to the data for the 1979 Imperial Valley earthquake. We use the horizontal components for the 15 stations listed in Table 5.1. The data weighting was adjusted so that stations in the heavily-instrumented northern end of the rupture zone did not dominate the solution. Stations in the El Centro array were assigned a weight of 1. Stations to the south in Mexico and those that were off the fault in the United States were given weights of 3. The station at EMO was given a weight of 0.5 due to its close proximity to the fault. This is the same weighting scheme as was applied to the data for the synthetic test cases of the previous section.

For the first rupture model we constrain the rupture velocity at 0.85β, and invert only for the slip intensity. The results we obtain are similar to those of *Hartzell and Helmberger* [1982] in their forward modeling of the earthquake assuming a rutpure velocity of 0.8β. Our rupture model is shown in Figure 5.13 and the fit to the deconvolved data is shown in Figure 5.14. The most prominent feature is a region of high slip from 17-25 km along-strike from the hypocenter. This feature was also found by *Hartzell and Helmberger* [1982]. Between the region of high slip and the hypocenter there is very little slip. Since we are using a high-frequency approximation and because the data are band-pass filtered, we may not be able to recover some of the slowly-varying slip on the fault. On the other hand, the almost complete lack of slip over much of the fault plane suggests that this may be a consequence of holding the rupture time fixed.

The seismic moment for this rupture model is 1.1×10^{18} Nm. The teleseismically estimated seismic moment is 7.0×10^{18} Nm [*Kanamori and Regan*, 1982]. The difference between the two values suggests that the amount of slip inferred from the strong-motion data is far too low.

Variable Rupture Velocity Model for the Imperial Valley Earthquake

In the next model we allow both the rupture time and the slip intensity to vary. The starting model has an average rupture velocity of 0.85β. The rupture model is shown in Figure 5.15 and the fit to the deconvolved data is shown in Figure 5.16. For the variable rupture velocity model, the slip distribution looks very different (Figure 5.15) than in the previous model (Figure 5.13). In particular there is a region of high slip located from 15-20 km along-strike. This feature is similar to features found in other models of this earthquake [*Olson and Apsel*, 1982; *Hartzell and Heaton*, 1983; *Archuleta*, 1984] although it is somewhat shallower in our model. As mentioned previously the depth resolution is not particularly good compared with the resolution of the location along-strike. The fit to the data would not be seriously degraded by moving the high-slip region somewhat deeper. In the region of high slip there is also a high rupture velocity–between the 7 and 8 second rupture time contours. This is similar to the high rupture velocities found by *Archuleta* [1984] in approximately the same location, although our rupture velocities are somewhat lower. The rupture velocity in our model is in excess of the shear wave velocity in this region for a distance of about 5 km from 19-24 km from the hypocenter.

It is interesting that this anomalous region is near the intersection of the Imperial and Brawley faults, which is located at 22 km along-strike. It may be that the Brawley fault provided a geometric obstruction that caused the Imperial fault to accumulate more strain locally during the interseismic period and that during the eventual rupture this increased strain was suddenly released; however, the mechanism by which this might occur is not as obvious as in the case of the left-step on the Calaveras fault near Anderson Reservoir in the Morgan Hill earthquake.

Our rupture model also has several features between the high-slip region and the hypocenter. The regions of 40-60 cm of slip are associated with areas of locally slow rupture propagation. This combination is required to fit several pulses recorded on the data recorded in Mexico, which are of large amplitude and short duration and are particularly evident at the

stations CHI and AGR. A more extensive region of backward rupture propagation was included by *Olson and Apsel* [1982] in their model of this earthquake. We did not resolve any backward propagation of rupture; however, if such a region is large, then it may be impossible to recover in our linearized approximation.

This region of the fault 10 km to the northwest of the hypocenter may have behaved like the region of the Calaveras fault near Anderson Reservior in the Morgan Hill earthquake. In this case however, there is no obvious explanation of the behavior in terms of fault geometry since the fault plane in this area is geometrically quite simple. The occurrence of a small cluster of aftershocks approximately 10 km to the north of the hypocenter (Figure 5.1) may be associated with this region of higher slip.

Slip to the south of the hypocenter is relatively low in amplitude. This is in contrast to the results of *Olson and Apsel* [1982] who found significant slip in this region. We did not model as much of the Mexican data as they did since some of it did not satisfy our assumption of the high-frequency, near-source approximation. It may be that this data indicates more slip to the south of the hypocenter than the data we analyzed.

Unlike other models of this earthquake, we did not resolve much slip beyond a distance of 25 km to the northwest of the hypocenter. This is a consequence of excluding the SS phase from our time windows. The SS phase from the hypocenter and the fault to the northwest of the hypocenter will interfere with the direct S waves from the northwestern part of the fault for most stations. Only the station BMA records a clean S wave. The result is poor resolution as indicated by the sensitivity tests.

Although our rupture model assumed a lower rupture velocity 0.85β than the studies of *Olson and Apsel* [1982] and *Archuleta* [1984], we resolve similar features of high slip and high rupture velocity. This may be the result of differing slip velocity functions in their studies, which had a decaying exponential [*Olson and Apsel*, 1982] and a box-car [*Archuleta*, 1984] time-dependence. Adopting the higher average rupture velocities found in

those studies of 0.9β by *Olson and Apsel* [1982] and 0.95β by *Archuleta* [1984] we were unable to fit the data as well.

The seismic moment for this rupture model is 2.3×10^{18} Nm, which is substantially less than the teleseismically estimated seismic moment of 7.0×10^{18} Nm [*Kanamori and Regan*, 1982]. The difference between the two values suggests that the amount of slip inferred from the strong-motion data is too low. This could be due to several factors. Slip on the northwest segment of the fault was not well resolved. In addition, the results we obtain using the band-passed data lack the low-wavenumber components of the slip distribution, which can contribute much of the seismic moment.

TABLE 5.1 Trigger Times

Station	Time
E03	6.18
E04	6.80
E05	6.75
E08	6.90
E10	6.80
E11	6.08
EDA	6.70
EMO	4.40
BMA	9.11
HVP	4.05
CXO	4.47
BCR	2.71
MCF	3.78
AGR	1.69
CHI	4.17

Figure Captions

Figure 5.1 Aftershocks of the Imperial Valley earthquake are shown with the surface traces of regional faults [*Jennings*, 1975]. The location of the hypocenter of the 1979 earthquake is indicated with an asterisk, just south of the international border (horizontal line). The intense aftershock activity at the northern end of the fault zone is associated with the Brawley seismic zone. A cluster of aftershocks occurred about 10 km to the north of the border. Rupture propagation was apparently primarily unilateral to the northwest. Surface faulting began north of the U.S.-Mexico border and extended for 30 km.

Figure 5.2 Horizontal components of displacement are shown for a selection of stations distributed from south to north along the strike of the Imperial Fault. The horizontal offset of the traces is proportional to the time offset.

Figure 5.3 The vertical component of acceleration is shown for the elements of the El Centro array. For an ideal vertical strike-slip fault, the vertical component should be nodal along the fault plane.

Figure 5.4 The horizontal y component of displacement across the El Centro array is shown. For an ideal vertical strike-slip fault in a laterally homogeneous medium the y component of motion ought to be symmetric about the fault.

Figure 5.5 The horizontal x component of displacement across the El Centro array is shown. For an ideal strike-slip fault in a laterally homogeneous medium the x component ought to be antisymmetric about the fault.

Figure 5.6 The stations used in the inversions are shown by triangles with their three-letter codes. The surface trace of faults in the Imperial Valley after *Jennings* [1976] are shown with solid and dotted curves. The epicenter of the Imperial Valley earthquake is shown with an asterisk. The approximation we make to the fault plane is indicated with the straight line running from 10 km to the southeast of the epicenter to 35 km to the northwest. The displacement of the epicenter to the east of the fault plane is due to the dip of the fault.

Figure 5.7 The *P*-wave velocity model determined by *McMechan and Mooney* [1980] and the *S*-wave velocity model determined by *Archuleta et al.* [1979] are shown with dashed lines. The values used in this study are shown with solid lines.

Figure 5.8 A synthetic test case to assess the resolution of the rupture history. The model is simply that of *Archuleta* [1984] for the Imperial Fault with the same rupture time distribution and the slip intensity assumed equal to the slip rate.

Figure 5.9 The starting model for the sensitivity tests and for our modeling of the actual data. Rupture begins at the instrumentally determined hypocenter and propagates at a constant fraction of the shear wave velocity. In this case the rupture velocity is 0.8 times the shear wave velocity. Slip is smoothly varying over the fault. Slip above 5 km depth is 10 cm and at 5 km depth and below is 40 cm.

Figure 5.10 The results of an inversion for slip only with rupture time held fixed. Slip to the southeast of the hypocenter is correctly estimated to be negligible. Slip near the hypocenter is negligible as well, but should be of substantial amplitude as in the original model (Figure 5.9). The region of high slip 20 km along strike is recovered, but is poorly resolved. The region of high slip 30 km along-strike is not well resolved. All but one of the stations used lies to the southeast of this part of the fault.

Figure 5.11 A comparison of the slip distribution for results of an inversion in which both slip and rupture time are allowed (below) to vary with the slip distribution in the original model (above). The slip amplitude bears much closer resemblance to the original model than when the rupture time was not a free parameter. The slip distribution to the northwest of the hypocenter is better resolved in depth and extent. The region of high slip at 20 km is also much better resolved. The region at 30 km is still not well resolved. Slip near the hypocenter is more similar to the original model than in the previous test case, but is still too small.

Figure 5.12 A comparison of the original and recovered rupture time model. Although the assumed rupture velocity in the starting model is substantially lower than in the original model, the region of high rupture velocity is correctly recovered at a distance of 17-22 km along-strike. A smaller region of high rupture velocity at 6-12 km along-strike is also recovered; however, the amplitude of the perturbation is small.

Figure 5.13 The results of an inversion assuming a constant rupture velocity of 0.85β and a rise time of 0.4 s is shown for the data from the Imperial Valley earthquake.

Figure 5.14 The fit to the data for the rupture model in Figure 5.13.

Figure 5.15 The results of an inversion assuming a constant rupture velocity of 0.85β and a rise time of 0.4 s is shown for the data from the Imperial Valley earthquake.

Figure 5.16 The fit to the data for the rupture model in 5.15.

Figure 5.17 A map view of the seismicity 1973-1979 in the Imperial Valley is shown together with the surface traces of faults in the region. The most intense activity occurs to the north of the 1979 earthquake rupture zone in the Brawley seismic zone and to the south in the Cerro Prieto seismic zone. There are very few events in areas which are inferred to have undergone large amounts of slip during the earthquake. The distribution of the pre-earthquake seismicity is similar to that of the aftershocks (Figure 5.1).

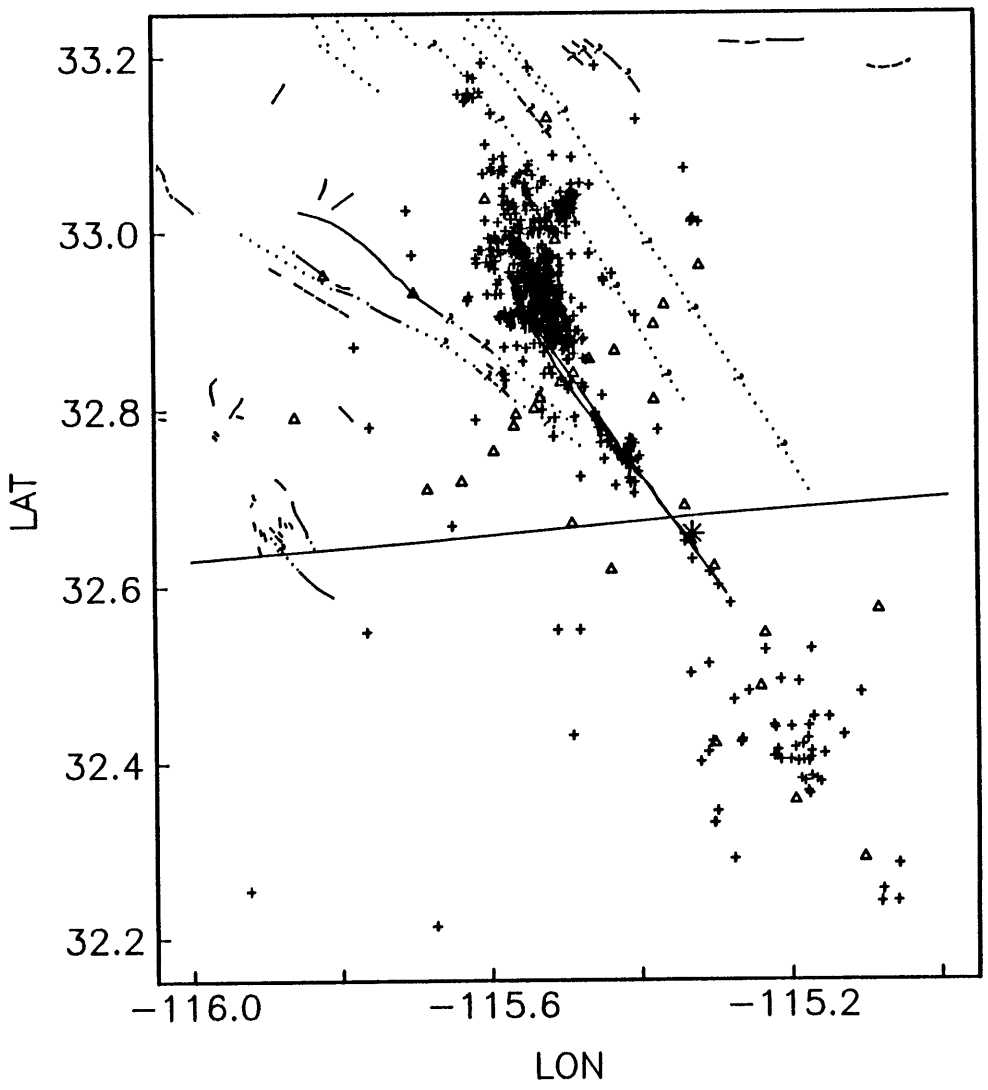

Figure 5.1

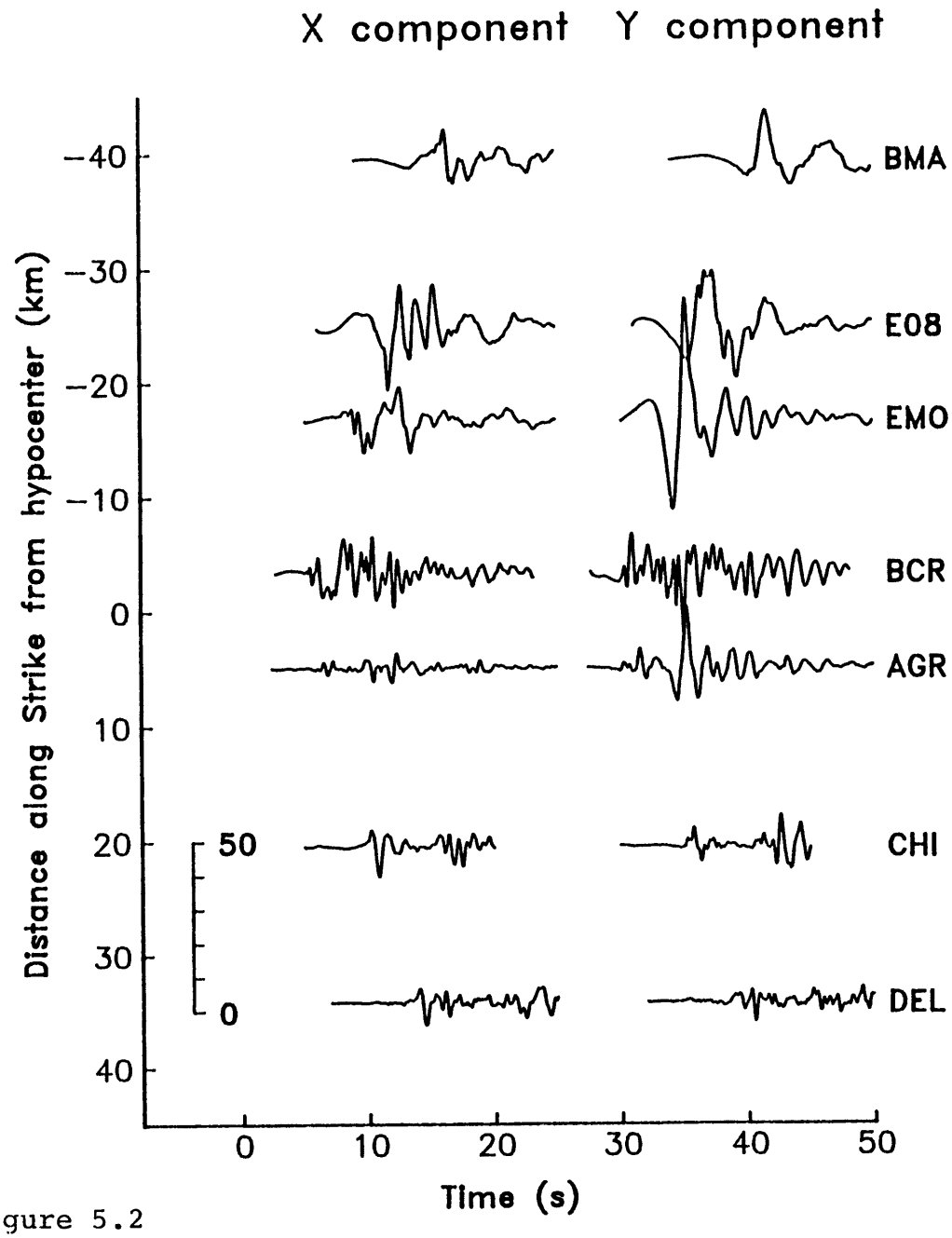
X component
Y component
BMA
E08
EMO
BCR
AGR
CHI
DEL
50
0
Distance along Strike from hypocenter (km)
-40
-30
-20
-10
0
10
20
30
40
0
10
20
30
40
50
Time (s)

Figure 5.2

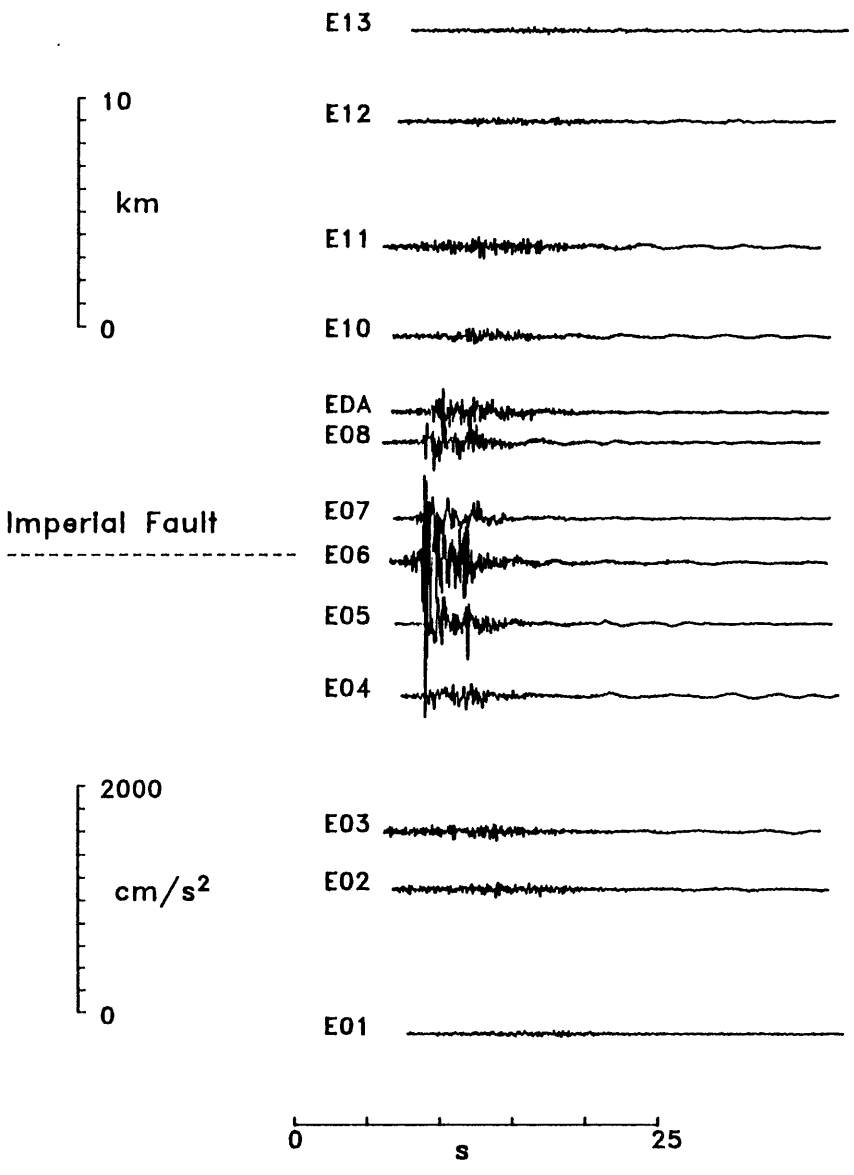
Z component
E13
10
E12
km
E11
0
E10
EDA
E08
Imperial Fault
E07
E06
E05
E04
2000
E03
cm/s²
E02
0
E01
0
s
25

Figure 5.3

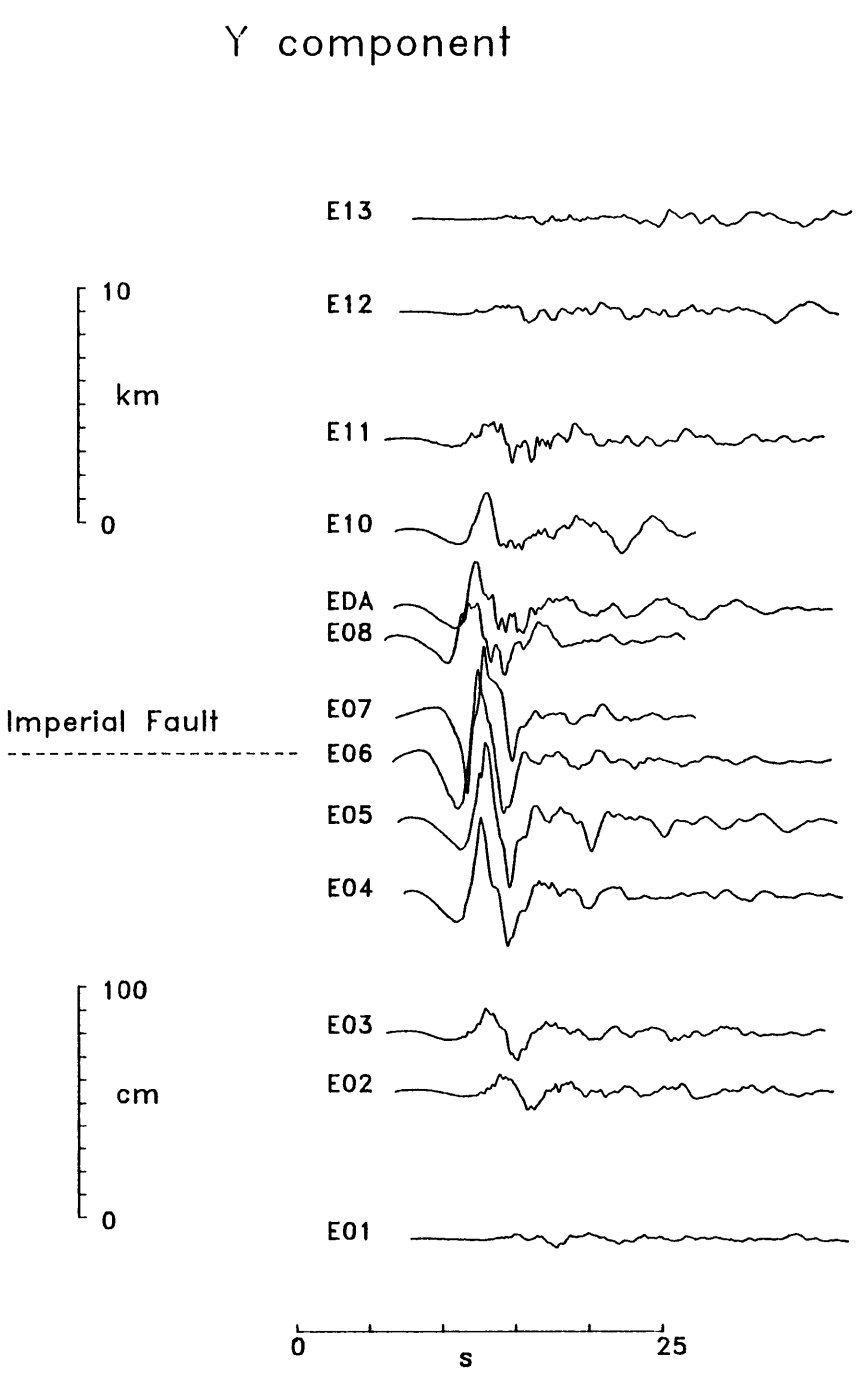
Y component
E13
E12
E11
E10
EDA
E08
E07
E06
E05
E04
E03
E02
E01
10
km
0
100
cm
0
Imperial Fault
0
s
25

Figure 5.4

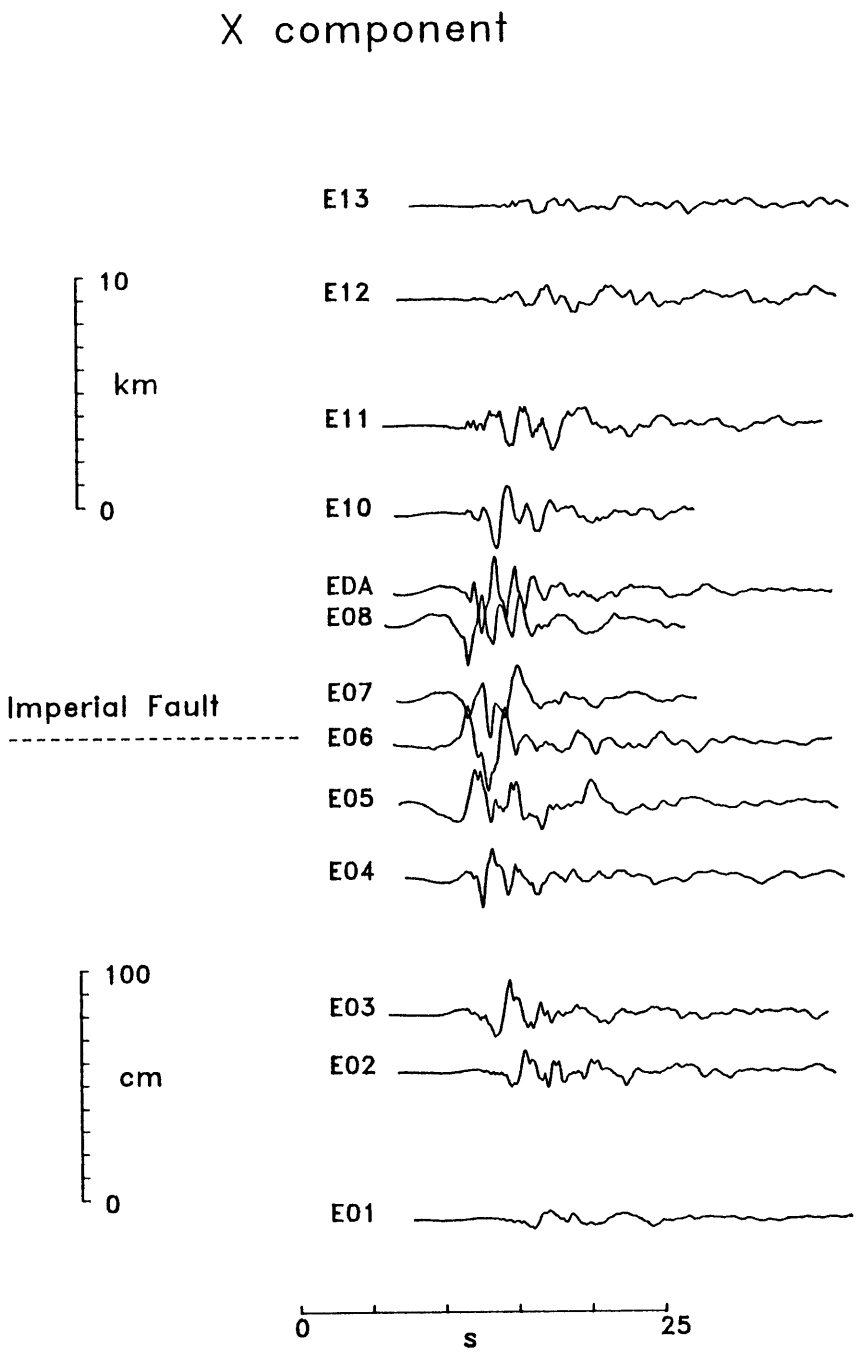
X component
E13
E12
10
km
E11
0
E10
EDA
E08
Imperial Fault
E07
E06
E05
E04
100
cm
E03
E02
0
E01
0
s
25

Figure 5.5

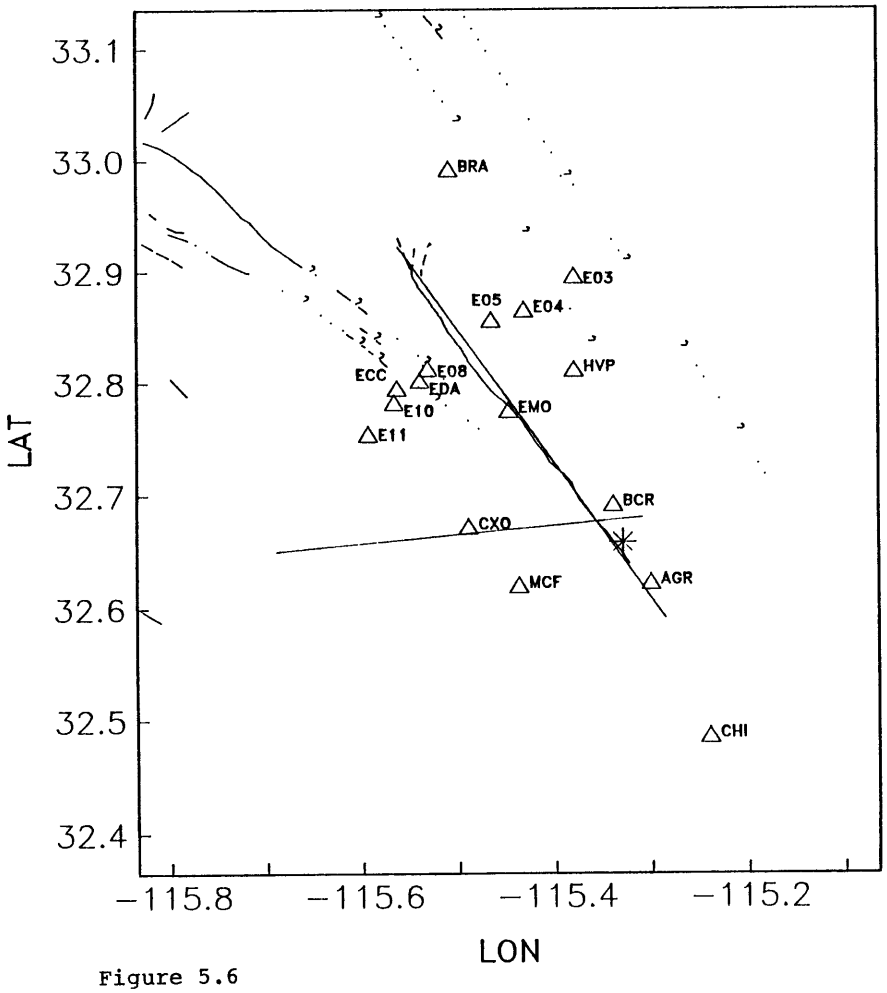
33.1
33.0
32.9
32.8
32.7
32.6
32.5
32.4
LAT
−115.8
−115.6
−115.4
−115.2
LON
BRA
E03
E05
E04
HVP
ECC
E08
EDA
E10
EMO
E11
BCR
CXO
MCF
AGR
CHI

Figure 5.6

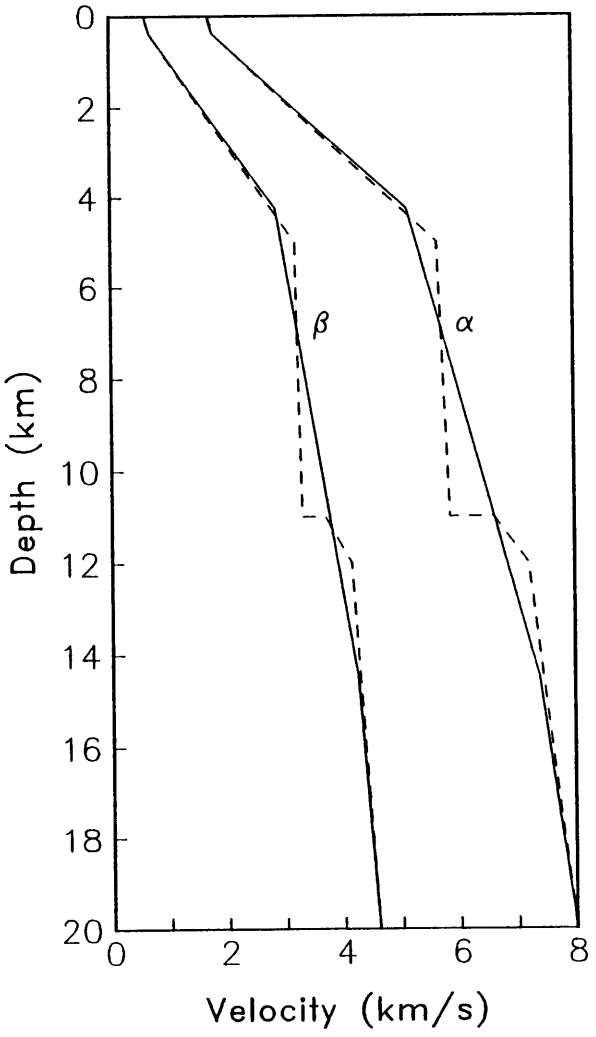

Figure 5.7

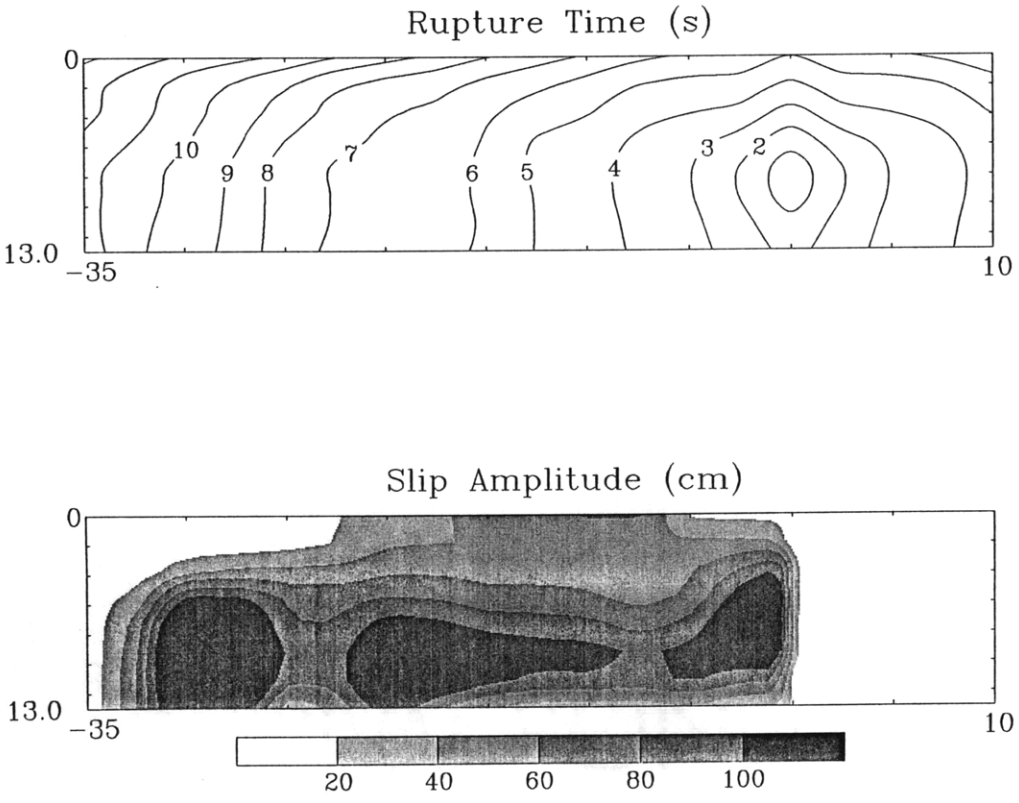
Rupture Time (s)
0
10
9
8
7
6
5
4
3
2
13.0
−35
10
Slip Amplitude (cm)
0
13.0
−35
10
20
40
60
80
100

Figure 5.8

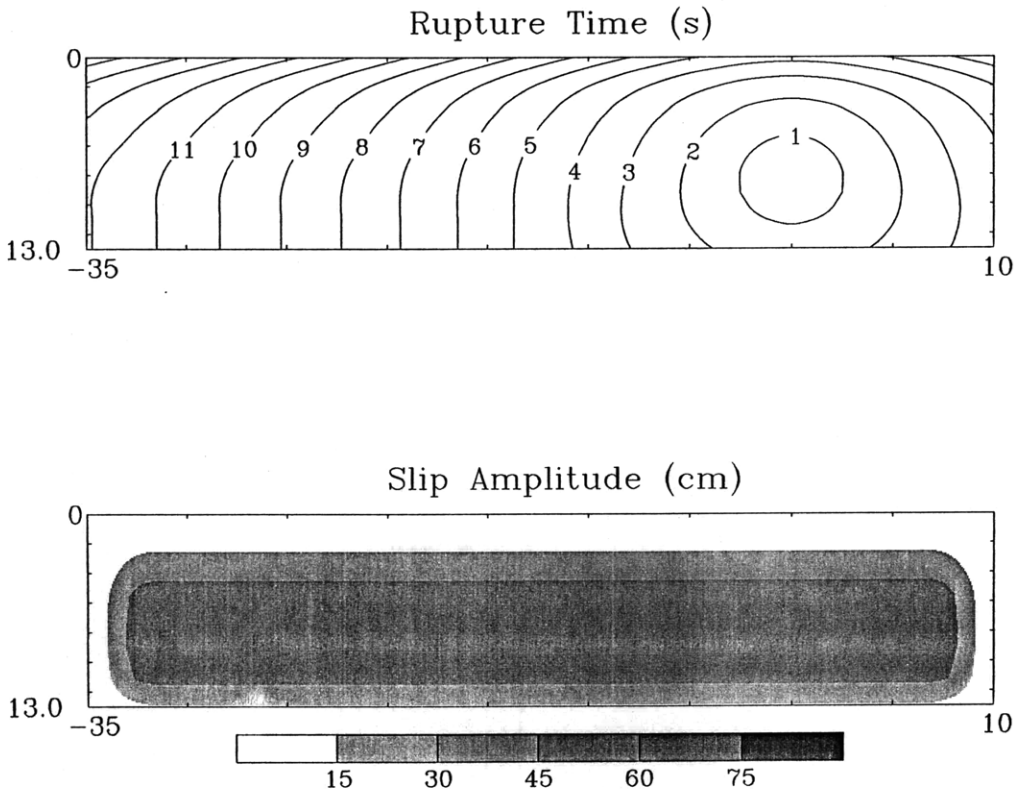
Rupture Time (s)
0
11
10
9
8
7
6
5
4
3
2
1
13.0
−35
10
Slip Amplitude (cm)
0
13.0
−35
10
15
30
45
60
75

Figure 5.9

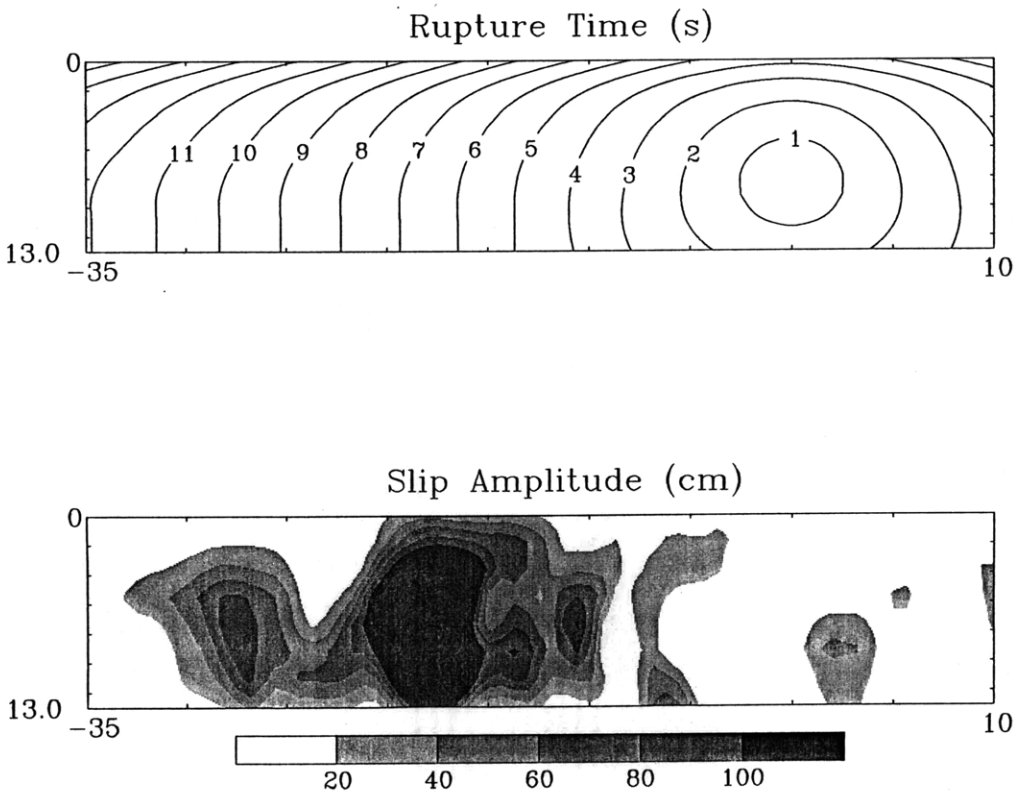
Rupture Time (s)
0
11
10
9
8
7
6
5
4
3
2
1
13.0
−35
10
Slip Amplitude (cm)
0
13.0
−35
10
20
40
60
80
100

Figure 5.10

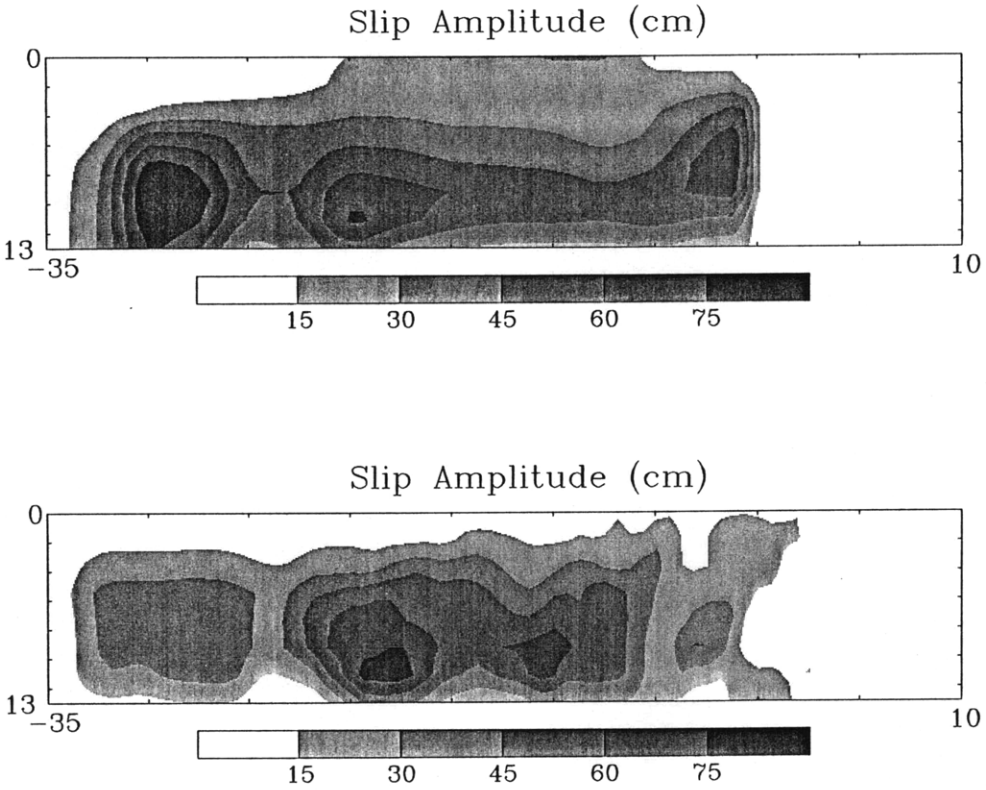
Slip Amplitude (cm)
0
13
−35
10
15
30
45
60
75
Slip Amplitude (cm)
0
13
−35
10
15
30
45
60
75

Figure 5.11

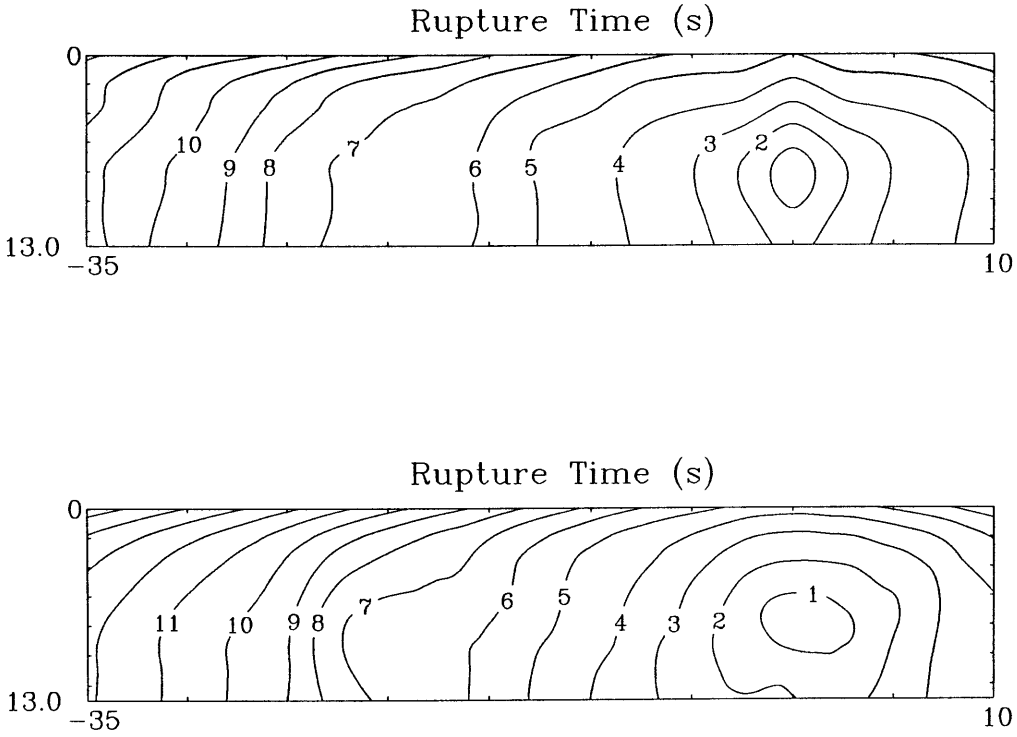
Rupture Time (s)
0
13.0
−35
10
10
9
8
7
6
5
4
3
2
Rupture Time (s)
0
13.0
−35
10
11
10
9
8
7
6
5
4
3
2
1

Figure 5.12

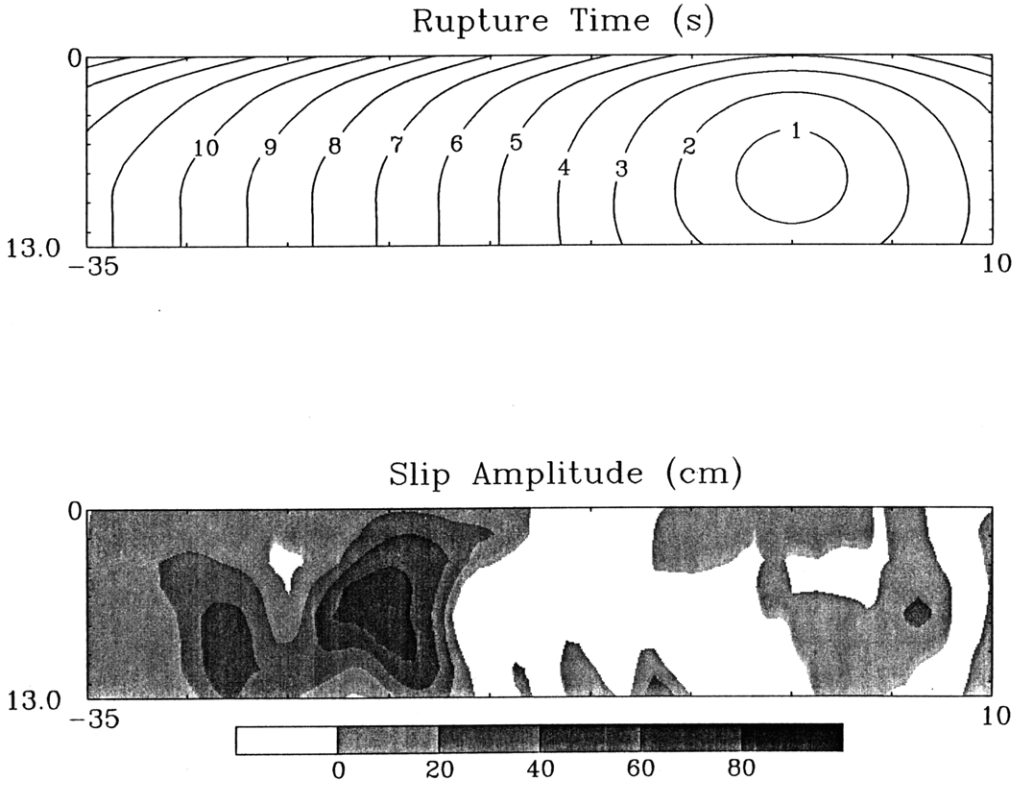
Rupture Time (s)
0
10
9
8
7
6
5
4
3
2
1
13.0
−35
10
Slip Amplitude (cm)
0
13.0
−35
10
0
20
40
60
80

Figure 5.13

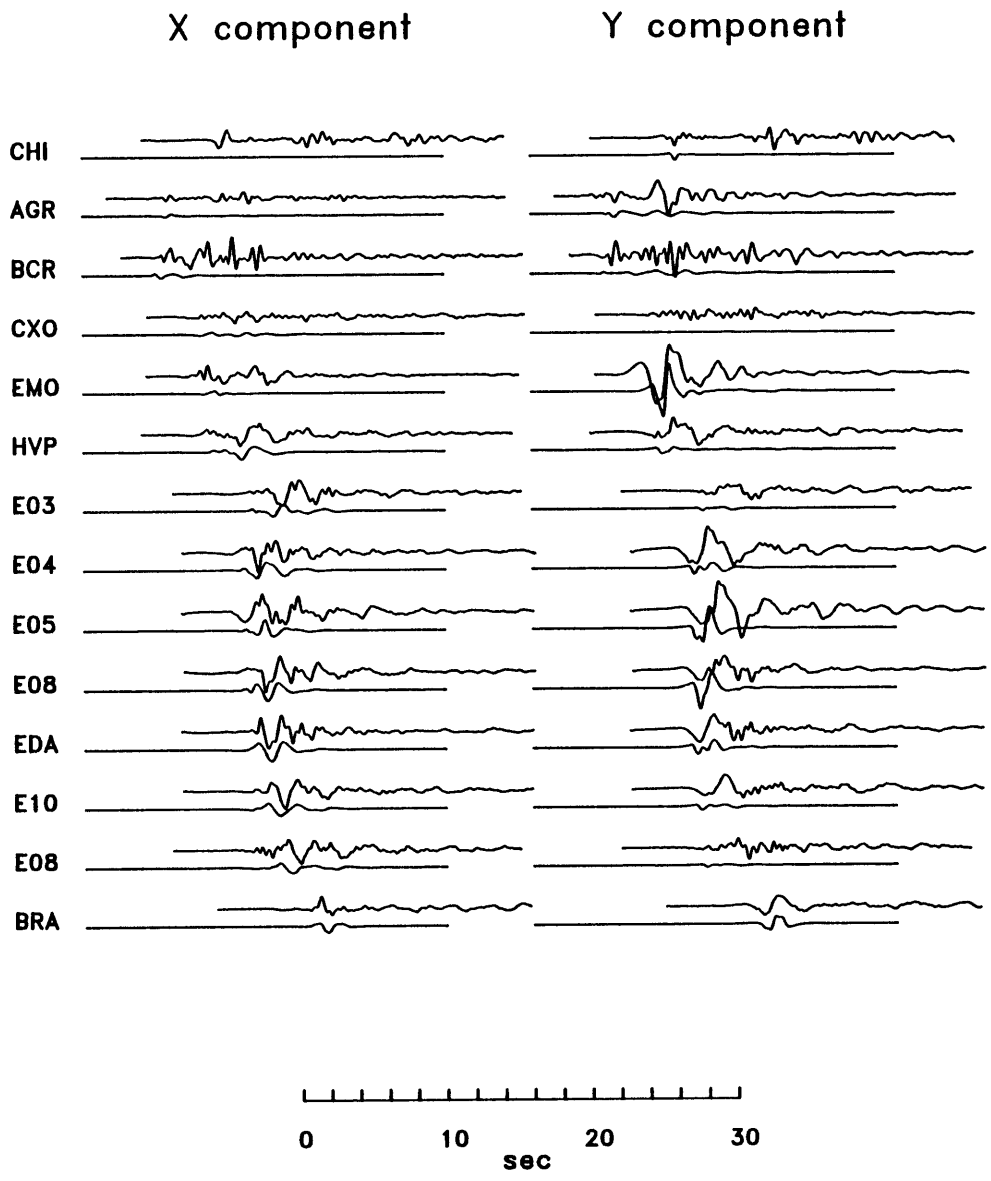
X component
Y component
CHI
AGR
BCR
CXO
EMO
HVP
E03
E04
E05
E08
EDA
E10
E08
BRA
0
10
20
30
sec

Figure 5.14

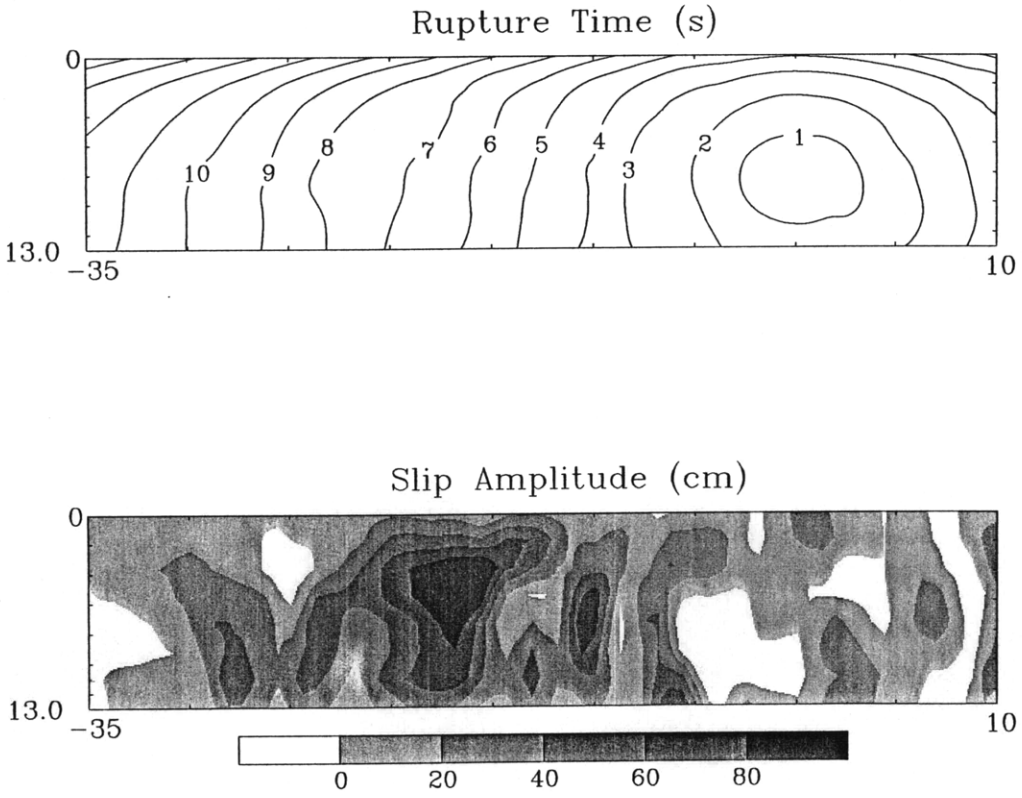
Rupture Time (s)
0
13.0
−35
10
10
9
8
7
6
5
4
3
2
1
Slip Amplitude (cm)
0
13.0
−35
10
0
20
40
60
80

Figure 5.15

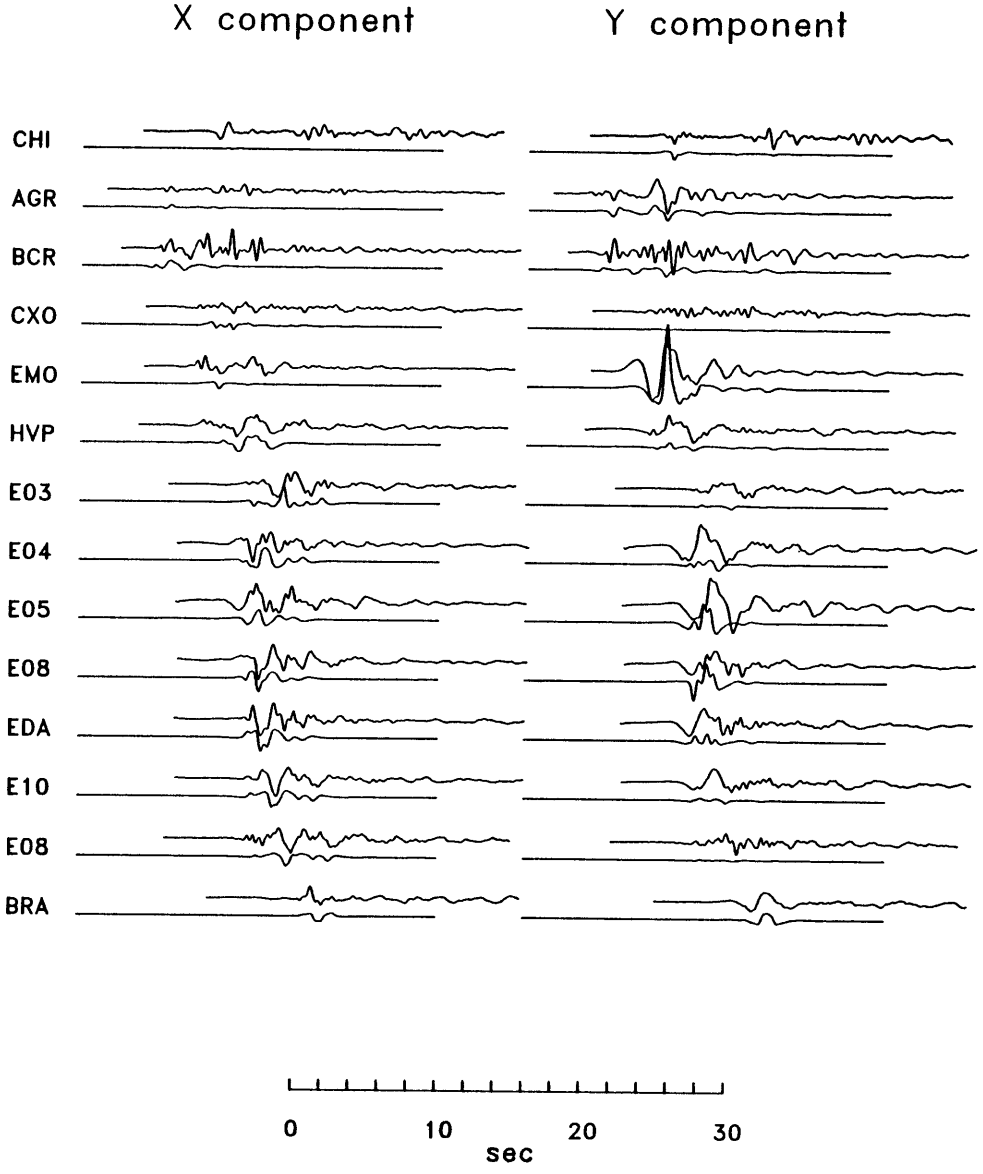
X component
Y component
CHI
AGR
BCR
CXO
EMO
HVP
E03
E04
E05
E08
EDA
E10
E08
BRA
0
10
20
30
sec

Figure 5.16

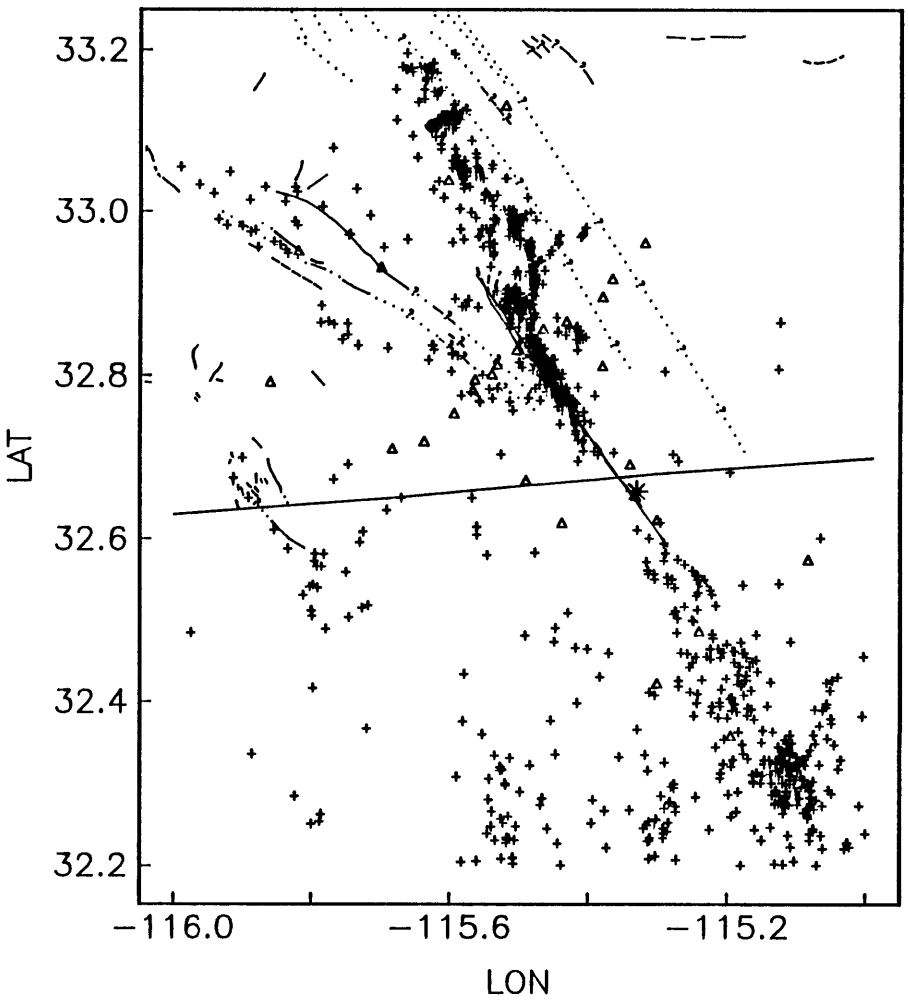

Figure 5.17

CHAPTER 6

THE 1966 PARKFIELD EARTHQUAKE

In this chapter we attempt a simple analysis of the Parkfield earthquake to determine the extent of coseismic rupture. Because of the poor station distribution we do not consider models in which rupture time is a free parameter. Our results do not provide a definitive rupture history for most of the fault, but they do allow us to place constraints on the extent of seismic rupture for a reasonable range of rupture velocities and to resolve an area of high slip rate on the fault.

Background

The Parkfield earthquake (M_L = 5.5) began at 0426:13.4 UTC on June 28, 1966, at (35.955N°, 121.498°W) [*McEvilly et al.*, 1967] on the San Andreas fault in central California. Like the 1934 Parkfield earthquake that ruptured the same segment of the San Andreas fault, the 1966 earthquake was preceded by a large foreshock 17 minutes before and immediately to the northwest of the mainshock [*McEvilly et al.*, 1967]. The aftershocks of the 1966 earthquake initially extended for 20 km to the southeast of the epicenter along the San Andreas fault and eventually extended to 27 km to the southeast [*McEvilly et al.*, 1967]. Surface cracking extended to 33 km to the southeast of the epicenter [*Smith and Wyss*, 1968].

The 1966 Parkfield earthquake occurred shortly after the installation in late 1965 of an array of strong-motion instruments near Cholame, California across the San Andreas fault, 20 km to the southwest of Parkfield. The strong-motion data for the 1966 earthquake included high-quality analog records from 5 accelerographs located near the southern terminus of rupture.

Because they represented one of the most complete strong-motion data sets prior to the 1971 San Fernando earthquake, the Parkfield data were studied by many investigators. The transverse component of motion at C02 was the first near-source seismogram to be successfully modeled. Since that time, the sophistication of strong-motion seismology has increased substantially and the importance of understanding seismic rupture on this particular segment of the San Andreas fault has increased due to the forecast of a future earthquake at Parkfield [*Bakun and McEvilly*, 1984; *Bakun and Lindh*, 1985], and the possibility that the great 1857 Fort Tejon earthquake on the southern San Andreas fault was triggered by an earthquake at Parkfield [*Sieh*, 1978]. While the regularity of events and hence the validity of the forecast at Parkfield have recently been questioned [*Real,* 1985; *Toppozada*, 1985] the geodetic data is consistent with the likely occurrence of a magnitude 5.5-6.0 earthquake in the Parkfield region by 1993 [*Segall and Harris*, 1987]. Before discussing the data and our results we briefly review previous studies of the strong-motion data from the 1966 Parkfield earthquake.

Despite a great deal of careful study, there are several issues regarding the 1966 Parkfield earthquake that remain unresolved. One issue is whether the coseismic rupture extended beyond the right-stepping offset in both the surface trace of the San Andreas fault and the aftershock distribution at Gold Hill (Figure 6.1). A number of investigators [*Aki*, 1968; *Anderson*, 1974; *Bouchon*, 1979; *Archuleta and Day*, 1980] have modeled the 1966 earthquake with a fault that extends approximately 30 km to the southwest of the hypocenter, past the right-step. Other investigators [*Trifunac and Udwadia*, 1974; *Lindh and Boore,* 1981] have argued for a shorter rupture zone that extended only 20 km to the southwest of the hypocenter and thus terminated at or near the offset at Gold Hill. A related question is whether the large amplitude ground motion observed at C02 (Figure 6.2) is a source or a propagation effect. Those who argue for a longer source zone attribute the large amplitudes at C02 to the propagation of rupture past the station. Those who argue for a shorter source zone attribute the anomalously large amplitudes to propagation effects.

The length of the source zone is important for several reasons. *Sieh* [1978] suggested that an event at Parkfield may have been a precursor to the great 1857 Fort Tejon earthquake. It is important to know where rupture during the last Parkfield earthquake was arrested. If rupture stops in the same place in each Parkfield earthquake, then the area where it terminates may represent a barrier to further rupture [*Aki*, 1979]. Successive earthquakes at Parkfield would steadily increase the level of stress on the segment of the San Andreas fault immediately to the southeast of the Parkfield earthquakes until it failed [*Tse et al.*, 1985]. In such a scenario it would be important to monitor that segment of the fault immediately after the next Parkfield earthquake.

Another question of interest is the effect of the geometrical obstruction at Gold Hill on the propagation of earthquake rupture. The effects of such obstructions on faulting are unclear, but have received considerable attention [e.g. *Segall and Pollard,* 1980; *Lindh and Boore*, 1981; *Sibson*, 1986]. The effect of a geometrical obstruction on the rupture behavior of the Morgan Hill earthquake is discussed in Chapter 4.

Data

The earthquake was recorded by strong-motion instruments of the Cholame-Shandon array, which consists of three-component, film-recording, analog instruments laid out perpendicular to the fault at a distance of approximately 30 km to the southeast of the epicenter of the 1966 earthquake (Figure 6.1).

For the 1966 earthquake the near-source data are not well-distributed with respect to the source region (Figure 6.1). The four elements of the Cholame-Shandon array: C02, C05, C08, C12, and the station at Temblor, TMB, are all located at the southern end of the rupture zone. This geometry makes it difficult to make definitive statements about the complete rupture history of the earthquake.

Prior to applying our inversion algorithm the data were uniformly sampled and instrument corrected. The data were band-pass filtered with a two-pole zero-phase

Butterworth filter with low- and high-cut corner frequencies at 0.2 and 4.0 Hz. As in the study of the Morgan Hill earthquake we deconvolve a 0.2-s slip velocity function from the data.

The data used to infer the rupture history consist of the horizontal components for the elements of the Cholame-Shandon array that are not located in the fault zone: C05, C08, C12, and TMB (Figure 6.1). Horizontal displacement, calculated from the corrected acceleration data, for the 5 available near-source instruments is shown in Figure 6.2. The component of C02 parallel to the fault was not recorded due to an instrument malfunction. Figure 6.2 demonstrates how large the displacements are at C02 relative to the other stations. If this is a source effect, then the rupture must have propagated very close to the station. We exclude C02 from our analysis of rupture.

The rupture zone considered in our analysis extends from 7 km to the northwest to 33 km to the southeast of the hypocenter (Figure 6.1). The location of the fault is assumed to follow the average surface trace at an azimuth of 141° with a vertical fault plane. In our starting models, rupture is assumed to begin at the instrumental hypocenter (28 Jun 1966 0426:13.4 UTC, 35.955°N, 121.498°W) [*McEvilly et al.*, 1967] and to propagate outward at a fixed fraction of the shear wave velocity over the assumed fault zone.

Theoretical seismograms were calculated using a smoothed version of the *P*-wave model of the Parkfield structure of *Eaton et al.*[1970] (Figure 6.3). The *S*-wave model assumes a constant compressional to shear wave velocity ratio of 1.73, based on a study of aftershocks of the 1966 earthquake [*Lindh and Boore*, 1981].

Sensitivity Tests

The poor station geometry renders the sensitivity tests particularly important. We wish to determine whether the strong-motion data can resolve the extent of the ruptured surface and whether rupture extends to the southeast of the fault offset at Gold Hill. We would also like to determine if the data are consistent with geodetic models of slip during the earthquake

[*Segall and Harris*, 1987] and whether there are any regions of concentrated slip. We have excluded the station C02 from the analysis because there is some indication that it may be strongly affected by propagation effects and because if rupture did extend past Gold Hill, it is too close to the fault for the high-frequency, near-source approximation to be valid.

For the sensitivity tests we adopt a model similar to the geodetic model of *Segall and Harris* [1987]. The slip distribution is smoothly varying over the entire fault. A region of high slip is located from 6-10 km depth and 15-20 km to the southwest of the hypocenter. Unlike the geodetic model, our test model has slip that cuts off abruptly near the offset at Gold Hill. A smaller high-slip region, also not present in the geodetic model, is located at the hypocenter. Rupture velocity is assumed to propagate at a fixed 0.85 times the local shear wave velocity. As in previous test cases, we add correlated noise to the theoretical seismograms, and the windowing and weighting are the same as used when analyzing data from the earthquake itself. The rupture time and slip amplitude model are shown in Figure 6.4. The starting model for a rupture velocity of 0.85 times the shear wave velocity is shown in figure 6.5. In the starting model the slip is smoothly varying and is of low amplitude over the entire fault plane.

The results of the inversion of the synthetic data for five rupture velocities: 0.75, 0.8, 0.85, 0.9, and 0.95 times the local shear wave velocity are shown in Figures 6.6-6.10. The model that best fits the data is for the correct average rupture velocity of 0.85 times the shear wave velocity (Figure 6.8).

For lower values of the rupture velocity the region of high slip at the southern end of the rupture zone occurs closer to the hypocenter and deeper than in the original model; however, the magnitude of the slip amplitude is approximately correct. The fact that we have recovered approximately the correct slip amplitude is due to the near cancellation of two competing factors. Because we are smoothing the slip amplitude in our modeling we tend to underestimate the slip in regions where it is rapidly varying. On the other hand, when we assume a rupture velocity that is too low, the inversion procedure attempts to correct for this

by moving the anomalies and increasing the amount of slip on them, compensating for the reduced effect of directivity at lower rupture velocities.

For the model with the correct rupture velocity the region of high slip near the hypocenter is recovered although the shape is strongly distorted. The region of high slip at the southern end of the rupture is recovered in approximately the correct location; however, it is lower in amplitude and more shallow than in the original model. There is also a small area of slip between 8 and 10 km depth that penetrates by a few kilometers the region that was unslipped in the original model.

For higher assumed rupture velocities the model and the fit to the data degrade rapidly. At a rupture velocity of 0.9 times the shear wave velocity the region of high slip near the hypocenter is recovered, but the vertical extent is very poorly estimated (Figure 6.9). The region of high slip at the southern end of the rupture zone is moved 5 km to the southwest and reduced in depth by about 4 km. At the higher rupture velocity of 0.95 times the shear wave velocity, the region of high slip near the hypocenter is spread over a broad zone, and the region of high slip from 15-20 km along strike is recovered only as a very shallow region of slip from 20-25 km along-strike (Figure 6.10).

Constant Rupture Velocity Model for the Parkfield Earthquake

We now perform the analysis on the data for the Parkfield earthquake itself. The data consist of the horizontal components of the Cholame-Shandon array stations C05, C08, C12, and TMB. The station C02 was excluded from the analysis as mentioned previously. Rupture velocities in excess of 0.85β fit the data very poorly and were characterized by slip distributions that had little slip at all over the principle rupture surface to the southeast of the hypocenter, which is similar to the results obtained in the sensitivity tests when the assumed rupture velocity was too high.

The data are best fit by models with rupture velocities in the range 0.65β-0.75β (Figures 6.11-6.13). A slightly better fit is obtained for the model with an average rupture velocity of 0.7β (Figure 6.12). Rupture velocities in this range result in rupture models that have substantial slip to the southeast of the hypocenter, which is in good agreement with the aftershock distribution, the extent of surface rupture, and previous studies of the strong-motion data.

The best-fitting rupture model has most of the slip occurring within 20 km of the hypocenter (Figure 6.12). The region of highest slip occurs about 10 km along-strike to the southeast and is located at a depth of 10 km. There is a small region of high slip near the hypocenter and a larger region of high slip from 25-30 km to the southeast of the hypocenter. If slip occurred as far as 30 km to the southeast, then the rupture would have propagated well past the right-step in the fault at Gold Hill and very near the station C02. The fact that this region appears to be disconnected in our model does not necessarily mean that it was disconnected in the earthquake. Our results should be interpreted as a high-passed filtered version of the rupture history with low-wavenumber components of the source removed because the seismic data used to estimate the model are themselves band-limited. In addition, even if the two regions of slip were not connected, the barrier model [*Das and Aki*, 1977; *Aki*, 1979] provides a mechanism for discontinuous rupture. However, the most disturbing aspect of this model is that the slip is lowest in exactly the place where the geodetically observed slip is the highest–about 15-25 km to the southeast of the hypocenter [*Segall and Harris*, 1987], so that unless substantial postseismic slip occurred there, it is inconsistent with the geodetic data.

An alternative model, which fits the data slightly less well, has an average rupture velocity of 0.75β with slip distributed to about 24 km to the southeast of the hypocenter (Figure 6.13). There is a small region of slip near 33 km along strike, but this is probably not significant. Another small region of slightly higher slip is located near the hypocenter. The largest slip concentration is located from 10-23 km along-strike, and at a depth ranging

from 2-12 km. The region of highest slip is located the same distance along the fault as the region of high slip found by *Segall and Harris* [1987] from the geodetic data, although it is somewhat more shallow in our model than in theirs. Changes in the rupture front geometry could easily move the high slip region vertically in our model to coincide with the depth of the high-slip region in the geodetically derived model. The fit to the data for this rupture model is shown in Figure 6.14. The large pulse on the x component at C05 and C08 is modeled with a region of high slip rate near Gold Hill. We find a lower amplitude of slip than the geodetic model. The discrepancy could be ascribed to aseismic creep in the postseismic period or the choice of the incorrect average rise time in our analysis.

Finally we consider a model of lower rupture velocity, 0.65β, that also fits the data well. This model has most of the slip occurring within 15 km of the hypocenter (Figure 6.11). The largest concentration of slip is located from 5-10 km along-strike. There is also a substantial amount of slip from 20-25 km along-strike to the southeast. However, in the rest of the region where the geodetically determined slip is high, there is little slip in the rupture model. For this reason we favor the model with a rupture velocity of 0.75β.

The teleseismically-determined seismic moment of the 1966 Parkfield earthquake was approximately 1.5×10^{18} Nm [*Tsai and Aki*, 1969]. We obtain a seismic moment of 2.1×10^{18} Nm from our analysis of the strong motion data. This is not a significant difference due to our poor resolution of the rupture behavior over much of the fault.

To summarize we have analyzed the 1966 Parkfield earthquake using simple, constant-velocity rupture models. We prefer the model with a rupture velocity of 0.75β for the Parkfield earthquake (Figure 6.13). This model has the virtue of being consistent with the geodetic estimate of the coseismic slip. It is also supported by several other estimates of the average rupture velocity [*Haskell*, 1969; *Trifunac and Udwadia*, 1974; *Levy and Mal*, 1976; *Lindh and Boore*, 1981]. It should be noted however, that other studies [*Eaton*, 1967; *Aki*, 1968] found slower rupture velocities of approximately 0.65β.

Within the confines of our simple assumptions, the preferred model supports the

conclusion of *Lindh and Boore* [1981] that coseismic rupture did not extend much to the south of Gold Hill. However we must be careful in this interpretation because it assumes that rupture velocity is constant. A rupture model in which rupture is delayed somewhat near Gold Hill and then continues to the southeast would also fit the data and could include significant slip well to the south of Gold Hill. The results from the previous two Chapters indicate that this may be a common occurrence during seismic rupture particularly in regions of complex fault geometry like the offset near Gold Hill. Thus we can only say from our analysis that we weakly favor the shorter rupture zone. To provide a more definitive answer to the question of the extent of rupture propagation in this earthquake it will be necessary to analyze data that is more evenly distributed about the rupture zone, such as the regional-distance Wood-Anderson data.

In the preferred model the most pronounced feature is a region of high slip from 15-23 km to the southeast of the hypocenter. This location coincides approximately with the location of a high-slip region found by the geodetic data. It is also the part of the fault near Gold Hill. As was the case in the Morgan Hill earthquake, the geometric complexity of the offset at Gold Hill may have acted to store strain energy in the interseismic period. When the earthquake occurred, slip on this part of the fault was greater than on surrounding regions. From the available data we are unable to determine whether the Parkfield earthquake exhibited the same sort of complexity in the behavior of the rupture front as the Morgan Hill earthquake. The Parkfield area is now one of the most heavily instrumented seismic regions in the world. When the next Parkfield earthquake occurs, it will provide a truly exceptional opportunity to study the details of fault rupture and such complexity will be easily resolved.

TABLE 6.1 Trigger Times

Station	Assumed (s)
C02	8.9
C05	6.3
C08	9.9
C12	9.9
TMB	11.9

Figure Captions

Figure 6.1 Strong-motion stations (triangles) are shown with respect to the surface rupture.

Figure 6.2 Displacement calculated from records of acceleration for the 5 near-source stations that recorded the 1966 Parkfield earthquake. The component of motion parallel to the fault at station C02 malfunctioned during the earthquake.

Figure 6.3 The smoothed gradient velocity model used in our analysis is shown with a solid line. It is an approximation to the velocity model of *Eaton et al.* [1970] for the Parkfield region. S wave velocities are derived assuming a constant compressional to shear wave velocity ratio of 1.73 based on aftershocks of the 1966 earthquake.

Figure 6.4 The rupture model used for the synthetic test case is shown. The region of high slip near the hypocenter is based loosely on the geodetic results of *Segall and Harris* [1987]. The region of high slip near the hypocenter was introduced arbitrarily to test our ability to resolve slip there. Rupture velocity is assumed to be a constant fraction, 0.85, times the local shear wave velocity.

Figure 6.5 The starting model for subsequent inversions presented in this Chapter. For this case the rupture velocity is 0.65β.

Figure 6.6 Sensitivity test for slip only assuming a rupture velocity of 0.75β.

Figure 6.7 Sensitivity test for slip only assuming a rupture velocity of 0.80β.

Figure 6.8 Sensitivity test for slip only assuming a rupture velocity of 0.85β.

Figure 6.9 Sensitivity test for slip only assuming a rupture velocity of 0.90β.

Figure 6.10 Sensitivity test for slip only assuming a rupture velocity of 0.95β.

Figure 6.11 Results of an inversion of the Parkfield data for slip only assuming a rupture velocity of 0.65β.

Figure 6.12 Results of an inversion of the Parkfield data for slip only assuming a rupture velocity of 0.70β. Although this solution fits the data slightly better than other models it conflicts with geodetic observations that detect a substantial amount of slip on the region of the fault near Gold Hill.

Figure 6.13 Results of an inversion of the Parkfield data for slip only assuming a rupture velocity of 0.75β. This is our preferred model.

Figure 6.14 The data (upper) and the theoretical (lower) seismograms for the deconvolved displacement are shown for the preferred model. The model, shown in Figure 6.13 has an average rupture velocity of 0.75β and a region of high slip near Gold Hill. This region of high slip is the source of the high-amplitude pulse on the x component of stations C05 and C08.

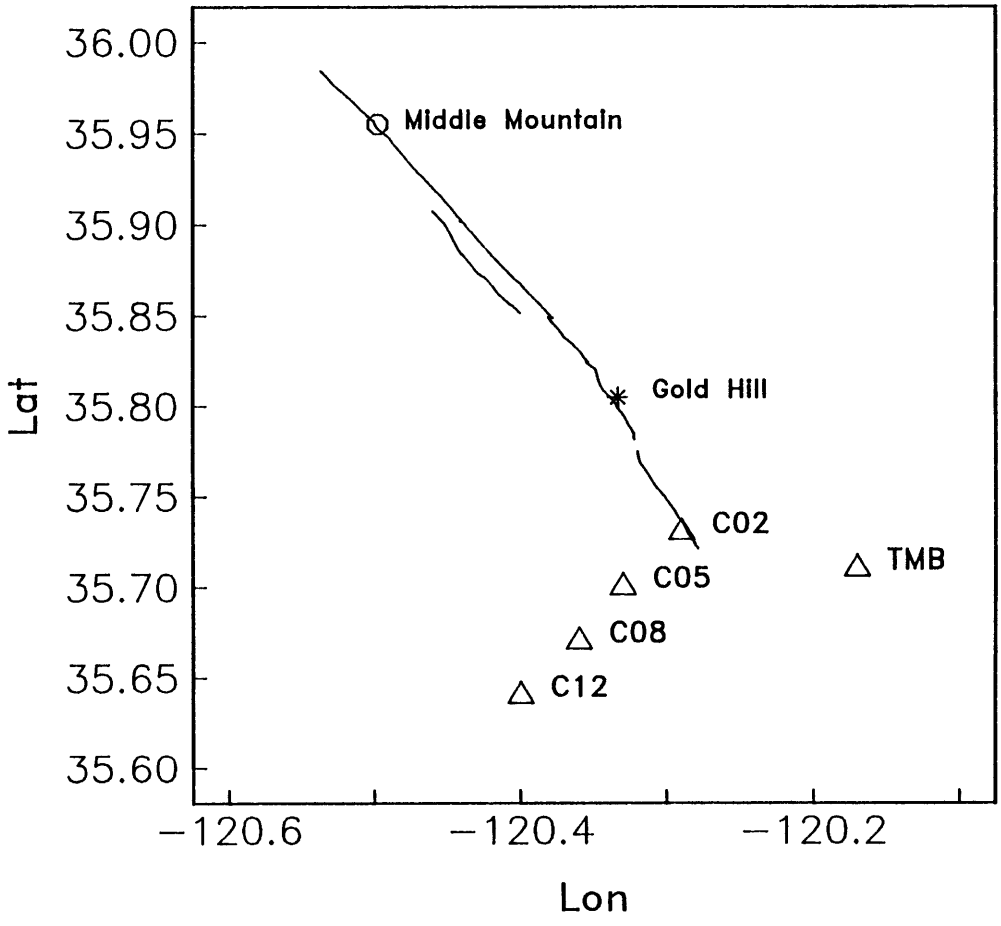
36.00
35.95
35.90
35.85
35.80
35.75
35.70
35.65
35.60
Lat
Middle Mountain
Gold Hill
C02
C05
C08
C12
TMB
−120.6
−120.4
−120.2
Lon

Figure 6.1

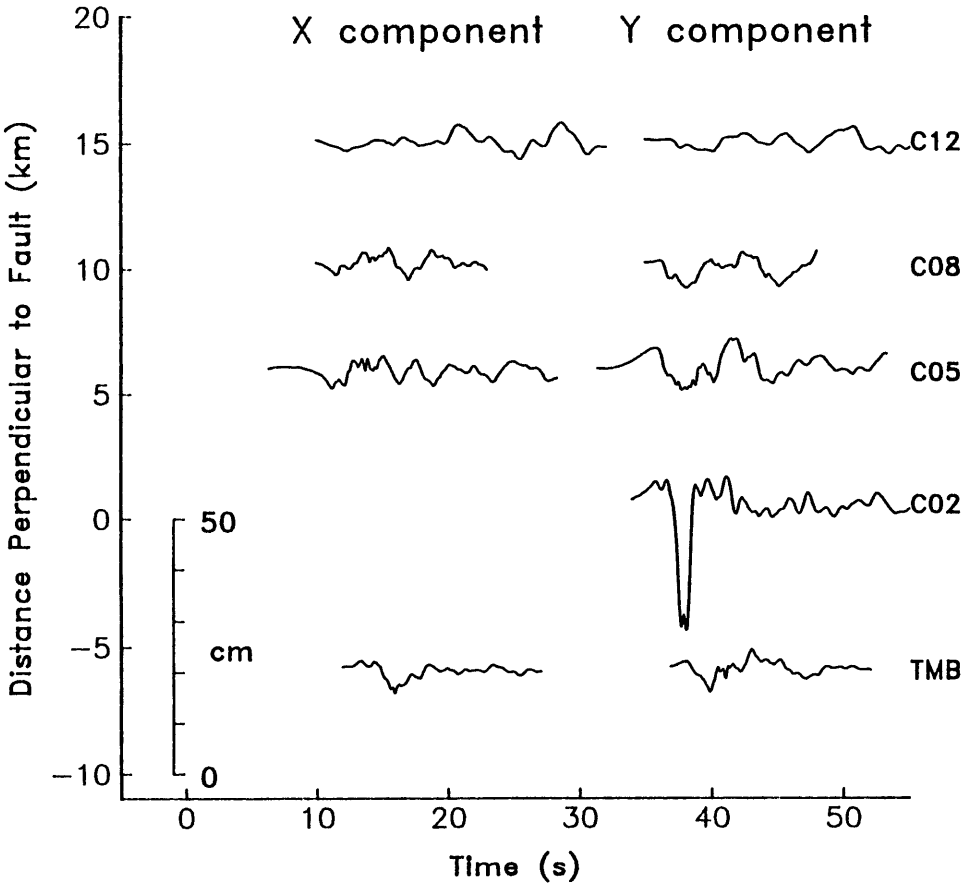
X component
Y component
Distance Perpendicular to Fault (km)
20
15
10
5
0
−5
−10
C12
C08
C05
C02
TMB
50
cm
0
0
10
20
30
40
50
Time (s)

Figure 6.2

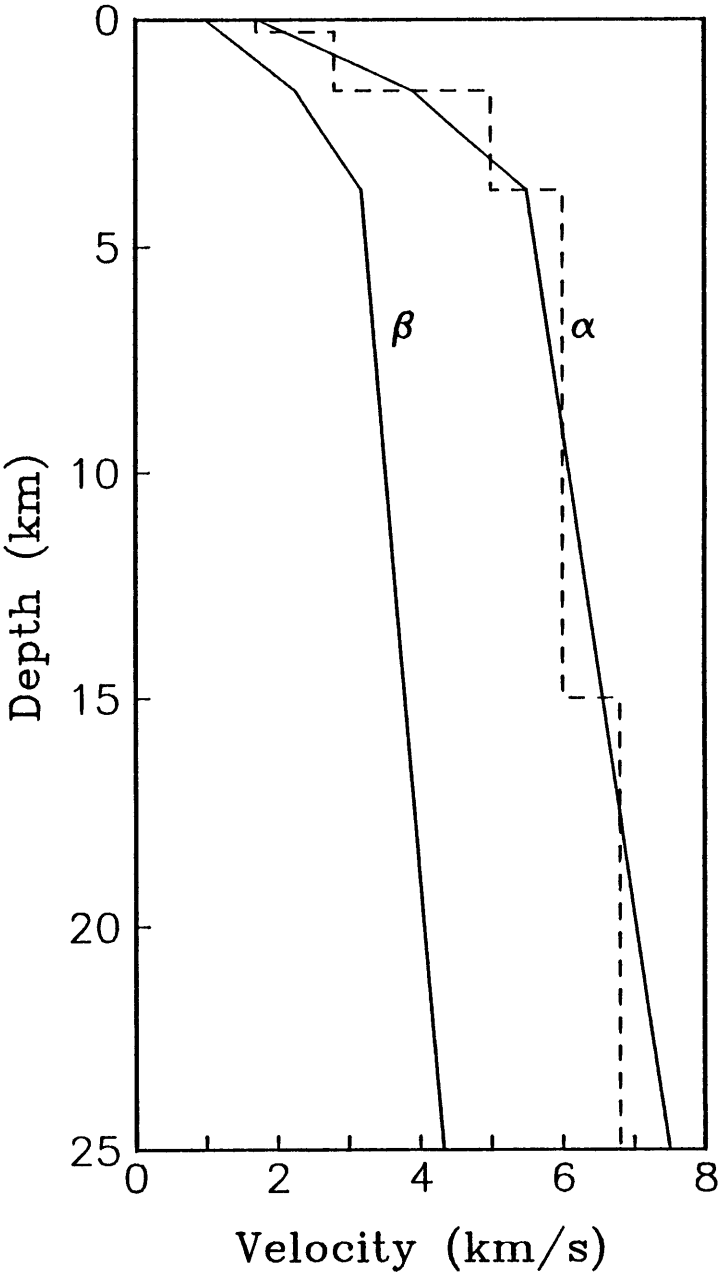

Figure 6.3

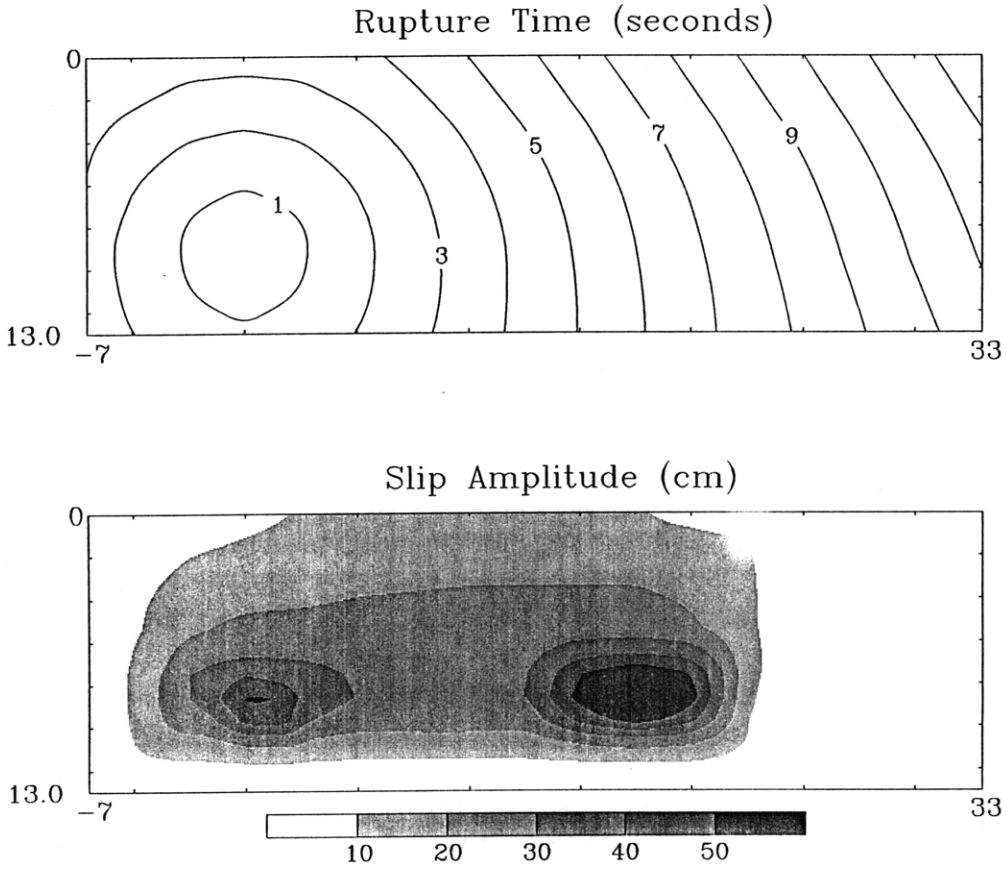
Rupture Time (seconds)
0
1
3
5
7
9
13.0
-7
33
Slip Amplitude (cm)
0
13.0
-7
33
10
20
30
40
50

Figure 6.4

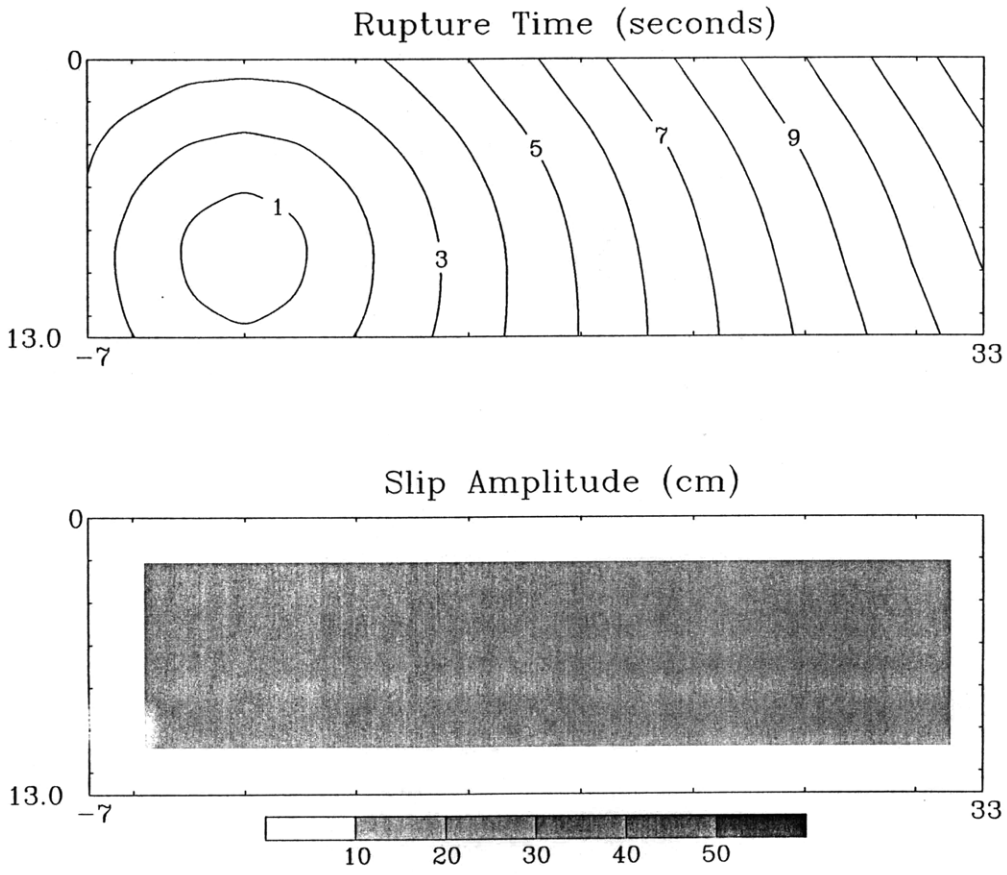
Rupture Time (seconds)
0
1
3
5
7
9
13.0
−7
33
Slip Amplitude (cm)
0
13.0
−7
33
10
20
30
40
50

Figure 6.5

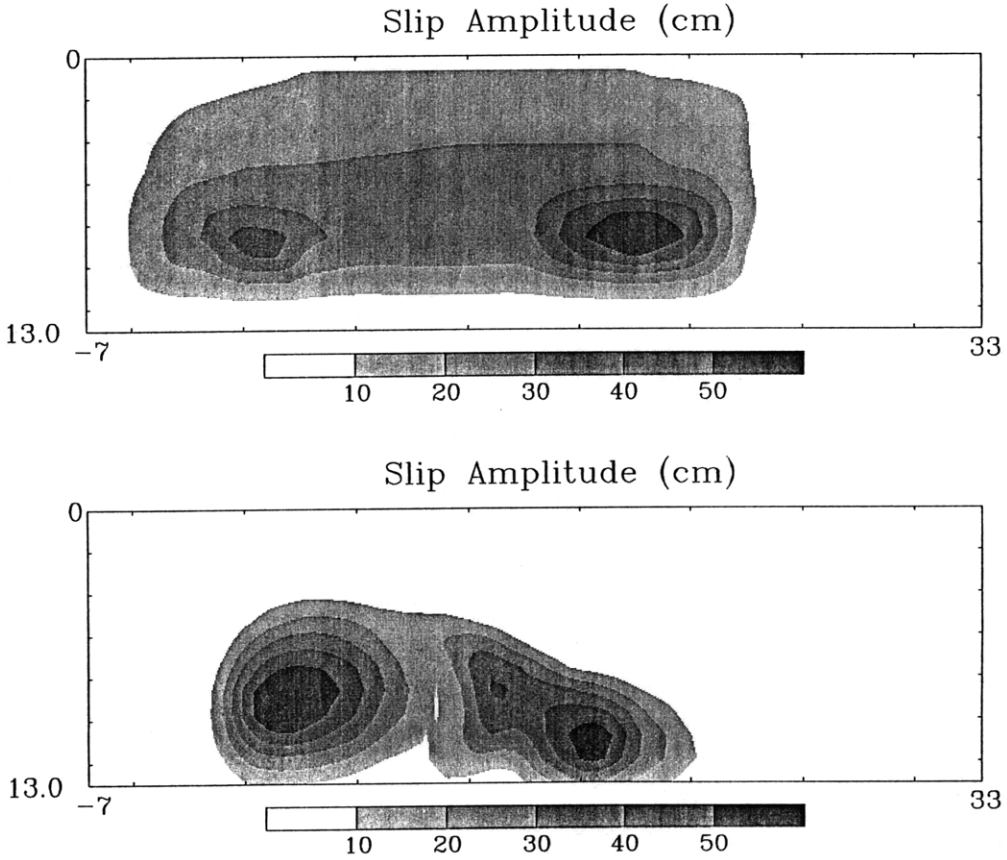
Slip Amplitude (cm)
0
13.0
−7
33
10
20
30
40
50
Slip Amplitude (cm)
0
13.0
−7
33
10
20
30
40
50

Figure 6.6

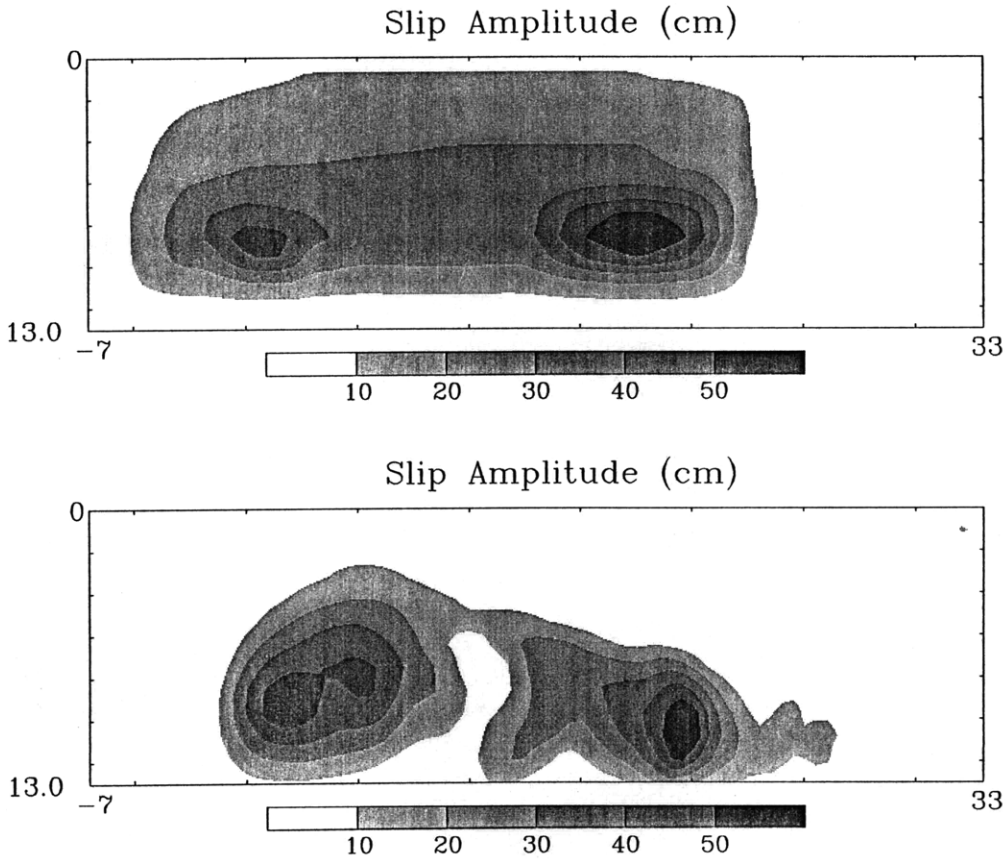
Slip Amplitude (cm)
0
13.0
−7
33
10
20
30
40
50
Slip Amplitude (cm)
0
13.0
−7
33
10
20
30
40
50

Figure 6.7

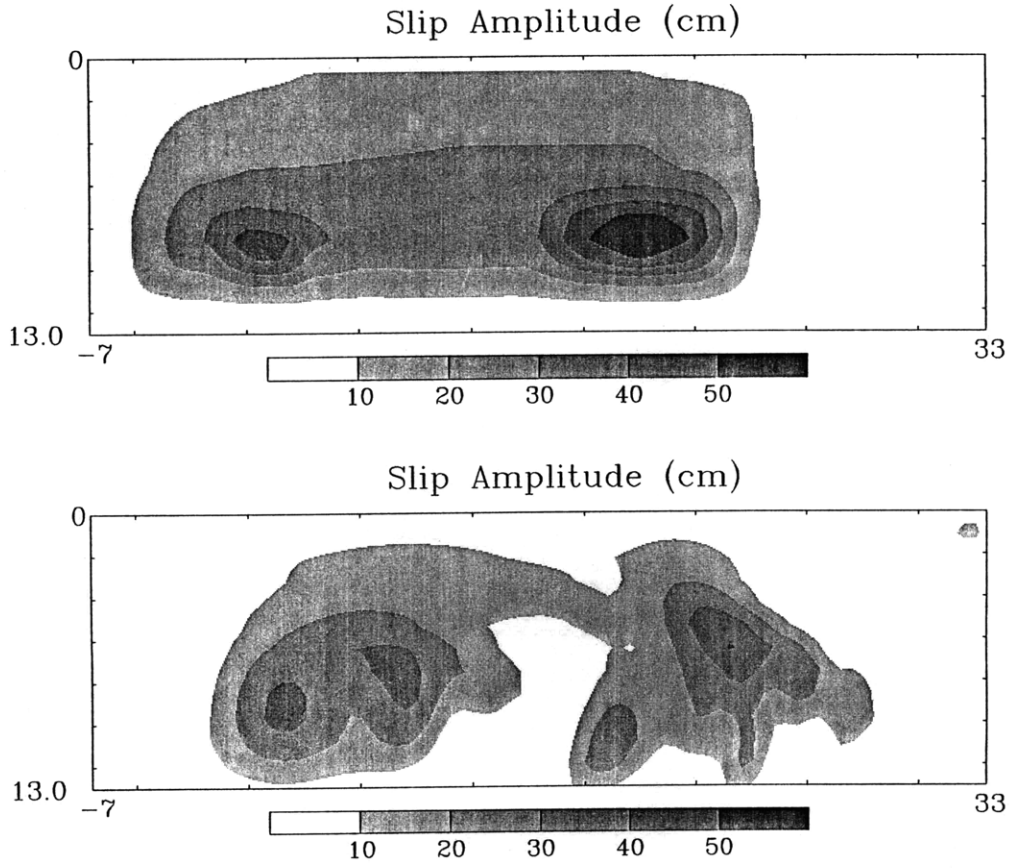
Slip Amplitude (cm)
0
13.0
-7
33
10
20
30
40
50
Slip Amplitude (cm)
0
13.0
-7
33
10
20
30
40
50

Figure 6.8

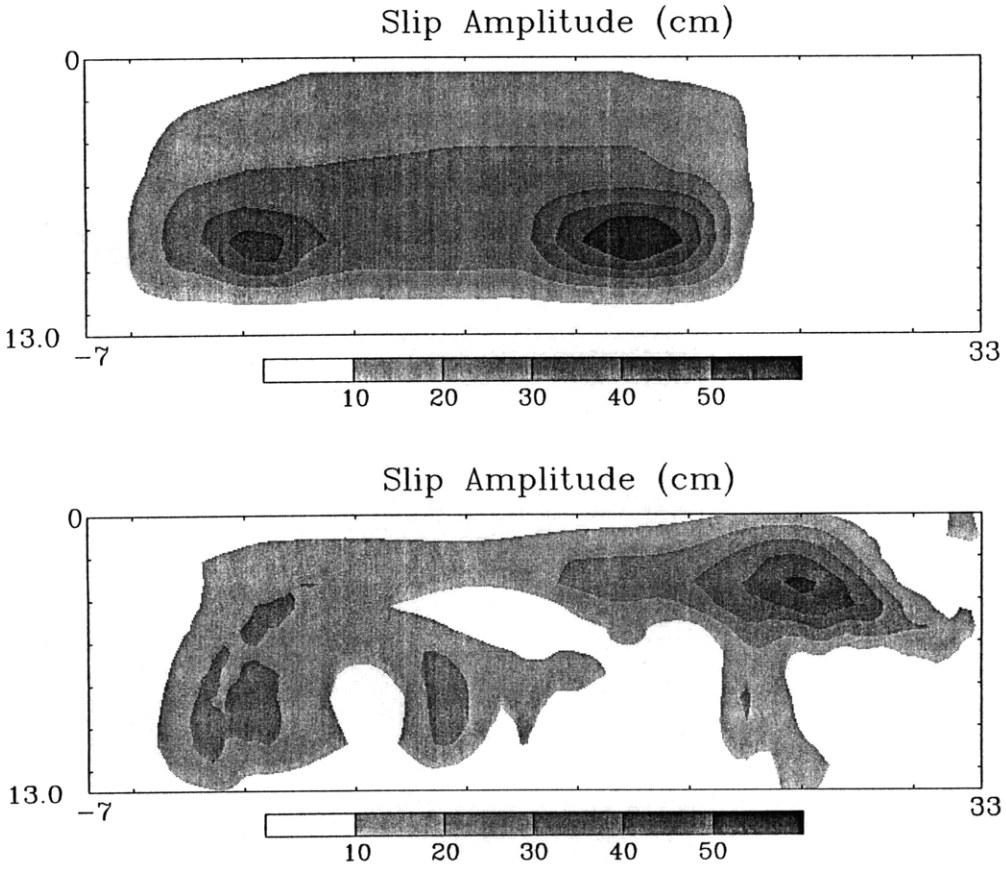
Slip Amplitude (cm)
0
13.0
-7
33
10
20
30
40
50
Slip Amplitude (cm)
0
13.0
-7
33
10
20
30
40
50

Figure 6.9

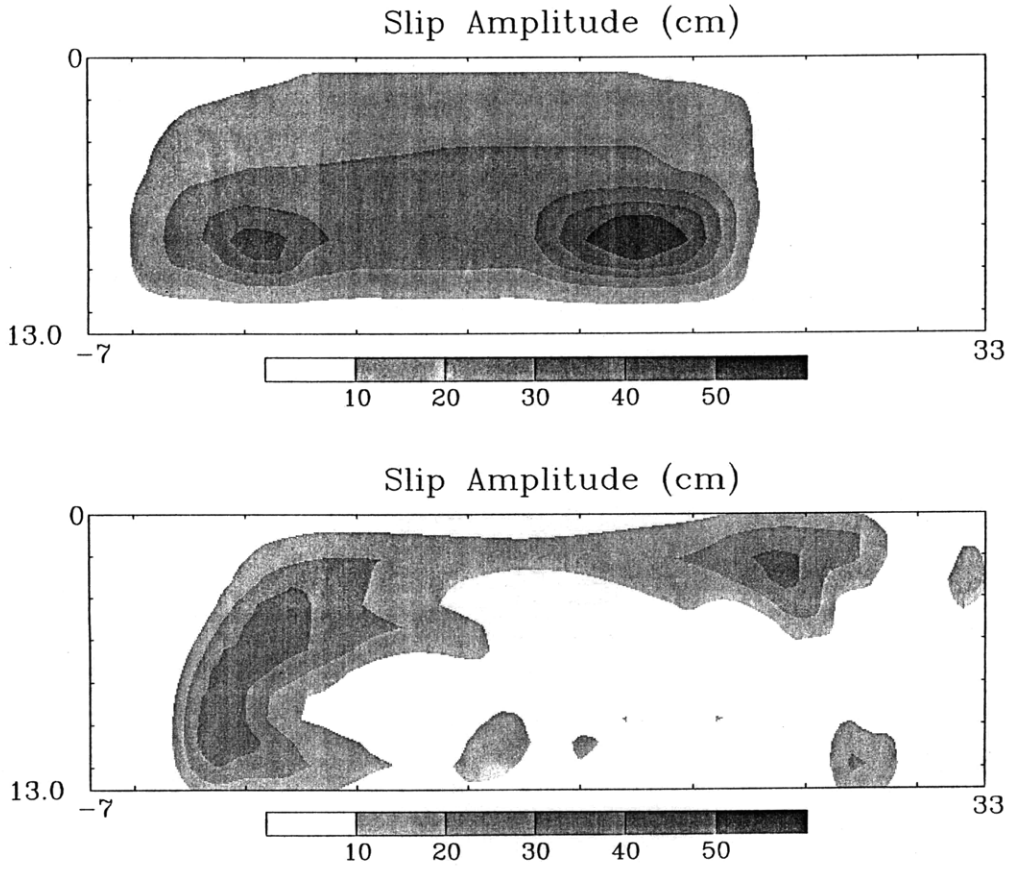
Slip Amplitude (cm)
0
13.0
−7
33
10
20
30
40
50
Slip Amplitude (cm)
0
13.0
−7
33
10
20
30
40
50

Figure 6.10

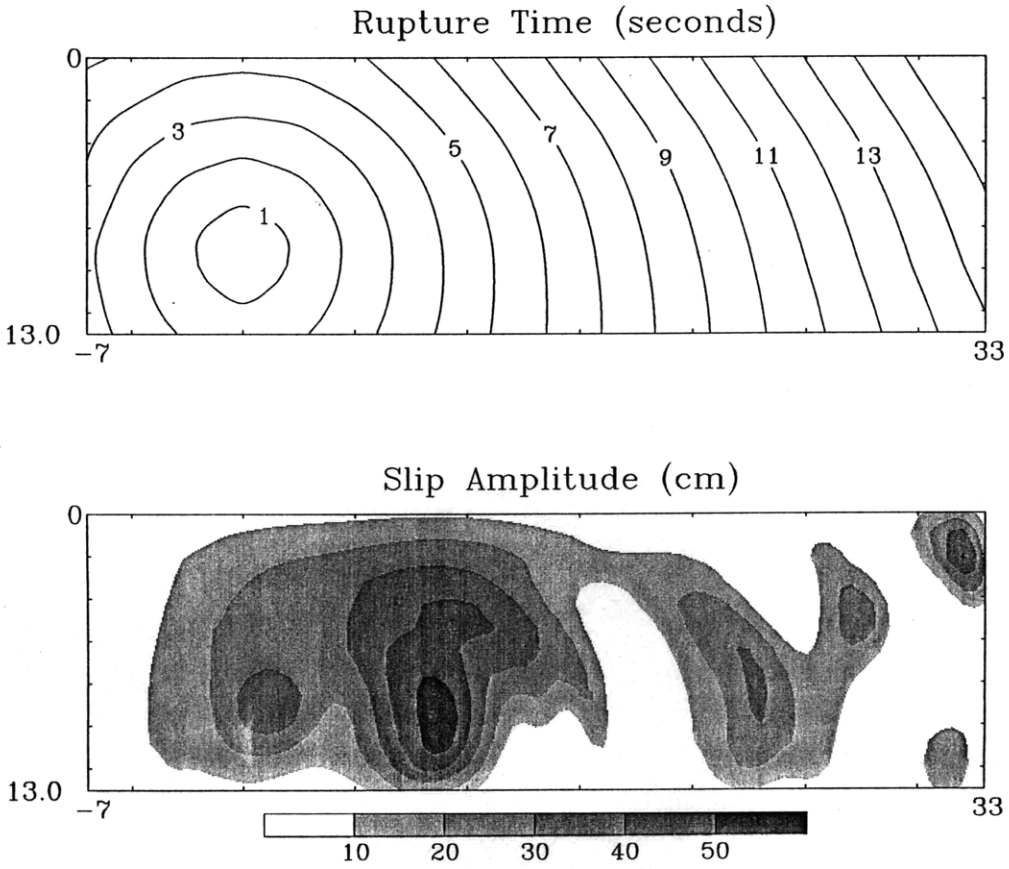
Rupture Time (seconds)
0
3
5
7
9
11
13
1
13.0
−7
33
Slip Amplitude (cm)
0
13.0
−7
33
10
20
30
40
50

Figure 6.11

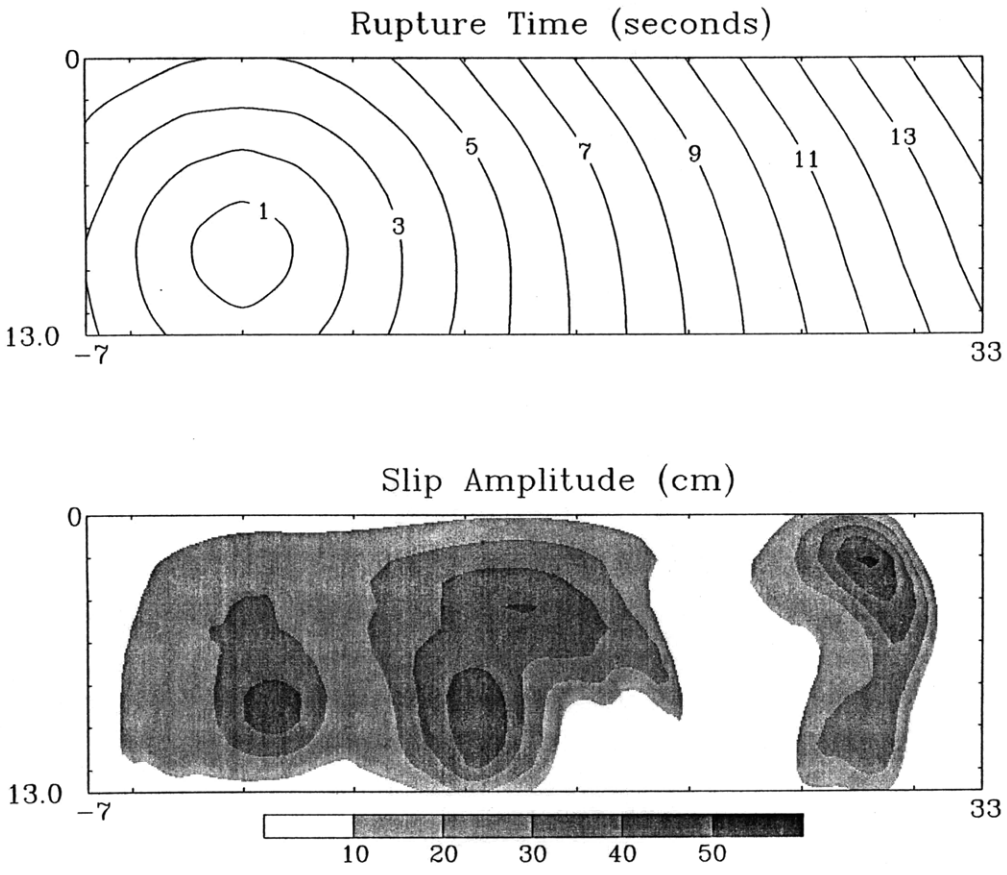
Rupture Time (seconds)
0
1
3
5
7
9
11
13
13.0
−7
33
Slip Amplitude (cm)
0
13.0
−7
33
10
20
30
40
50

Figure 6.12

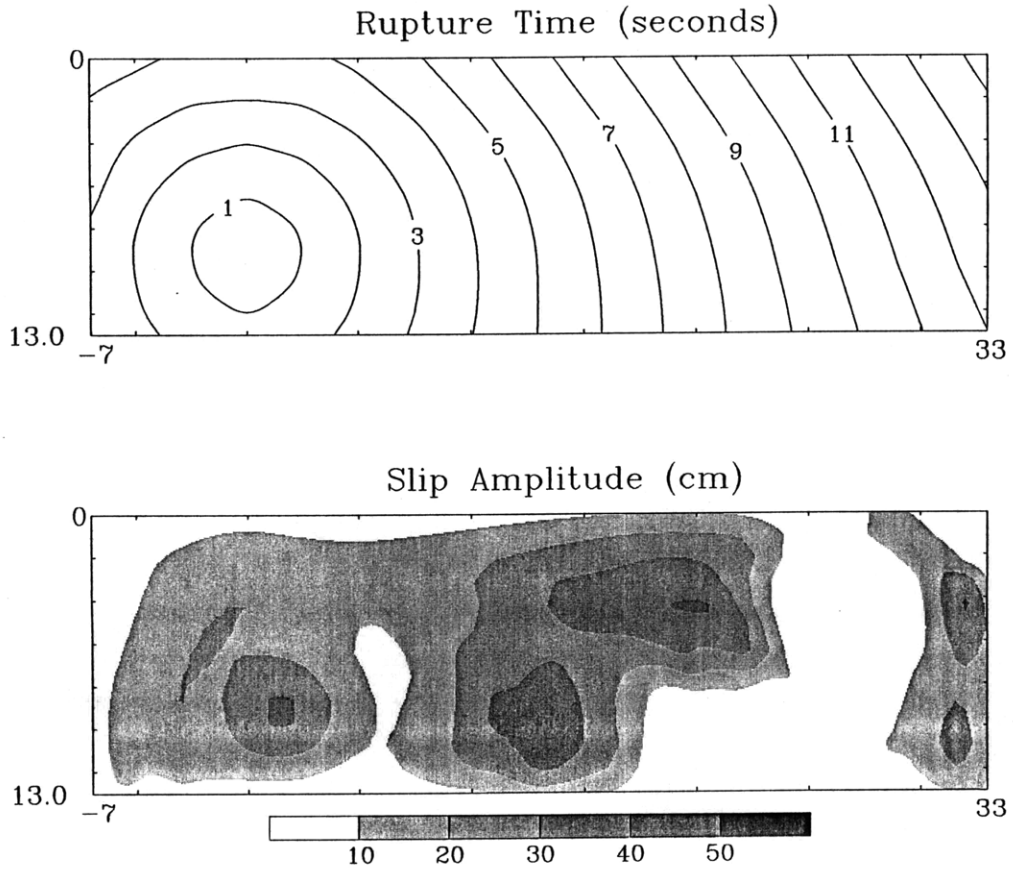
Rupture Time (seconds)
0
1
3
5
7
9
11
13.0
−7
33
Slip Amplitude (cm)
0
13.0
−7
33
10
20
30
40
50

Figure 6.13

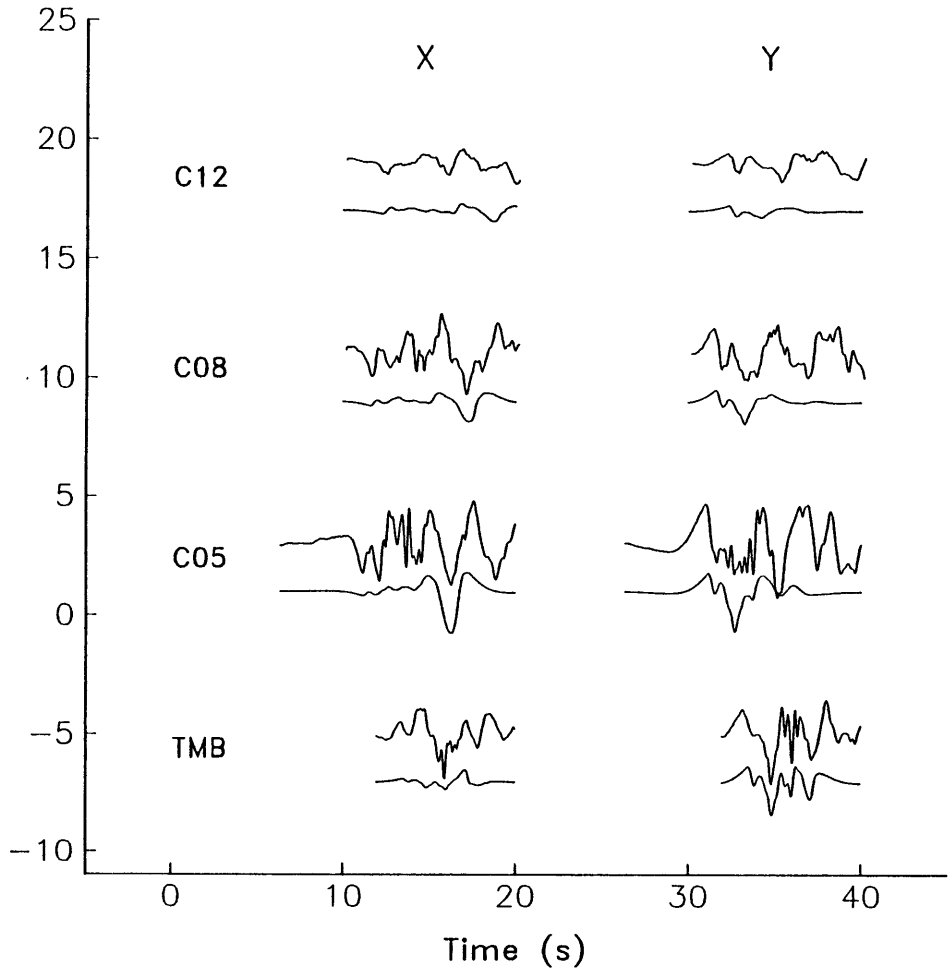

Figure 6.14

CHAPTER 7

OBSERVATIONAL CONSTRAINTS ON EARTHQUAKE RUPTURE DYNAMICS

In this chapter we discuss the the results obtained in previous chapters and the implications they have for earthquake rupture dynamics. We derive an estimate of the shear fracture energy for each of the earthquakes we have studied using average values for the slip intensity. There are notable deviations of our observations from idealized models of slip on a planar fault for which we propose possible explanations. The role of fault-zone heterogeneity in the dynamics of seismic rupture is also discussed.

Earthquakes as Elastodynamic Shear Cracks

Earthquakes are usually modeled as point sources or as distributed dislocations across fault surfaces. While this approach has led to much insight into earthquake source behavior, it is limited in utility and scope because it is purely kinematic and ignores much of the physics of material failure. Dynamic crack models are an attempt to describe the physical processes of rupture by imposing reasonable boundary conditions on the crack surface, and by requiring a finite amount of energy to be expended in extending the crack. Before discussing the implications of our results for earthquake rupture dynamics, we briefly review some relevant concepts from fracture mechanics.

For a fault plane with normal $\hat{\mathbf{z}}$, extending to infinity in the $\pm y$ direction, and propagating in the x direction, three modes of fracture may be defined (Table 7.1).

TABLE 7.1 Nomenclature for Elastodynamic Cracks

Mode	Type	Stress Relaxed	Slip Direction
I	Tensile	σ_{zz}	z
II	Inplane	σ_{zx}	x
III	Antiplane	σ_{zy}	y

Most of the fracture mechanics literature analyzes Mode-I cracks because they are the most relevant for engineering applications. We are primarily interested in models of antiplane and inplane shear fracture (Mode-II and Mode-III). In general, three-dimensional shear cracks will be a mixture of Mode-II and Mode-III. On such a crack the propagation of the two modes is uncoupled except where the crack front has sharp corners. This provides a justification for considering two-dimensional, single-mode cracks for three-dimensional problems.

Following *Madariaga* [1985], if we let $l(t)$ describe the position of the crack tip with time, the boundary conditions to be satisfied on the $z = 0$ plane are

Specified stress drop behind tip $\quad \sigma(x) = \Delta\sigma(x) \quad x < l(t)$ (7.1)

No slip ahead of tip $\quad \Delta u(x) = 0 \quad x > l(t)$ (7.2)

where σ and Δu are the stress and displacement components appropriate for the mode considered. The mixed boundary conditions of stress and displacement make this a difficult problem to solve.

Asymptotic solutions, valid near the crack tip behave similarly for all modes of fracture [*Rice*, 1980]. For a static crack with an integrable energy density near the tip, the only

dependence of stress on r, the distance from the tip, that satisfies the above boundary conditions and is singular near the crack tip has $\sigma \sim r^{-1/2}$. This term dominates since other terms are either finite or zero near the tip [*Rice*, 1980]. The inverse square root of r dependence for the static crack solution is shared by dynamically extending cracks for which the amplitude is modified by factors that depend on the rupture velocity [*Freund*, 1979]. These factors decrease from a value of one for a rupture velocity of zero to a value of zero for a rupture velocity equal to the limiting speed of rupture for the mode. The limiting speed for Mode-II cracks is the Rayleigh wave velocity and the limiting speed for Mode-III cracks is the shear wave velocity.

Following *Madariaga* [1985] the stress and slip velocities for a semi-infinite crack moving at constant rupture velocity can be expressed as

$$\sigma(x) = K[x - l(t)]^{-1/2} \tag{7.3}$$

$$\Delta\dot{u}(x) = V[l(t) - x]^{-1/2} \tag{7.4}$$

where the stress intensity factor, K, with units of Pa $m^{1/2}$, and the dynamic velocity intensity factor, V, with units of $m^{3/2}$ s^{-1}, describe the strength of the singularities and are related by the expressions

$$K = \frac{\mu}{2v_r}\left(\frac{\beta}{v_r}\right)^2 R(v_r)\left[1 - \left(\frac{v_r}{\beta}\right)^2\right]^{-1/2} V \tag{7.5}$$

for a Mode-II crack and

$$K = \frac{\mu}{2v_r}\left[1 - \left(\frac{v_r}{\beta}\right)^2\right]^{1/2} V \tag{7.6}$$

for a Mode-III crack, where $R(v_r)$ is the Rayleigh function

$$R(v_r) = 4\left[1 - \left(\frac{v_r}{\beta}\right)^2\right]^{1/2}\left[1 - \left(\frac{v_r}{\alpha}\right)^2\right]^{1/2} - \left[2 - \left(\frac{v_r}{\beta}\right)^2\right]^2 \qquad (7.7)$$

For Mode-II the limiting rupture velocity is the Rayleigh wave velocity and for Mode-III the limiting velocity is the shear wave velocity.

The singularities in slip velocity behind the crack tip and in stress ahead of the crack tip are a consequence of having assumed that the material remains elastic and that stress is proportional to strain until the stress becomes infinite. Obviously this is not a realistic model. It can be modified by invoking a constitutive relation near the crack tip to include a slip-weakening zone, in which the yield stress is exceeded [*Ida,* 1972]. In the slip-weakening model the crack starts to slip once a critical stress level σ^t is attained. Once this happens a slip-weakening law relates slip and stress $\sigma(\Delta u)$. Further weakening occurs until a critical value of displacement, D, is achieved at which time the stress has fallen to the frictional level. In slip-weakening models, rupture velocities well in excess of the critical velocity and approaching the compressional wave velocity are possible [*Burridge*, 1973; *Andrews*, 1976].

In the subsequent analysis we consider crack propagation at velocities below the critical velocity for an elastic-brittle crack with the understanding that for real materials the slip velocity and stress intensity singularities will be smoothed. The analysis of slip-weakening cracks using elastic-brittle analysis is adequate provided the size of the slip-weakening zone is much smaller than the overall size of the crack [*Rice*, 1980].

Fracture Energy

A fundamental parameter for describing earthquakes in terms of fracture mechanics is the shear fracture energy, G. The shear fracture energy is a generalization of concept of the specific surface energy, which is defined as the amount of energy needed to create a unit area

of surface by tensile fracture. In an intact material, the specific surface energy is a rough measure of the strength and density of atomic bonds across a surface. It has been measured in laboratory experiments by making a notch in a sample and pulling it apart in a tensile mode. [*Brace and Walsh*, 1962] performed such experiments and obtained values in the range of 0.1 to 1.0 J/m^2 for the specific surface energy of quartz and feldspar.

The concept of surface energy has been generalized for shear fracture to mean the amount of energy absorbed per unit advance of a crack in a shearing mode. The relation between tensile and shear fracture energy is unclear, except that specific surface energy should provide a lower bound for shear fracture energy. Shear fracture energy tends to be about 2 orders of magnitude higher than the specific surface energy in laboratory experiments [*Wong*; 1982].

For an ideal elastic crack, energy flow into the crack tip can be determined by calculating the work done in extending the fracture. The only place where the slip velocity and traction are non-zero, and hence where work is done, in an elastic-brittle crack is at the tip itself where both are singular. For the slip-weakening model, work expended in extending the crack tip takes place over the length of the slip-weakening zone. The work done is simply the area under the stress-displacement curve which comes from the constitutive relation, $\sigma = \sigma(\Delta u)$, in the cohesive zone [*Rice*, 1980].

Rice [1980] estimated G from post-failure behavior of lab samples by integrating the stress-displacement curve for rocks in a triaxial experiment done at high confining pressure (470 MPa). He obtained values ranging from 4.5 x 10^4 to 7.3 x 10^4 J/m^2. *Okubo and Dieterich* [1984] estimated G in a biaxial experiment under normal stresses ranging from 0.6 to 4.0 MPa and found values of G ranging from 0.2 to 2.4 J/m^2. They also noted that G increased with normal stress and fault roughness; however, the rate of increase with normal stress would predict fracture energies on the order of 400 J/m^2 for the magnitude of the normal stress used in the triaxial tests, leaving a discrepancy of 2 orders of magnitude in the laboratory data. One explanation is that the extrapolation of the low normal stress

dependence of G to higher normal stresses is invalid. Another is that the triaxial tests were done with intact samples, and the biaxial experiments were done with precut samples. In addition for the triaxial experiments the size of the triaxial specimens was only about 5 % of the slip-weakening zone size so that the whole sample was slipping simultaneously, violating the assumed geometry. *Wong* [1982] applied this technique to a large amount of data and found values of G ranging from 0.8 to 7.3×10^4 J/m^2. He also found that D is on the order of mm and d the slip-weakening zone length, is on the order of tens of cm. *Wong* [1982, 1986] also calculated values of G for laboratory data and obtained values ranging from 0.7×10^4 to 5.1 x 10^4 J/m^2 for normal stresses ranging from 80 to 250 MPa over a wide range of temperatures.

Ida [1973] using observations of accelerations and velocities was the first to estimate the shear fracture energy of earthquakes. He found that the specific fracture energy was as large as 10^7 J/m^2. *Husseini et al.* [1975] assumed that an earthquake stops due to a decrease in the tractions along the fault available to induce fracture in their estimation of G. They applied their technique to a large set of data ranging from deep earthquakes in Tonga to aftershocks of the San Fernando earthquake and obtained values of G from 10 to 10^6 J/m^2. The lower values of G were attributed to frictional sliding on a pre-existing surface, and higher values with fracture of intact material. *Das* [1976] found values of G ranging from 10^6 to 10^8 J/m^2 based on observations of earthquake rupture velocities.

Seismic estimates of G are very uncertain. For example *Aki* [1979] used the barrier model to estimate G for the 1966 Parkfield earthquake and obtained a value of $G = 8 \times 10^5$ J/m^2. *Husseini et al* [1975] estimated $G = 1.1 \times 10^2$ J/m^2 for the same event. Part of this discrepancy is that *Aki* [1979] estimated G for the barrier that stopped the earthquake and *Husseini et al.* [1975] estimated it for the entire earthquake. Nevertheless a range of nearly four orders of magnitude in estimates of G for a single earthquake is quite large. *Rice and Simons* [1976] analyzed a creep event on the San Andreas fault and obtained $G = 2.6 \times 10^2$

J/m^2. Because creep events are thought to occur on relatively weak fault zones, this may provide a realistic lower bound on G during normal earthquakes.

In our modeling of earthquake rupture for the Morgan Hill, Imperial Valley, and Parkfield earthquakes we parameterized the rupture history using the rupture time and the slip intensity, $S = |s|$. For a constant rupture velocity, the slip intensity is directly related to the dynamic velocity intensity factor, V, by the square root of the rupture velocity

$$V = v_r^{1/2} S \tag{7.9}$$

For Mode-II and Mode-III cracks there is a relation between S and K, the stress intensity factor. For Mode-II cracks

$$K = \frac{\mu}{2v_r}\left(\frac{\beta}{v_r}\right)^2 R(v_r)\left[1 - \left(\frac{v_r}{\beta}\right)^2\right]^{-1/2} v_r^{1/2} S \tag{7.10}$$

and for Mode-III cracks

$$K = \frac{\mu}{2v_r}\left[1 - \left(\frac{v_r}{\beta}\right)^2\right]^{1/2} v_r^{1/2} S \tag{7.11}$$

Madariaga [1985]. The shear fracture energy G is given by *Kostrov and Nikitin* [1970] as

$$G = \frac{\pi}{2v_r} K V \tag{7.12}$$

Expressed in terms of the slip intensity S, for Mode-II cracks we have

$$G = \frac{\pi\mu\beta^2}{4v_r^3} R(v_r)\left[1 - \left(\frac{v_r}{\beta}\right)^2\right]^{-1/2} S^2 \tag{7.13}$$

and for Mode-III cracks

$$G = \frac{\pi\mu}{4v_r}\left[1 - \left(\frac{v_r}{\beta}\right)^2\right]^{1/2} S^2 \qquad (7.14)$$

Equations (7.13) and (7.14) express the fracture energy, G, in terms of quantities that are directly estimated in our inversion procedure. Thus our results will yield two estimates for G one for Mode-II and one for Mode-III cracks. In practice we have found that for the events we have studied, equations (7.13-7.14) yield approximately the same values of G for each mode.

For the Morgan Hill earthquake our estimate of G for both Mode-II and Mode-III cracks based on the approximate values: $\mu = 3.0 \times 10^{10}$ Pa, $v_r = 2.4 \times 10^3$ m/s, $\beta = 3.0 \times 10^3$ m/s, and $S = 0.5$ ms$^{-1/2}$ is approximately 1-2 $\times 10^6$ J/m^2. For the Imperial Valley earthquake using the values of $v_r = 2.6 \times 10^3$ m/s, $\beta = 3.2 \times 10^3$ m/s, and $S = 0.4$ ms$^{-1/2}$ we obtain a slightly smaller value of $G = 9 \times 10^5$ J/m^2. For the Parkfield earthquake using the values of $v_r = 2.5 \times 10^3$ m/s, $\beta = 3.3 \times 10^3$ m/s, and $S = 0.3$ ms$^{-1/2}$ we obtain G = 5-6 $\times 10^5$ J/m^2. The relatively low value for Parkfield is a consequence of a lower rupture velocity and a smaller slip intensity for this earthquake than for the other earthquakes. Although our estimates of G vary by a factor of nearly 4 between the different earthquakes, the differences are probably not significant due to the strong dependence of the estimates on the rupture velocity.

It is difficult to assess how reliable our estimates of G based on equations (7.14-7.15) are. These relations are derived for semi-infinite, single-mode shear cracks propagating at constant rupture velocity. Since this is not a realistic model for earthquakes it is not obvious that an estimate of G based on these relations would be worthwhile. For this reason we have

checked our procedure by applying it to a numerical simulation of a complex rupture presented by *Day* [1979] in which the shear fracture energy is known.

Day [1979] used a slip-weakening model with realistic values of the slip-weakening zone size and the slip-weakening displacement to study three-dimensional rupture propagation. His model is complicated in that it is mixed mode, includes variable prestress, and has episodes of supershear rupture propagation. We estimated G using the peak slip rates and rupture velocities obtained by *Day* [1979] together with our assumption of the square-root singularity slip velocity function using equations (7.13-7.14). The estimates of G for portions of the fault where the rupture velocity is subshear are within a factor of two of the correct value and the results for the fault as a whole are off by a factor of less than three. Although these are fairly large discrepancies, the uncertainty in estimates of G for a single earthquake can be several orders of magnitude. Thus the idealized two-dimensional elastic-brittle approximation is in rough agreement with the results for a heterogeneous, three-dimensional, slip-weakening model.

The values we have obtained for the shear fracture energy are within the wide range of values found previously for earthquakes; however, they are substantially larger than estimates based on experimental data [e.g., *Wong*, 1982], which are generally less than 10^4 J/m^2. A likely source for this difference is the complexity of rupture propagation during an earthquake. If seismic faulting consists of the breaking of an assemblage of cracks with a greater total surface area than a simple fault plane, much more energy will be expended to extend the rupture.

Fault Heterogeneity and Earthquake Rupture Dynamics

Our models of earthquake rupture for each of the earthquakes studied exhibit considerable heterogeneity in both the distribution of slip and the propagation of the rupture front. The Morgan Hill earthquake had an episode of delayed or even reversed rupture propagation near Anderson Reservoir. The Imperial Valley earthquake had several events in which both the

slip and rupture time were locally variable. The Parkfield earthquake also showed evidence for a large-slip region near Gold Hill, but because of the poor station geometry the nature of rupture front propagation in the region is unresolved.

The discontinuous and heterogeneous rupture propagation that we have observed with jumping of rupture over strong regions and locally supershear rupture can be explained by stress and strength heterogeneity on the fault. Almost every numerical study of spontaneous rupture propagation in which stress and strength heterogeneity are allowed has exhibited similar behavior [*Das and Aki*, 1977; *Day*, 1982*b*, *Boatwright and Quin*, 1986]. Thus we can plausibly ascribe the heterogeneity observed in the rupture process to variations in these parameters. Apparently heterogeneity in fault zone properties plays a major role in governing the accumulation and release of stress in earthquake rupture.

This is not the first time rupture heterogeneity has been observed. We have been able to resolve heterogeneity in the rupture behavior with scale lengths of several kilometers. Numerous studies of teleseismically-recorded great earthquakes [e.g. *Kanamori and Stewart*, 1976; *Lay and Kanamori*, 1981; *Nabelek*, 1984] indicate that rupture heterogeneity persists over much larger scale-lengths. Heterogeneity in the rupture process is also thought to persist to much smaller length scales [*Haskell*, 1966; *Aki*, 1967; *Hanks*, 1979; *Andrews*, 1980, 1981].

There are a number of seismic observations that indicate that heterogeneity is an important aspect of seismic rupture at shorter scale-lengths and that it governs the properties of high-frequency strong ground motion. The lack of observed strong directivity in records of acceleration for most earthquakes indicates that rupture is irregular. The 1980 Livermore, California earthquake is a counter-example [*Boatwright and Boore*, 1982]. The fact that acceleration spectra resemble band-limited, Gaussian, white noise to a good approximation indicates that there is considerable randomness in the earthquake source. Short rise times for the moderate-sized earthquakes that we have studied suggest that the rise time is controlled by

local variations in strength and stress rather than larger scale variations such as the distance to the edge of the rupture zone [*Day*, 1982*a*] or the length of the fault [*Scholz*, 1982].

Geological observations also point to the importance of heterogeneity in earthquake faulting. Upon detailed examination, surface traces of faults are known to have complex multiple-segment geometries [*Tchalenko and Abramaseys*, 1970]. Observations of faults causing rockbursts in mines indicates considerable complexity [*Gay and Ortlepp*, 1974] as well. There is also evidence that supports the complexity of fault surfaces over a wide range of scale-lengths [*Tchalenko*, 1970; *King*, 1983; *Okubo and Aki*, 1987].

Understanding of this heterogeneity is essential to understanding the nature of seismic rupture and its consequences: the behavior of rupture during an earthquake, the prediction of high-frequency ground motion, and possibly to the prediction of earthquakes. For the events we have studied, we have been able to attribute the heterogeneities in the faulting process directly to heterogeneities in the fault zone. At smaller length-scales this direct attribution and even the description of rupture models must be statistical in nature. Studies by *Andrews* [1980, 1981], have developed a framework for the description of earthquake faulting and the dynamics of faulting using a stochastic approach, but much work remains to be done.

APPENDIX A

RAY-THEORY GREEN'S FUNCTIONS USING DYNAMIC RAY TRACING

For the domain in which the scale-length of heterogeneity is much greater than the wavelength, geometric ray theory provides a powerful technique for calculating Green's functions. Ray-theory solutions to the equation of motion can be obtained by expressing the displacement, u, as an asymptotic series in inverse powers of angular frequency, ω

$$u = e^{-i\omega(t-\tau)} \sum_{n=0}^{\infty} U^n(-i\omega)^{-n} \tag{A.1}$$

[*Cerveny et al.*, 1977]. If we retain only the zeroth-order term in (A.1) and let $U = U^0$ then we are left with a solution of the form

$$u = U e^{-i\omega(t-\tau)} \tag{A.2}$$

The scalar Helmholtz equation, which governs the propagation of SH waves in a two-dimensional medium, is

$$\nabla \cdot (\mu \nabla u) + \rho \omega^2 u = 0 \tag{A.3}$$

were μ is the shear modulus and ρ is the density. Substituting the *ansatz* (A.2) into (A.3), retaining only terms of order $(i\omega)^2$ and $(i\omega)$, and requiring that the solution remain independent of frequency we obtain the two equations

$$\nabla\tau \cdot \nabla\tau = \frac{\rho}{\mu} \tag{A.4}$$

and

$$(\nabla\mu\cdot\nabla\tau) + \mu\,(U\nabla^2\tau + 2\nabla U\cdot\nabla\tau) \;=\; 0 \qquad \text{(A.5)}$$

Equation (A.4) is known as the eikonal equation and equation (A.5) is known as the transport equation. Rays are characteristics of the eikonal equation (surfaces of constant τ are wavefronts). The transport equation is used to solve for geometric spreading.

We solve the vector, three-dimensional, elastic versions of equations (A.4) and (A.5) for *P* and *S* waves using the dynamic ray tracing technique [*Popov and Psencik*, 1978]. Dynamic ray tracing is a convenient method for computing ray trajectories, geometric spreading, and *S*-wave torsion needed to calculate ray-theory Green's functions in a three-dimensional, laterally-varying medium. Following *Popov and Psencik* [1978] and *Cerveny and Hron* [1980] we perform the dynamic ray tracing in the ray-centered coordinate system.

The ray-centered coordinate system is an orthogonal, curvilinear coordinate system that follows the ray trajectory and rotates according to the accumulated torsion of the ray. It has the convenient property that the transport equations for the two components of *S* waves are uncoupled at the zeroth-order approximation. This contrasts with the traditional Frénet frame of normal and bi-normal vectors for which the transport equations are coupled even at zeroth order [*Hubral*, 1979].

To perform the dynamic ray tracing we integrate a system of fifteen first-order differential equations along the ray. These include six equations, derived from the eikonal equation, for ray trajectory:

$$\frac{d\mathbf{x}}{d\tau} \;=\; v^2\mathbf{p} \qquad \text{(A.6)}$$

and

$$\frac{d\mathbf{p}}{d\tau} = -\frac{1}{\upsilon}\nabla\upsilon \tag{A.7}$$

where **x** is the position vector, **p** is the slowness vector, τ is the travel-time, and υ is the local *P* or *S*-wave velocity. Equation (A.6) describes the position of the ray, which depends in turn on the slowness vector in (A.7). The accumulated rotation of the vector basis, ϕ, of the ray-centered coordinate system due to *S*-wave torsion is determined by integrating the equation

$$\frac{d\phi}{d\tau} = \frac{p_3}{p_1^2 + p_2^2}\left(p_2\frac{d\upsilon}{dx_1} - p_1\frac{d\upsilon}{dx_2}\right) \tag{A.8}$$

We use the vertical and azimuthal take-off angles, γ_1 and γ_2, as ray parameters to specify the initial trajectory of the ray. The partial derivatives of the slowness with respect to the ray parameters are used to determine the geometric spreading. Following *Cerveny* [1986] we determine the geometric spreading using the **Q** and **P** matrices, which are defined as

$$Q_{ij} = \frac{\partial q_i}{\partial \gamma_j} \tag{A.9}$$

$$P_{ij} = \frac{\partial p_i}{\partial \gamma_j} \tag{A.10}$$

where i and j both range from 1 to 2. The eight differential equations that govern the evolution of **P** and **Q** along the ray are

$$\frac{dQ_{ij}}{d\tau} = \upsilon^2 P_{ij} \tag{A.11}$$

and

$$\frac{dP_{ij}}{d\tau} = -\frac{1}{v}\left(Q_{1j}\frac{\partial^2 v}{\partial q_i \partial q_1} + Q_{2j}\frac{\partial^2 v}{\partial q_i \partial q_2}\right) \tag{A.12}$$

[*Cerveny and Hron*, 1980]. Geometric spreading, S^v, is calculated from the determinant of the **Q** matrix by the relation

$$S^v = \frac{1}{\sqrt{|\mathbf{Q}^v|}} \tag{A.13}$$

We also use the **Q** matrix to solve the two-point ray tracing problem using the paraxial approximation as described in Appendix B.

The fifteen differential equations (A.6, A.7, A.8, A.11, A.12) of the dynamic ray tracing system were integrated numerically using a Runge-Kutta technique. To calculate ray-theory Green's functions using dynamic ray tracing, we follow a parallel development to that of *Spudich and Frazer* [1984] who analyzed the same problem using ray tracing in the Frénet frame.

Let the ray-tangent unit vector be $\hat{\mathbf{e}}_1$ and the orthogonal unit vectors that complete the ray-centered coordinate system be $\hat{\mathbf{e}}_2$ and $\hat{\mathbf{e}}_3$. The high-frequency P-wave response at angular frequency ω and position ξ on the fault plane due to a unit impulse at time $t = 0$ and receiver position $\mathbf{x}$ in the $\hat{\mathbf{a}}$ direction is

$$\mathbf{u}^P(\xi, \omega; \mathbf{x}, 0) = \frac{F^{e_1}\left(\hat{\mathbf{a}} \cdot \hat{\mathbf{e}}_1^o\right) e^{i\omega t^P}}{4\pi\sqrt{\rho_o \rho \alpha_o^3 \alpha}\, S^\alpha}\hat{\mathbf{e}}_1 \tag{A.14}$$

F^{e1} is the free-surface reflection coefficient, α is the compressional wave velocity, and the subscript o denotes the value of a parameter at the observer position $\mathbf{x}$. Denoting the shear wave velocity as β, the equivalent expression for S waves is

$$\mathbf{u}^s\left(\xi,\omega;\,\mathbf{x},\,0\right) = \frac{\left[F^{e2}\left(\hat{\mathbf{a}}\cdot\hat{\mathbf{e}}_2^o\right)\hat{\mathbf{e}}_2 + F^{e3}\left(\hat{\mathbf{a}}\cdot\hat{\mathbf{e}}_3^o\right)\hat{\mathbf{e}}_3\right] e^{i\omega t^S}}{4\pi\sqrt{\rho_o\rho\beta_o^3\beta}\;S^\beta} \tag{A.15}$$

We are free to choose the initial orientation for the unit vectors $\hat{\mathbf{e}}_2$ and $\hat{\mathbf{e}}_3$. It is most convenient to choose them such that $\hat{\mathbf{e}}_2$ corresponds to polarization in the horizontal plane perpendicular to the ray, and $\hat{\mathbf{e}}_3$ corresponds to polarization in the vertical plane perpendicular to the ray, evaluated at the receiver. The free surface reflection coefficients for $\hat{\mathbf{e}}_2$ and $\hat{\mathbf{e}}_3$ are then the *SH* and *SV* reflection coefficients respectively.

The traction $\mathbf{T}$ due to a stress tensor τ at a point on a fault plane with unit normal $\hat{\mathbf{n}}$ in an isotropic medium is

$$\mathbf{T} = \hat{\mathbf{n}}\cdot\tau = \lambda\left(\nabla\cdot\mathbf{u}\right)\hat{\mathbf{n}} + \mu\left(\nabla\mathbf{u} + (\nabla\mathbf{u})^{\mathrm{T}}\right)\cdot\hat{\mathbf{n}} \tag{A.16}$$

where λ and μ are the Lame parameters. If we substitute the displacement field generated by the point force at the receiver considered in equation (A.14) into the general expression for the traction (A.16) and retain only the highest order terms in frequency, then the traction acting across the fault due to compressional waves generated by a unit impulse at the receiver is

$$\mathbf{T}^s\left(\xi,\omega;\,\mathbf{x},\,0\right) = i\omega\,\frac{F^{e1}\left(\hat{\mathbf{a}}\cdot\hat{\mathbf{e}}_1^o\right)\left[\lambda\hat{\mathbf{n}} + 2\mu\left(\hat{\mathbf{e}}_1\cdot\hat{\mathbf{n}}\right)\hat{\mathbf{e}}_1\right]}{4\pi\sqrt{\rho_o\rho\alpha^3\alpha_o^3}\;S^\alpha}\,e^{i\omega t^P} \tag{A.17}$$

Performing the same substitution for S waves we find that the traction on the fault from the same unit impulse is

$$\mathbf{T}^s(\xi,\omega;\mathbf{x},0) = \frac{i\omega\mu\, e^{i\omega t^S}}{4\pi\sqrt{\rho_o\rho\beta^3\beta_o^3}\; S^\beta}\Big\{F^{e_2}(\hat{\mathbf{a}}\cdot\hat{\mathbf{e}}_2^o)\big[(\hat{\mathbf{e}}_1\cdot\hat{\mathbf{n}})\hat{\mathbf{e}}_2 + (\hat{\mathbf{e}}_2\cdot\hat{\mathbf{n}})\hat{\mathbf{e}}_1\big] + F^{e_3}(\hat{\mathbf{a}}\cdot\hat{\mathbf{e}}_3^o)\big[(\hat{\mathbf{e}}_1\cdot\hat{\mathbf{n}})\hat{\mathbf{e}}_3 + (\hat{\mathbf{e}}_3\cdot\hat{\mathbf{n}})\hat{\mathbf{e}}_1\big]\Big\} \tag{A.18}$$

For shear dislocation across a fault we are interested in the special case in which we allow no cavitation across the fault plane. In this case the expression (A.17) for the P wave traction reduces to

$$\mathbf{T}^p(\xi,\omega;\mathbf{x},0) = i\omega\frac{\mu F^{e_1}(\hat{\mathbf{a}}\cdot\hat{\mathbf{e}}_1^o)(\hat{\mathbf{e}}_1\cdot\hat{\mathbf{n}})\hat{\mathbf{e}}_1}{2\pi\sqrt{\rho_o\rho\alpha_o^3\alpha^3}\; S^\alpha}e^{i\omega t^p} \tag{A.19}$$

and the traction from the S waves (A.18) remains the same.

In Chapter 2 we refer to the quantities $\mathbf{H}_a^p$ and $\mathbf{H}_a^s$, which are defined for the case of no cavitation as

$$\mathbf{H}_a^p(\xi,\omega;\mathbf{x},0) = \frac{\mu F^{e_1}(\hat{\mathbf{a}}\cdot\hat{\mathbf{e}}_1^o)(\hat{\mathbf{e}}_1\cdot\hat{\mathbf{n}})\hat{\mathbf{e}}_1}{2\pi\sqrt{\rho_o\rho\alpha_o^3\alpha^3}\; S^\alpha} \tag{A.20}$$

and

$$\mathbf{H}_a^s(\xi,\omega;\mathbf{x},0) = \frac{\big\{F^{e_2}(\hat{\mathbf{a}}\cdot\hat{\mathbf{e}}_2^o)\big[(\hat{\mathbf{e}}_1\cdot\hat{\mathbf{n}})\hat{\mathbf{e}}_2 + (\hat{\mathbf{e}}_2\cdot\hat{\mathbf{n}})\hat{\mathbf{e}}_1\big] + F^{e_3}(\hat{\mathbf{a}}\cdot\hat{\mathbf{e}}_3^o)\big[(\hat{\mathbf{e}}_1\cdot\hat{\mathbf{n}})\hat{\mathbf{e}}_3 + (\hat{\mathbf{e}}_3\cdot\hat{\mathbf{n}})\hat{\mathbf{e}}_1\big]\big\}}{4\pi\sqrt{\rho_o\rho\beta^3\beta_o^3}\; S^\beta} \tag{A.21}$$

The validity of the ray-theory approximation described here is discussed in general in Chapter 2, and more specifically for individual earthquakes and crustal structures in Chapters 4-6. *Cerveny et al.* [1987] have used Gaussian beams to obtain analogous expressions for (A.20) and (A.21).

APPENDIX B

MODELING EARTHQUAKE SOURCES IN LATERALLY-VARYING STRUCTURE – THE EFFECT OF A FAULT ZONE

The high-frequency, near-source approximation that we use enables us to calculate theoretical seismograms in a three-dimensionally varying medium using ray theory (Appendix A). The effects of lateral heterogeneity were not included when modeling earthquake sources because the three-dimensional structure of the crust is not known in sufficient detail in the source regions studied. In this chapter we consider the effects of a simple model of a low velocity zone surrounding a fault. The model is based on several studies that indicate a shallow, wedge-shaped zone of low velocity centered on earthquake faults in California. For certain source-receiver geometries, the effects of lateral heterogeneity are quite strong. These effects may explain some observations of strong ground motion not easily explained in a laterally-homogeneous velocity model.

Paraxial Ray Tracing

In order to use (2.17) to calculate seismograms, it is necessary to evaluate the Green's function on the fault. To do this using ray theory we must solve the two-point ray tracing problem–to trace rays from each receiver to a grid of points on the fault. We have used iterative paraxial ray tracing to accomplish this task. Iterative paraxial ray tracing amounts to using the elements of the **Q** matrix of dynamic ray tracing (Appendix A) to solve the two-point ray tracing problem.

We begin with an initial guess of the ray parameters γ that specify the initial ray trajectory at the source. We then calculate a misfit vector between the ray endpoint and the desired endpoint on the fault plane. The misfit vector, **f**, between the actual and desired ray

endpoints is projected onto the wavefront, which amounts to transforming **f** from a cartesian frame to the ray-centered coordinate frame. The projected misfit vector is then used to update the current estimate of the ray parameter γ^{n-1} based on our knowledge of the local curvature of the wavefront, i.e.,

$$\begin{pmatrix} \gamma_1^n \\ \gamma_2^n \end{pmatrix} = \begin{pmatrix} \gamma_1^{n-1} \\ \gamma_2^{n-1} \end{pmatrix} + \mathbf{Q}^{-1} \begin{pmatrix} f_1^{n-1} \\ f_2^{n-1} \end{pmatrix} \tag{B.1}$$

Equation (B.1) is used iteratively to estimate the ray parameters, γ^n, of the desired ray. Paraxial ray tracing provides an efficient and practical alternative to shooting and bending methods, particularly in three-dimensionally varying media. For the cases we have studied, convergence to a misfit of less than 10 m for a pathlength of 10 km was obtained after only a few iterations.

Three Dimensional Structure Near a Fault Zone

To demonstrate the application of this technique, we examine the effects due to an idealized model of a fault zone. Evidence of three-dimensionally varying structure in the vicinity of fault zones has been found in several different types of studies. For example, in central California the existence of a low velocity zone extending below the surface trace of the Calaveras and San Andreas faults has been inferred from earthquake arrival time residuals [*Mayer-Rosa*, 1973; *Thurber*, 1983], refraction profiles [*Mooney and Luetgert*, 1982; *Blümling et al.*, 1985], reflection sections [*Feng and McEvilly*, 1983], and waveform modeling of aftershocks [*Cormier and Spudich*, 1984].

Evidence for three-dimensionally varying structure can also be found in strong-motion data. *Tucker and King* [1984] have documented strong effects of sediment filled valleys on the amplitude spectra for earthquakes recorded in the Garm region of the USSR. The variations of amplitude across the El Centro array, particularly the large amplitudes at station

6, in the 1979 Imperial Valley earthquake have been attributed by some authors [*Singh* 1981; *Rial et al.*, 1986] to lateral variations in the local velocity structure. *Vidale and Helmberger* [1988] have obtained a better fit to recordings of the 1971 San Fernando earthquake by calculating finite-difference seismograms for a laterally-varying structure.

Since the true velocity structure in the vicinity of the Calaveras and San Andreas faults is not well determined, we use a simple representative velocity anomaly to demonstrate the type and magnitude of the effects to be expected. The example is based on the laterally-homogeneous model of *Blümling et al.* [1985] for the vicinity of the Calaveras Fault. The *Blümling et al.* [1985] velocity structure, $v_0(z)$, is perturbed with a velocity anomaly that decays exponentially with distance from the fault, y, and with depth, z. The perturbation has the form

$$v(y,z) = v_0(z)\left[1 - Ce^{-(y/w)^2 - z/d} \right] \qquad \text{(B.2)}$$

where w is the width of the fault zone, d is the depth, and C is a constant that scales the strength of the perturbation. The parameters chosen to approximate the wedge-shaped fault zone anomaly of *Feng and McEvilly* [1985] are $w = 2$ km, $d = 10$ km, and $C = 0.4$ km. The resulting velocity structure is shown in figure B.1. S-wave velocities are calculated by assuming a Poisson solid.

Because an analytical perturbation (B.2) is applied to the velocity anomaly it is a simple matter to calculate the first and second partial derivatives of velocity that are needed for dynamic ray tracing. Although the velocity structure does not vary with x, the problem is three dimensional since rays from different locations on the fault have markedly different trajectories to the receiver. It is worth mentioning here that the simple structure was chosen for convenience only, the method is valid for a general laterally-varying structure provided the medium is sufficiently smooth that ray theory is applicable [*Beydoun and Ben-Menahem*,

1985; *White et al.*, 1987]. An example of an iterative sequence of rays based on the paraxial method in equation (B.1) is shown in Figure B.2.

Figure B.3 shows an example of the effect of the assumed structure on rays emanating from a 5 km deep point source. The azimuthal distribution of rays spans the axis of the fault zone. Also shown are the velocity seismograms for the 1984 Morgan Hill earthquake recorded by stations G06 and G07 of the Gilroy array [*Shakal et al.*, 1984]. The location of the point source is shallower than most of the faulting during the earthquake, but coincides with the location of a region of high slip centered near 8 km depth (Chapter 4).

Although the two stations are less than 4 km apart, they have dramatically different waveforms. Peak velocities at G06 are about 5 times larger than those at G07. Since both stations are located on similar "hard-rock" sites, the effect is not likely to be a local site effect. Also the stations are too close to one another to ascribe the difference to directivity alone [*Hartzell and Heaton*, 1986]. The effects of a low velocity zone centered on the fault may be responsible for the large difference between the two stations. Figure B.3 suggests that waves at G06 may be focussed and waves at G07 may be in a shadow zone for the 5 km deep point source.

Many of the rays in figure B.3 touch caustic surfaces that occur in the regions of strong lateral velocity gradients. Due to the symmetry of the idealized fault zone the caustics periodically collapse to focal points. Since the iterative ray tracing method fails at caustics, as does our method for calculating geometric spreading, the examples we have chosen to demonstrate the method are restricted to stations outside the fault zone, removed from caustic surfaces. Even for stations outside the fault zone there can be substantial effects on the ground motion.

The Effect on Theoretical Seismograms

We have calculated theoretical seismograms for the structure described above. The locations of the receivers and the fault geometry are shown in figure B.4. The receivers are

placed at 1-km intervals at the free surface from 3 to 7 km from the fault. The three vertical subfaults considered are 1 km in diameter, centered at a depth of 4.5 km, at a distance of 0.5, 2.5, and 4.5 km along the strike of the fault. Slip on each of the subfaults is assumed to be a uniform 10 cm of right-lateral strike-slip. Rupture propagates radially at a velocity of 2 km/s with a uniform rise time of 0.2 s. The source description is purely kinematic. The only purpose is to demonstrate the effects of laterally varying structure on the ground motion.

A surface projection of rays shot from each subfault to the receiver is shown in figure B.5. for the laterally-homogenous and laterally-inhomogeneous cases. For the unperturbed medium the rays are straight lines–there is no horizontal variation in velocity to refract them. For the perturbed medium the ray paths are strongly affected. In the perturbed case rays leave the source region more nearly perpendicular to the fault normal because the minimum time path is one that leaves the low-velocity zone fairly directly. Because the rays are bent they arrive at the receiver with different trajectories. The also emanate from the source with a different orientation and consequently a different excitation. Other than the delay in arrival time, these are the primary differences in high-frequency wave propagation for the two structures. These effects are demonstrated by comparing theoretical seismograms calculated with the two different models.

Figures B.6-B.8 show the seismograms for the subfaults that are 0.5, 2.5, and 4.5 km along strike from the observer. For this geometry the rays depart on a lobe of the SH radiation pattern. The SH radiation appears primarily on the x (parallel to the fault) component of motion. The polarity of the y component is different for the two velocity models for the receivers closest to the fault. This is due to the trajectory of the ray at the receiver (Figure B.4). For the receivers close to the fault the SV contribution is stronger than the SH contribution for the laterally-inhomogeneous case, but not for the laterally homogeneous case. In the laterally-heterogeneous case, and for receivers farther from the fault, SH dominates SV. Since for this geometry SH and SV have opposite signs, the polarity of the S-wave arrival at the receiver is reversed. Figure B.8 demonstrates the effect

for the subfault 2.5 km along strike. For the receiver at 4.5 km, the *SV* contribution is less than the *SH* contribution for the laterally-varying case, but for the laterally-homogeneous case it is not, and the polarity in the two cases is opposite. For the receiver 7 km from the fault, the *SV* contribution is larger for both cases and the polarity is the same.

Another feature common to the comparisons in Figures B.6-B.8 is that the contribution of the *P* wave relative to the *S* wave is usually greater in the inhomogeneous case. This can be explained in part by the relative excitation of the *P* and *S* waves in the two models. The components of the *S* waves have a larger component parallel to the fault normal in the laterally homogeneous case, thus by equation (A.22) they are more strongly excited for shear dislocations. The same effect causes the *P* waves, for which the particle motion is tangential to the ray, to have a larger component parallel to the fault normal and by equation (A.21) they are more strongly excited in the laterally inhomogeneous case.

The use of ray theory in the high-frequency, near-source approximation allows us to incorporate the effects of smooth, laterally-varying structure on earthquake strong ground motion. If the three-dimensional structure of an area were well known, this would be a preferred method for calculating seismograms. We have demonstrated some interesting effects due to lateral velocity variations in a simplified model of fault-zone structure. These type of effects may explain much of the residual misfit to the data in our modeling the rupture histories of earthquakes in Chapter 4. In the future, when Earth structure in the near-source region is better known, we may be able to usefully apply the fully three-dimensional ray theory seismograms demonstrated in this appendix to the problems treated in the previous chapters to better image earthquake sources.

Figure Captions

Figure B.1 Lines of equal shear wave velocity are shown for the laterally-varying structure used in this study. The contour interval is 0.5 km/s. The laterally homogeneous structure (away from the fault) is the smoothed version of the *Blümling et al.*[1985] structure used in the analysis of the Morgan Hill earthquake in Chapter 4. The laterally-homogeneous structure is perturbed according to equation (B.2). This perturbation approximately models the low velocity zone found by *Feng and McEvilly* [1983].

Figure B.2 A sequence of paraxially-traced rays is shown for the laterally-varying medium from the receiver (triangle) to the fault plane. The target point is at the center of the circle. The initial guess based on a laterally-homogeneous assumption misses the target by several km, but subsequent estimates of the ray parameter quickly converge to the ray connecting the source and receiver.

Figure B.3 A fan of rays shot for a 5 km deep source in the structure shown in Figure B.1. The take-off angle has been kept constant and the azimuth varied to span the width of the fault zone. Also shown are velocity records from the 1984 Morgan Hill, California earthquake (Chapter 4). The variations in amplitude at the stations G06 and G07 may be related to their location inside or out of the fault zone.

Figure B.4 The set of 5 receivers (triangles) that range from 3 to 7 km from the fault are shown in perspective with the subfaults (circles), which are vertical, circular, and located 0.5, 2.5, and 4.5 km along-strike. The coordinate system is shown with x parallel to the fault zone, z, positive downward, and y forming a right-handed system. Rays from the receiver at $y = 3$ km to the first subfault at $x =$ 0.5 km are shown for the laterally-homogeneous and laterally-heterogeneous cases. The lower ray, which is more strongly bent, is traced through the laterally-heterogeneous structure.

Figure B.5 A map view is shown of the rays connecting the receiver at 3 km with the center of each subfault. The straight, solid lines are the rays for the laterally-homogeneous case and the curved, dashed lines are the rays for that laterally-heterogeneous case.

Figure B.6 Theoretical velocity seismograms for the laterally-homogeneous model (solid lines) and for the laterally-heterogeneous model (dashed lines) are compared for the x, y, and z, components of motion for the subfault 0.5 km along-strike. The seismograms are for receivers ranging from $y = 3$ km (bottom) to $y = 7$ km (top) from the fault. The peak amplitude of the largest of the two traces is shown in units of $cm/s^2 \times 10^{-3}$.

Figure B.7 Same as Figure B.6 for the subfault 2.5 km along-strike.

Figure B.8 Same as Figure B.6 for the subfault 4.5 km along-strike.

Figure B.9 The velocity seismograms for the y component of motion radiated by the subfault at 2.5 km observed at receivers at $y = 3$ and $y = 7$ km are shown. The seismograms are decomposed into local *SH* and *P-SV* at the receiver. Solid lines indicate seismograms calculated in the laterally-homogeneous structure and dashed lines indicate seismograms calculated in the laterally-heterogeneous structure. The difference in polarity of the *S* waves at 4 km, but not at 7 km, us due to the relatively large contribution of *SV* to this component of motion for the receiver at 4 km in the laterally homogeneous case. For this geometry *SH* and *SV* have opposite polarities.

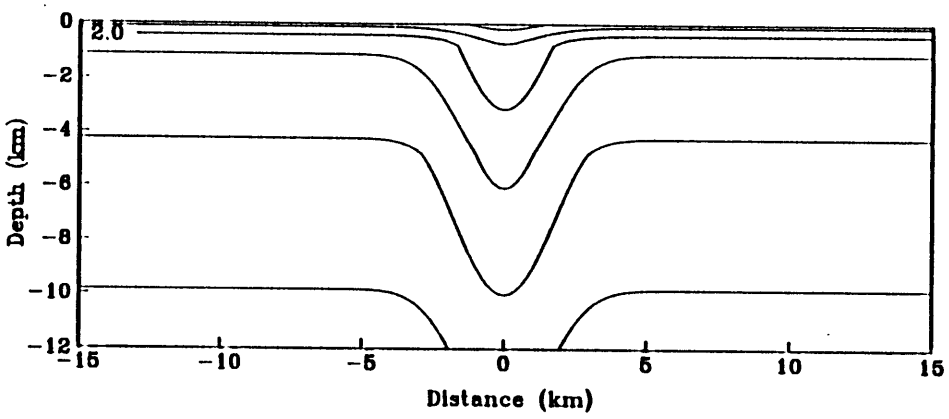

Figure B.1

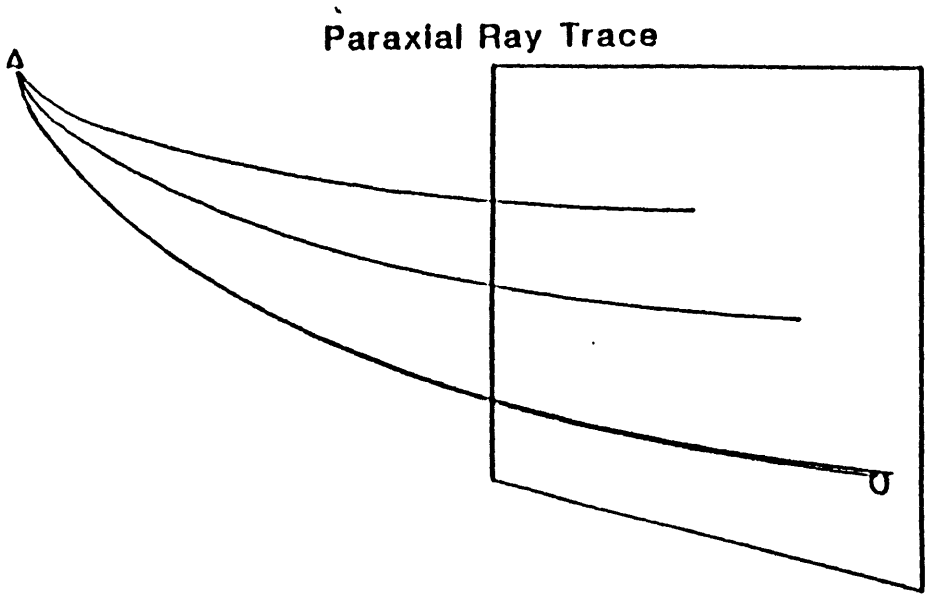

Figure B.2

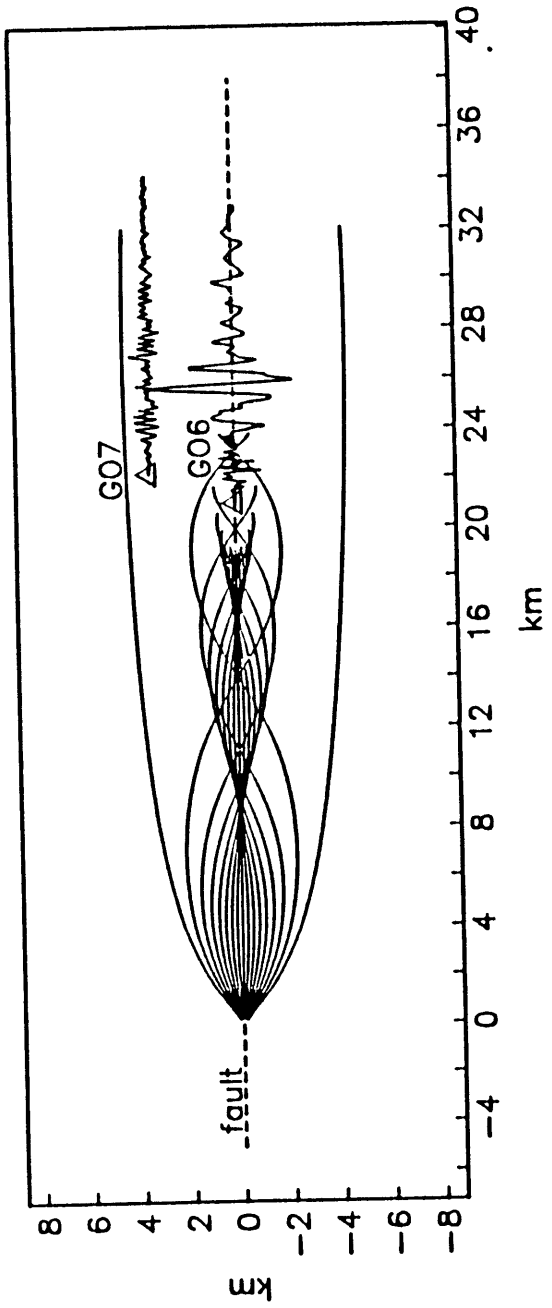

Figure B.3

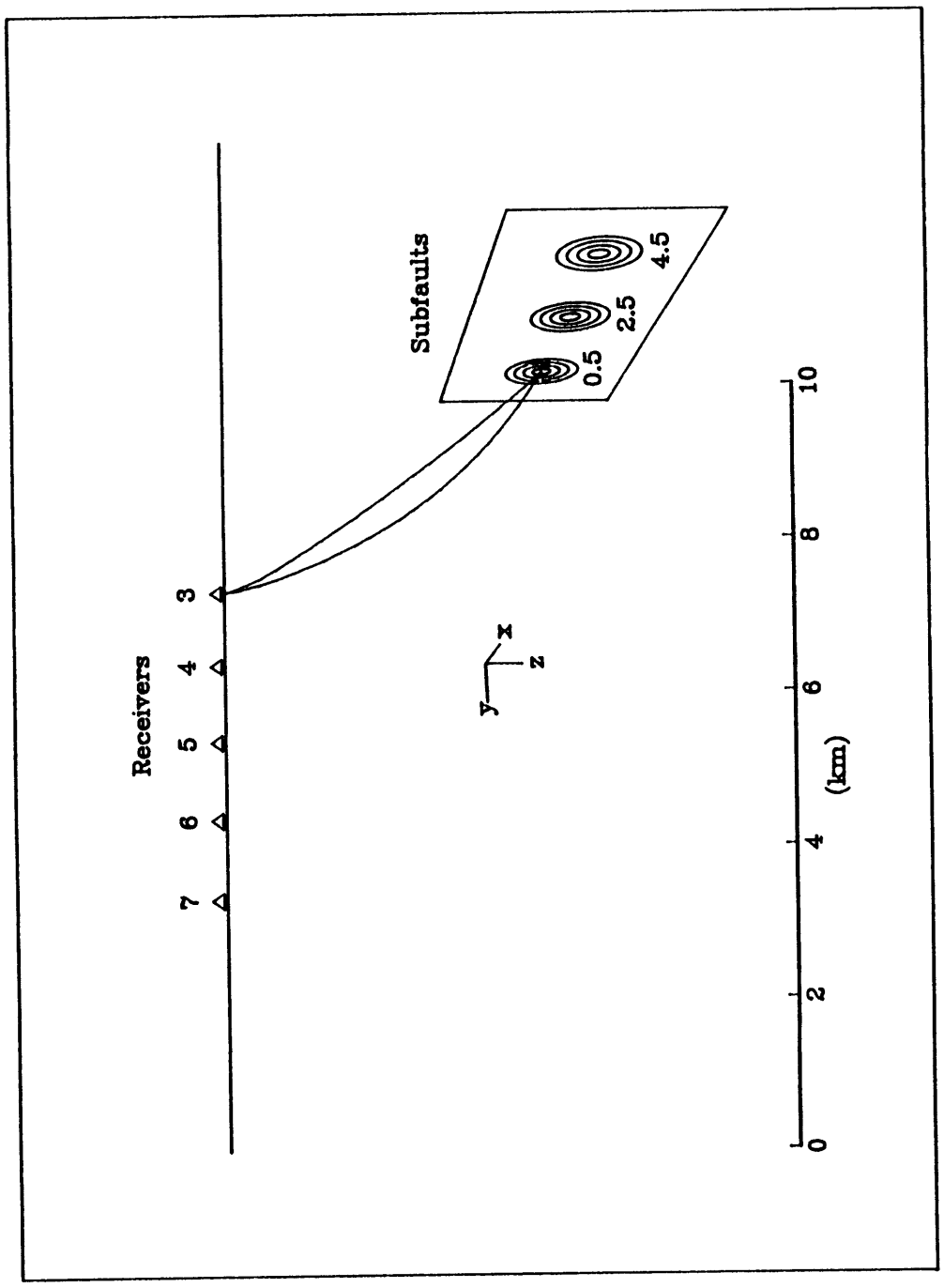

Figure B.4

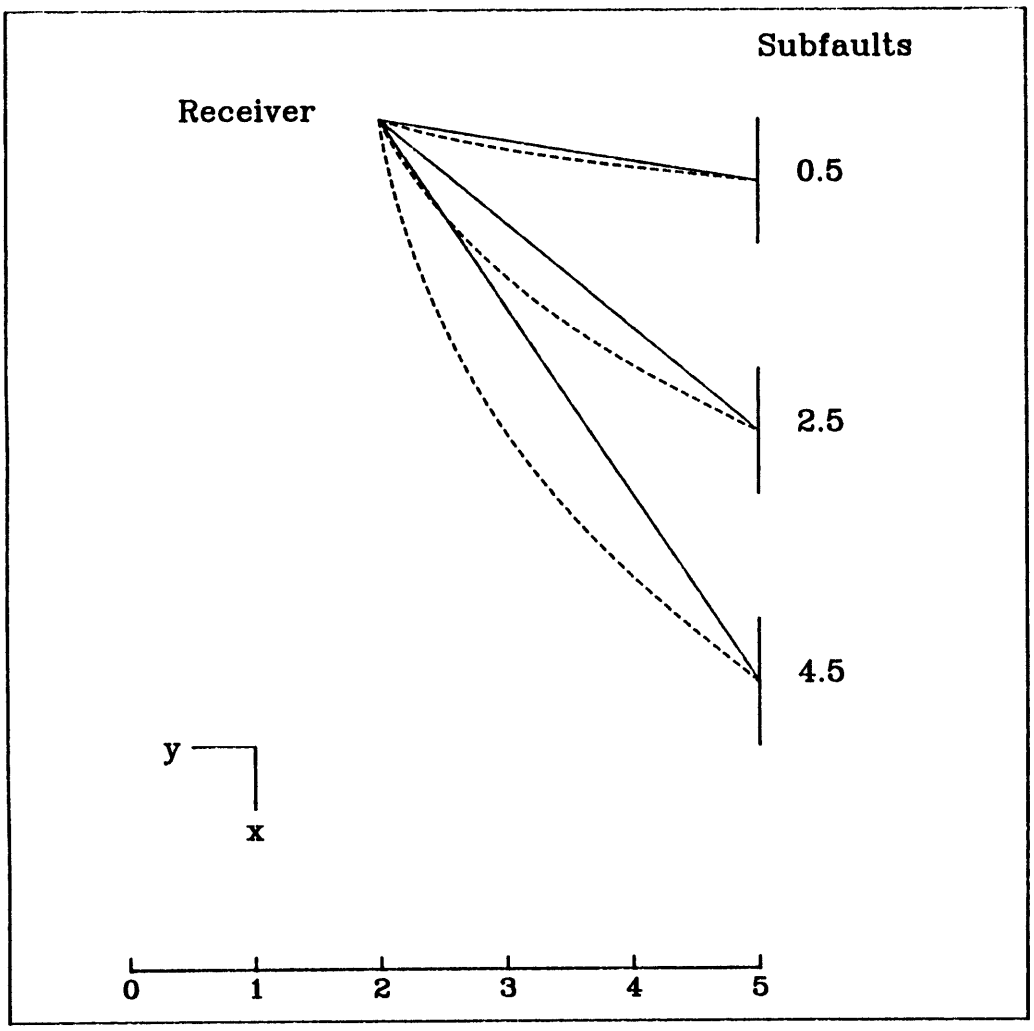

Figure B.5

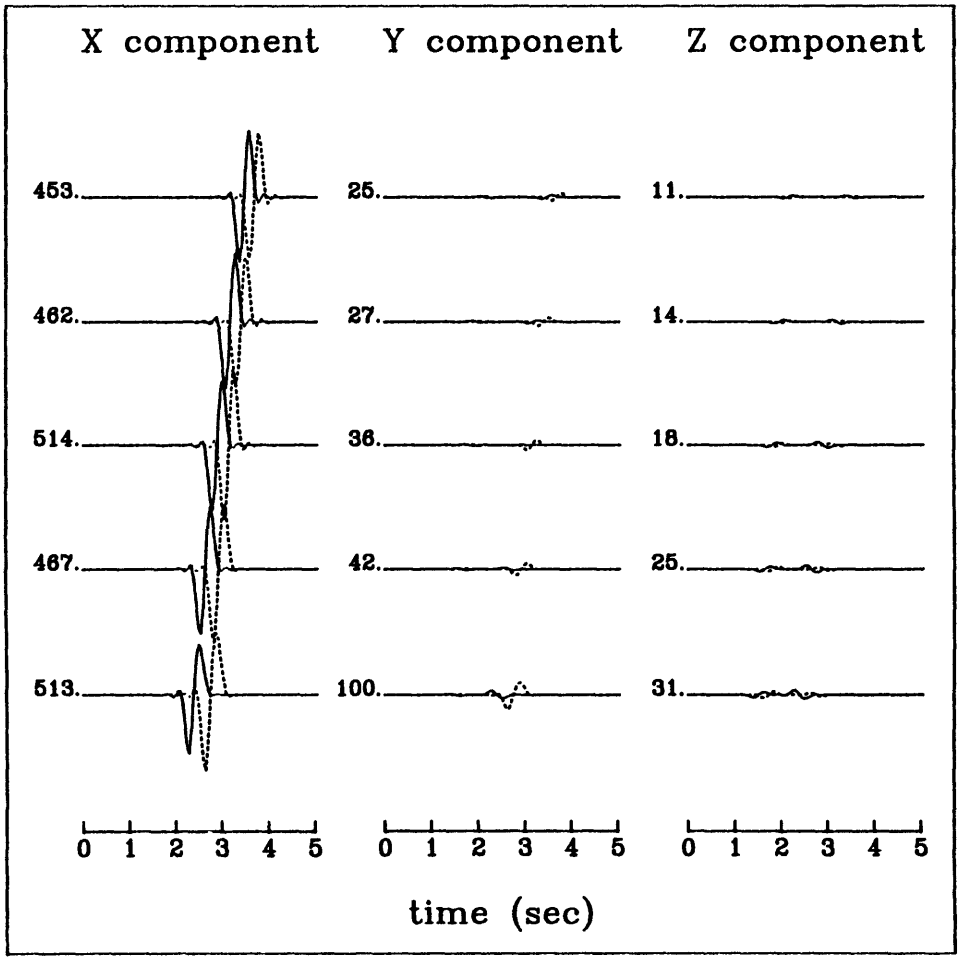
X component
Y component
Z component
453.
462.
514.
467.
513.
25.
27.
36.
42.
100.
11.
14.
18.
25.
31.
0 1 2 3 4 5
0 1 2 3 4 5
0 1 2 3 4 5
time (sec)

Figure B.6

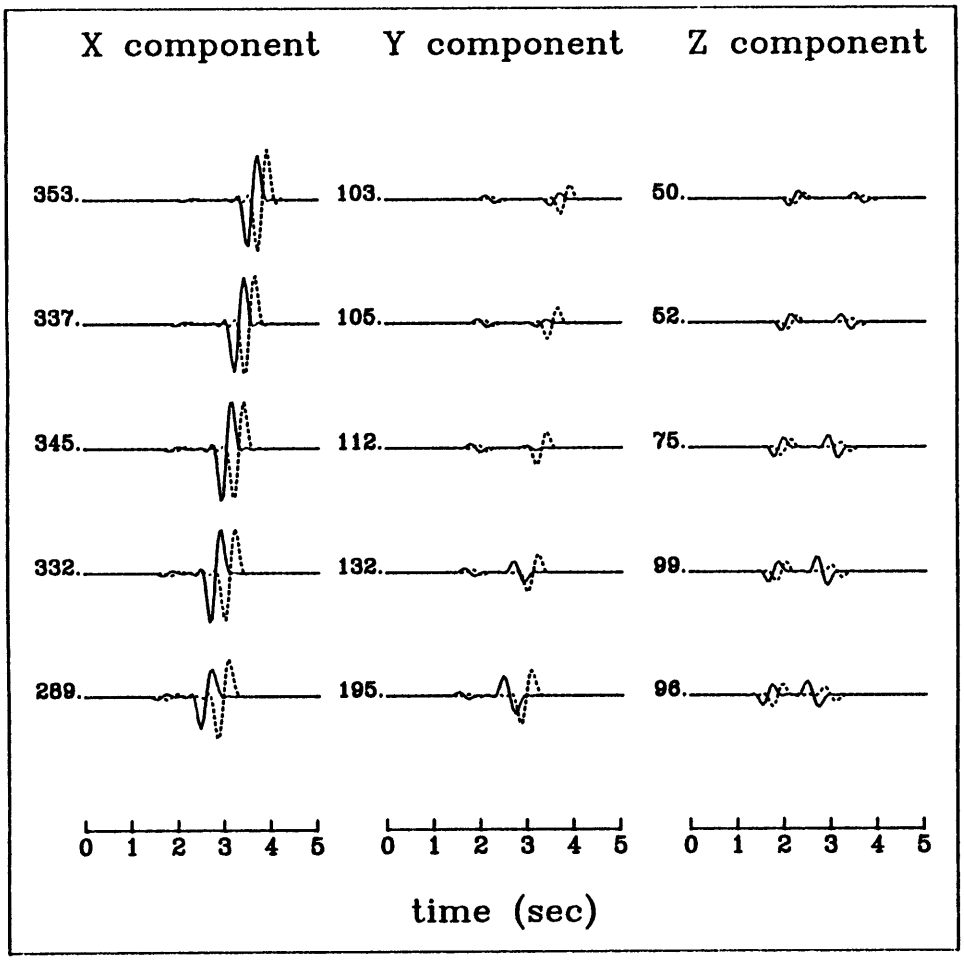
X component
Y component
Z component
353.
103.
50.
337.
105.
52.
345.
112.
75.
332.
132.
99.
289.
195.
96.
0 1 2 3 4 5
0 1 2 3 4 5
0 1 2 3 4 5
time (sec)

Figure B.7

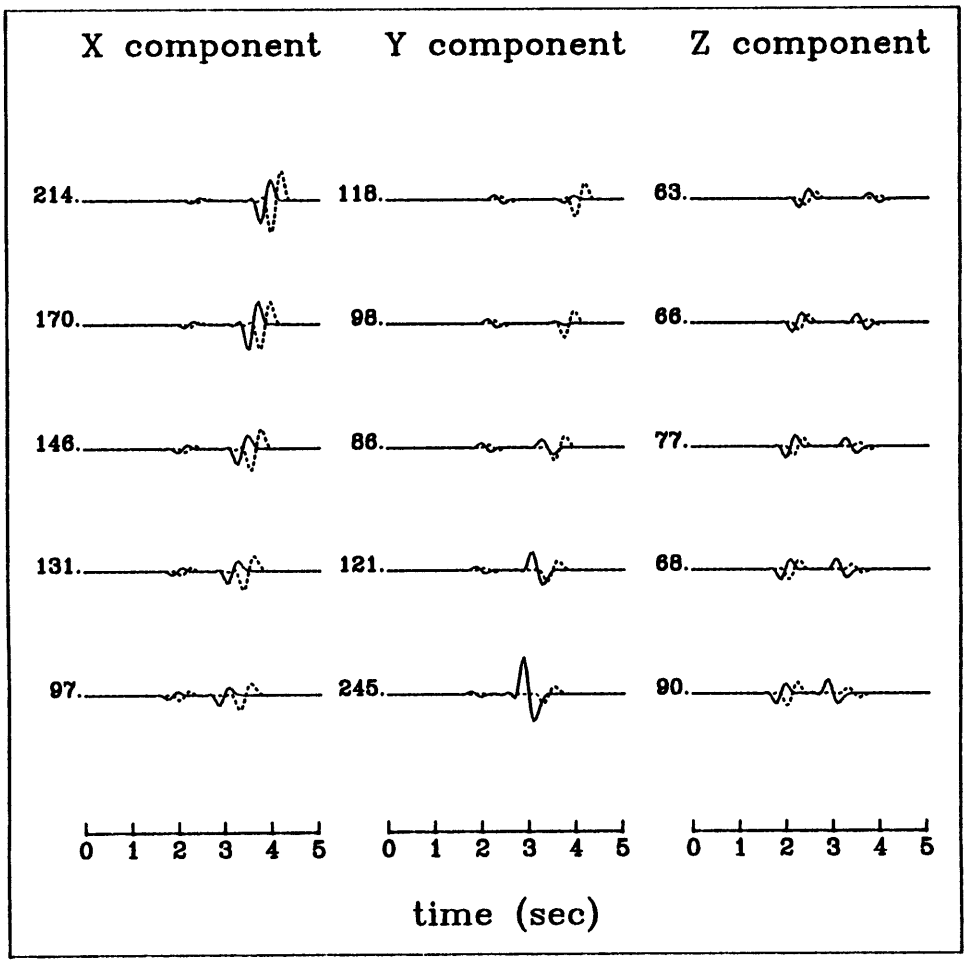
X component
Y component
Z component
214.
118.
63.
170.
98.
66.
146.
86.
77.
131.
121.
68.
97.
245.
90.
0 1 2 3 4 5
0 1 2 3 4 5
0 1 2 3 4 5
time (sec)

Figure B.8

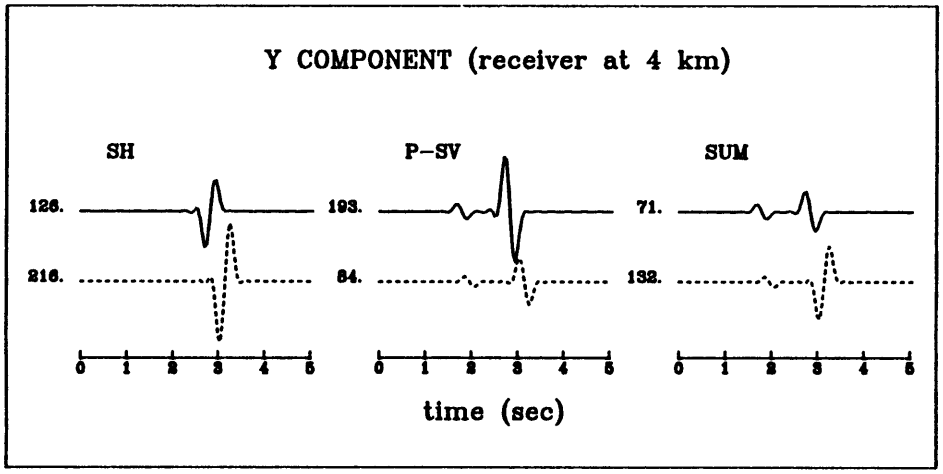
Y COMPONENT (receiver at 4 km)
SH
P-SV
SUM
126.
216.
193.
84.
71.
132.
0 1 2 3 4 5
time (sec)

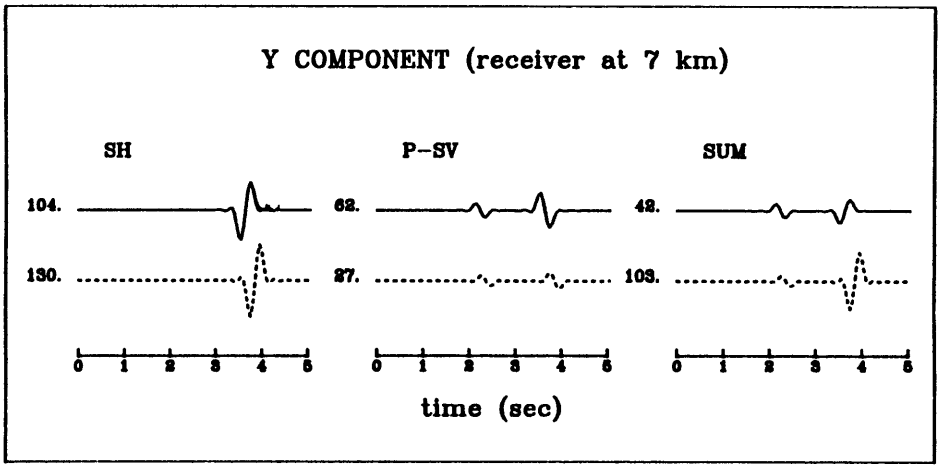
Y COMPONENT (receiver at 7 km)
SH
P-SV
SUM
104.
130.
62.
27.
42.
103.
0 1 2 3 4 5
time (sec)

Figure B.9

REFERENCES

Abrahamson, N. A., and R. B. Darragh, Observation of a double event at regional distances: The Morgan Hill earthquake of 24 April 1984, *Bull. Seismol. Soc. Am., 75*, 1461-1464, 1985.

Aki, K., Seismic displacements near a fault, *J. Geophys. Res., 73,* 5359-5376, 1968.

Aki, K., Characterization of barriers on an earthquake fault, *J. Geophys. Res., 84,* 6140-6148, 1979.

Aki, K., Strong motion prediction using mathematical modeling techniques, *Bull. Seismol. Soc. Am., 72,* 529-541, 1982.

Aki, K., and P. G. Richards, *Quantitative Seismology: Theory and Methods, vol. 1*, W. H. Freeman, New York, 1980a.

Aki, K., and P. G. Richards, *Quantitative Seismology: Theory and Methods, vol. 2*, W. H. Freeman, New York, 1980b.

Anderson, J. G., A dislocation model for the Parkfield earthquake, *Bull. Seismol. Soc. Am., 64*, 671-686, 1974.

Anderson, J. and S. E. Hough, A model for the shape of the Fourier amplitude spectrum of acceleration at high frequencies, *Bull. Seismol. Soc Am., 74*, 1969-1993, 1984.

Andrews, D. J., Evaluation of static stress on a fault plane from a Green's function, *Bull. Seismol. Soc. Am., 64*, 1629-1633, 1974.

Andrews, D. J., Rupture velocity of plane-strain shear cracks, *J. Geophys. Res., 81*, 5679-5687, 1976.

Andrews, D. J., A stochastic fault model 1. static case, *J. Geophys. Res., 85*, 3867-3877, 1980.

Andrews, D. J., A stochastic fault model 2. time-dependent case, *J. Geophys. Res., 86*, 10821-10834, 1981.

Archuleta, R. J., Hypocenter for the 1979 Imperial Valley earthquake, *Geophys Res. Lett., 9*, 625-628, 1982*a*.

Archuleta, R. J., Analysis of near-source static and dynamic measurements from the 1979 Imperial Valley earthquake, *Bull. Seismol. Soc. Am., 72*, 1927-1956, 1982*b*.

Archuleta, R. J., A faulting model for the 1979 Imperial Valley earthquake, *J. Geophys. Res., 89*, 4559-4585, 1984.

Archuleta, R. J., E. Cranswick, C. Mueller, and E. Cranswick, Source parameters of the 1980 Mammoth Lakes, California earthquake sequence, *J. Geophys. Res., 87*, 4595-4608, 1982.

Archuleta, R. J., and S. H. Hartzell, Effects of fault finiteness on near-source ground motion, *Bull. Seismol. Soc. Am., 71*, 939-957, 1981.

Archuleta, R. J., and S. M. Day, Dynamic rupture in a layered medium: the 1966 Parkfield earthquake, *Bull.Seismol. Soc. Am., 70*, 671-689, 1980.

Archuleta, R. J., P. Spudich, and A. Olson, Synthetic seismogram studies of an aftershock of the 1979 Imperial Valley, California earthquake, *Seismol. Soc Am. Earthquake Notes, 50*, 50, 1979.

Backus, G. and M. Mulcahy, Moment tensors and other phenomenological descriptions of earthquake sources, I, continuous displacements, *Geophys. J. Roy. Astron. Soc., 46*, 341-361, 1976a.

Backus, G. and M. Mulcahy, Moment tensors and other phenomenological descriptions of earthquake sources, II, discontinuous displacements, *Geophys. J. Roy. Astron. Soc., 46*, 301-329.

Bakun, W. H., Seismic activity on the southern Calaveras fault in central California, *Bull. Seismol. Soc. Am., 70*, 1181-1197, 1980.

Bakun, W. H., M. M. Clark, R. S. Cockerham, W. L. Ellsworth, A. G. Lindh, W. H. Prescott, A. F. Shakal, and P. Spudich, The 1984 Morgan Hill, California, earthquake, *Science, 225*, 288-291, 1984.

Bakun, W. H., and A. G. Lindh, The Parkfield, California earthquake experiment, *Science, 229,* 619-624, 1985.

Bakun, W. H., and T. V. McEvilly, Recurrence models and Parkfield, California, earthquakes, *J. Geophys. Res., 89*, 3051-3058, 1984.

Barenblatt, G. I., The formation of equilibrium cracks during brittle fracture, general ideas and hypotheses, axially symmetric cracks, *Appl. Math. Mech., 23,* 622-636, 1959.

Bernard, P., and R. Madariaga, A new asymptotic method for the modeling of near-field accelerograms, *Bull. Seismol. Soc. Am., 74*, 539-557, 1984.

Beydoun, W. and A. Ben-Menahem, Range of validity of seismic ray and beam methods in general inhomogeneous media I. general theory, *Geophys. J. Roy. Astron. Soc. , 82*, 207-234, 1985.

Bilham, R., R. Yeats, and S. Zerbini, Space geodesy and the global forecast of earthquakes, *EOS,* 65-73, 1989.

Blümling, P., W. D. Mooney, and W.H.K. Lee, Crustal structure of the southern Calaveras fault zone, central California, from seismic refraction investigations, *Bull. Seismol. Soc. Am., 75*, 193-209, 1985.

Boatwright, J., A spectral theory for circular seismic sources; simple estimates of source dimension, dynamic stress drop, and radiated energy, *Bull. Seismol. Soc. Am., 70*, 1-27, 1980.

Boatwright, J., and D. M. Boore, Analysis of ground accelerations radiated by the 1980 Livermore Valley earthquakes for directivity and dynamic source characteristics, *Bull. Seismol. Soc. Am., 72*, 1843-1865, 1982.

Boatwright, J., and H. Quin, The seismic radiation from a 3-D dynamic model of a complex rupture process, part I Confined ruptures, in *Earthquake Source Mechanics, Geophys. Monogr. Ser., vol. 37*, edited by S. Das, J. Boatwright, C. Scholz, pp. 97-109, AGU, Washington, D.C., 1986.

Bouchon, M., Predictability of ground displacement and velocity near an earthquake fault: an example: the Parkfield earthquake of 1966, *J. Geophys. Res., 84*, 6149-6156, 1979.

Bouchon, M., A dynamic source model for the San Fernando earthquake, *Bull. Seismol. Soc. Am., 68,* 1555-1576, 1978.

Brace, W. F., and J. B. Walsh, Some direct measurements of the surface energy of quartz and orthoclase, *Amer. Mineralogist, 47*, 1111-1122, 1962.

Brady, A. G., V. Perez, and P. N. Mork, Digitization and processing of mainshock ground-motion data from the U.S. Geological Survey accelerograph network, The Imperial Valley, California, Earthquake, October 15, 1979, *U.S. Geological Survey Prof. Pap., 1254*, 377-384, 1982.

Brady, A. G., R. L. Porcella, G. N. Bycroft, E. C. Etheredge, P. N. Mork, B. Silverstein, and A. F. Shakal, The Morgan Hill, California earthquake of April 24, 1984, *U.S. Geol. Surv. Open File Report, 84-498B*, 1984.

Brune, J. N., F. L. Vernon III, R. S. Simons, J. Prince, and E. Mena, Strong-motion data recorded in Mexico during the mainshock, The Imperial Valley, California, Earthquake, October 15, 1979, *U.S. Geological Survey Prof. Pap., 1254*, 319-350, 1982.

Burridge, R., The reflection of a pulse in a solid sphere, *Proc. Roy. Soc. A., 276*, 367-400, 1963.

Burridge, R., Admissable speeds for plane-strain self-similar shear cracks with friction, but lacking cohesion, *Geophys. J. Roy. Astron. Soc., 35*, 439-455, 1973.

Burridge, R., and L. Knopoff, Body force equivalent for seismic dislocations, *Proc. R. Soc. London, Ser. A, 54*, 1875-1888, 1964.

Campillo, M. and M. Bouchon, A theoretical study of radiation of small strike-slip earthquakes at close distances, *Bull. Seismol. Soc. Am., 73*, 83-96, 1983.

Cerveny, V., The application of ray tracing to the propagation of shear waves in complex media, in *Seismic Exploration*, S. Treitel and K. Helbig editors, Geophysical Press, London, 1985.

Cerveny, V. and F. Hron, The ray-series method and dynamic ray tracing systems for three-dimensional inhomogeneous media, *Bull. Seismol. Soc. Am., 70,* 47-77, 1980.

Cerveny, V., I. A. Molotkov, and I. Psencik, *Ray Method in Seismology*, Karlova Univerzita, Prague, 1977.

Cerveny, V., J. Pleinerova, L. Klimes, and I. Psencik, High-frequency radiation from earthquake sources in laterally varying structures, *Geophys. J. R. Astron. Soc., 88*, 43-79, 1987.

Choy, G. L., and J. Boatwright, The rupture characteristics of two deep earthquakes inferred from broadband GDSN data, *Bull. Seismol. Soc. Am., 71*, 691-711, 1981.

Cockerham, R. S., and J. P. Eaton, The earthquake and its aftershocks, April 24 through September 30, 1984, *U.S. Geol. Surv. Bull., The Morgan Hill, California, Earthquake of April 24, 1984, USGS Bull., 1639*, 15-28, 1987.

Constable, S. C., R. L. Parker, and C. G. Constable, Occam's inversion: A practical algorithm for generating smooth models from electromagnetic sounding data, *Geophysics*, 52, 289-300, 1987.

Cormier, V. F., and P. Spudich, Amplification of ground motion and waveform complexity in fault zones: Examples from the San Andreas and Calaveras faults, *Geophys. J. R. Astron. Soc., 79*, 135-152, 1984.

Cormier, V. F., and G. C. Beroza, Calculation of strong ground motion due to an extended earthquake source in a laterally varying structure, *Bull. Seismol. Soc. Am., 77*, 1-13, 1987.

Das, S., A numerical study of rupture propagation and earthquake source mechanisms, Sc. D. thesis, Mass. Inst. of Technol., Cambridge, 1976.

Das, S., and K. Aki, Fault plane with barriers: A versatile earthquake model, *J. Geophys. Res., 82*, 5658-5670, 1977.

Das, S., and B. V. Kostrov, Breaking of a single asperity: Rupture process and seismic radiation, *J. Geophys. Res., 88*, 4277-4288, 1983.

Day, S. M., Three-dimensional finite difference simulation of fault dynamics, *Final Rep. SSS-R-80-4295*, S-Cubed, La Jolla, Calif., 1979.

Day, S. M., Three-dimensional finite difference simulation of fault dynamics: Rectangular faults with fixed rupture velocity, *Bull. Seismol. Soc. Am., 72*, 705-727, 1982a.

Day, S. M., Three-dimensional simulation of spontaneous rupture: The effect of nonuniform prestress, *Bull. Seismol. Soc. Am., 72*, 1881-1902, 1982b.

Dines, K. A., and R. J. Lytle, Computerized geophysical tomography, *Proc. IEEE, 67*, 1065,1073, 1979.

Dziewonski, A. M., and J. H. Woodhouse, Studies of the seismic source using normal-mode theory, in *Earthquakes: Observation, Theory, and Interpretation*, pp. 45-137, North-Holland, Amsterdam, 1985.

Eaton, J. P., Instrumental seismic studies, the Parkfield-Cholame, California earthquakes of June-August, 1966, *U.S. Geol. Surv. Prof. Paper 579*, 57-65, 1967.

Eaton, J. P., M. E. O'Neill, and J. N. Murdock, Aftershocks of the 1966 Parkfield-Cholame, California, earthquake: a detailed study, *Bull. Seismol. Soc. Am., 60*, 1151-1197, 1967.

Ekstrom, G., Centroid-moment tensor solution for the April 24, 1984 Morgan Hill, California, earthquake, The 1984 Morgan Hill, California, Earthquake, *Special Publication 68*, pp. 209-214, Calif. Div. of Mines and Geol., Sacramento, 1984.

Ellsworth, W. L., and S. M. Marks, Seismicity of the Livermore Valley, California region, 1969-1979, *U.S. Geol. Surv. Open File Rep., 84-515*, 1980.

Federal Emergency Managment Agency, An assessment of the consequences and preparatiohns for a catastrophic California earthquake – findings and actions taken: M & R-2, Washington D.C., 59 p., 1981.

Feng, R., and T. V. McEvilly, Interpretation of seismic reflection profiling data for the structure of the San Andreas fault zone, *Bull. Seimol. Soc. Am., 73*, 1701-1720, 1983.

Farra, V., P. Bernard, and R. Madariaga, Fast near-source evaluation of strong ground motion for complex fault models, in *Earthquake Source Mechanics, Geophys. Monogr. Ser., vol. 37*, edited by S. Das, J. Boatwright, C. Scholz, pp. 121-130, AGU, Washington, D.C., 1986.

Freund, L. B., The mechanics of dynamic shear crack propagation, *J. Geophys. Res., 84*, 2199-2209, 1979.

Fuis, G. S., W. D. Mooney, J. H. Healy, G. A. McMechan, and W. J. Lutter, Crustal structure of the Imperial Valley region, The Imperial Valley, California, earthquake, October 15, 1979, *U. S. Geological Survey Prof. Pap., 1254*, 377-384, 1982.

Fukuyama, E., and K. Irikura, Rupture process of the 1983 Japan Sea (Akita-Oki) earthquake using a waveform inversion method, *Bull. Seismol. Soc. Am., 76*, 1623-1640, 1986.

Gay, N. C., and W. D. Ortlepp, The anatomy of mining induced fault zones, 1, *Geol. Soc. Am. Bull., 90*, 47-58, 1979.

Haddon, R. and P. Buchen, Use of Kirchhoff's formula for body wave calculations in the Earth, *Geophys. J. Roy. Astron. Soc., 67,* 587-598, 1981.

Hanks, T. C., *b* values and ω-γ seismic source models: implication for tectonic stress variation along active crustal fault zones and the estimation of high-frequency strong ground motion, *J. Geophys. Res., 84*, 2235-2242, 1979.

Hartzell, S. H., Earthquake aftershocks as Green's functions, *Geophys. Res. Lett., 5*, 1-4, 1978.

Hartzell, S. H., and T. H. Heaton, Inversion of strong ground motion and teleseismic waveform data for the fault rupture history of the 1979 Imperial Valley, California earthquake, *Bull. Seismol. Soc. Am., 73,* 1553-1583, 1983.

Hartzell, S. H., and T. H. Heaton, Rupture history of the 1984 Morgan Hill, California, earthquake from the inversion of strong motion records, *Bull. Seismol. Soc. Am., 76,* 649-674, 1986.

Hartzell, S. H., and D. V. Helmberger, Strong motion modeling of the Imperial Valley earthquake of 1979, *Bull. Seismol. Soc. Am., 72*, 571-596, 1982.

Haskell, N. A., Total energy and energy spectral density of elastic wave radiation from propagating faults, *Bull. Seismol. Soc. Am., 54*, 1811-1841, 1964.

Haskell, N., Total energy and energy spectral density of elastic wave radiation from propagating faults, II, a statistical source model, *Bull. Seismol. Soc. Am., 56*, 125-140, 1966.

Haskell, N. A., Elastic displacements in the near-field of a propagating fault., *Bull. Seismol. Soc. Am., 76*, 59, 865-908, 1969.

Hays, W. W., Facing geologic and hydrologic hazards: earth science consideration, *U.S. Geol.Surv. Prof. Paper 1240-B*, 1981.

Heaton, T. H., and D. V. Helmberger, A study of the strong ground motion of the Borrego Mountain, California earthquake, *Bull. Seismol. Soc. Am., 67*, 315-330, 1977.

Hilterman, F. J., Amplitudes of seismic waves–a quick look, *Geophysics, 40*, 745-762, 1975.

Hong, T. L., and D. V. Helmberger, Glorified optics and wave propagation in nonplanar structure, *Bull Seismol. Soc. Am., 68*, 1313-1358, 1978.

Hubral, P., On the computation of shear waves by the ray method, *Geophys. J. Roy. Astron. Soc., 57*, 445-449, 1979.

Humphreys, E., R. W. Clayton, and B. H. Hager, A tomographic image of mantle structure beneath southern California, *Geophys. Res. Lett., 11*, 625-627, 1984.

Husseini, M. I., D. B. Jovanovich, M. J. Randall, and L. B. Freund, The fracture energy of earthquakes, *Geophys. J. R. Astron. Soc., 43*, 367-385, 1975.

Ida, Y., Cohesive force across the tip of a longitudinal shear crack and Griffith's specific surface energy, *J. Geophys. Res., 77*, 3796-3805, 1972.

Ida, Y., The maximum acceleration of seismic ground motion, *Bull. Seismol. Soc. Am., 63,* 959-968, 1973.

Ivanson, S., Remark on an earlier proposed tomographic algorithm, *Geophys. J. R. Astron. Soc., 75*, 855-860, 1983.

Jennings, C. W., Fault map of California, *Calif. Geol. Map Ser., map 1*, Calif. Div. of Mines and Geol., Sacramento, 1975.

Johnson, C. E., and Lk. K. Hutton, Aftershocks and pre-earthquake activity, The Imperial Valley, California, Earthquake, October 15, 1979, *U.S. Geological Survey Prof. Pap., 1254*, 59-76, 1982.

Kanamori, H., and J. Regan, Long-period surface waves, The Imperial Valley, California, Earthquake, October 15, 1979, *U.S. Geological Survey Prof. Pap., 1254*, 55-58, 1982.

Kanamori, H. and G. S. Stewart, Seismological aspects of the Guatemala earthquake of February 4, 1976, *J. Geophys. Res., 83,* 3427-3434, 1976.

Kawasaki, On the dynamical process of the Parkfield earthquake of June 28, 1966, *J. Phys. Earth, 23,* 127-144, 1975.

King, G. C. P., The accomodation of large strains in the upper lithosphere of the Earth and other solids by self-similar fault systems: the geometrical origin of the *b*-value, *Pageoph., 121,* 761-815, 1983.

Kostrov, B., Self-similar problems of propagation of shear cracks, *J. Appl. Math. Mech., 28*, 1077-1078, 1966.

Kostrov, B. V., and L. V. Nikitin, Some general problems of the mechanics of brittle fracture, *Arch. Mech. Stosow., 22*, 750-775, 1970.

Lanczos, C., *Linear Differential Operators*, pp. 100-162, D. Van Nostrand, New York, 1961.

Lay, T. and H. Kanamori, An asperity model of large earthquake sequences, in *Earthquake Prediction, an International Review, Geophys. Monogr. Ser., vol. IV*, edited by D. W. Simpson, and P. G. Richards, pp. 579-592, AGU, Washington, D.C., 1981.

Levenberg, K., A method for the solution of certain non-linear problems in least squares, *Quarterly of Applied Mathematics, 2*, 164-168, 1949.

Levy, N. A., and A. K. Mal, Calculation of general motion in a three-dimensional model of the 1966 Parkfield earthquake, *Bull. Seismol. Soc. Am., 66*, 405-423, 1976.

Lindh, A. G., and D. M. Boore, Control of rupture by fault geometry during the 1966 Parkfield earthquake, *Bull. Seismol. Soc. Am., 71*, 95-116, 1981.

Luenberger, D. G., *Linear and Nonlinear Programming*, pp. 277-304, Addison-Wesley, Reading, Mass., 1984.

Madariaga, R., Dynamics of an expanding circular fault, B*ull. Seismol. Soc. Am., 66,* 639-666, 1976.

Madariaga, R., High frequency radiation from dynamic earthquake source models, *Ann. Geophys., 1*, 17-23, 1983.

Madariaga, R., Earthquake source theory: A review, in *Earthquakes: Observation, Theory, and Interpretation*, pp. 1-44, North-Holland, Amsterdam, 1985.

Madariaga, R., and P. Papadimitriou, Gaussian beam modelling of upper mantle phases, Ann. Geophy., 6, 799-812, 1985.

Maruyama, T., On the force equivalents of dynamic elastic dislocations with reference to the earthquake mechanism, *Bull. Earthquake Res. Inst., Tokyo Univ.*, 41, 467-486, 1963.

Mayer-Rosa, D., Travel-time anomalies and distribution of earthquakes along the Calaveras fault zone, California, *Bull. Seismol. Soc. Am., 63*, 713-729, 1973.

McEvilly, T. V., W. H. Bakun, and K. B. Casaday, The Parkfield earthquakes of 1966, *Bull. Seismol. Soc. Am., 57*, 1221-1244, 1967.

McMechan, G. A., and W. D. Mooney, Asymptotic ray theory and synthetic seismograms for laterally varying structures, theory and application to the Imperial Valley, Califonia, *Bull. Seismol. Soc. Am., 70,* 2121-2035, 1980.

Michael, A.J., Effects of three-dimensional velocity structure on the seismicity of the 1984 Morgan Hill, California aftershock sequence, *Bull. Seismol. Soc. Am.*, 1199-1221, 1988.

Mooney, W. D., and R. H. Colburn, A seismic refraction profile across the San Andreas, Sargent, and Calaveras faults, west-central California, *Bull. Seismol. Soc. Am., 75,* 175-191, 1985.

Mooney, W. D., and J. H. Luetgert, A seismic refraction study of the Santa Clara Valley and the southern Santa Cruz Mountains, west-central California, *Bull. Seismol. Soc. Am., 72,* 901-909, 1982.

Mueller, C. S., D. M. Boore, and R. L. Porcella, Detailed study of site amplification at the El Centro strong motion array station 6, *Proc. on the Third Int. Conf. on Earthquake Microzonation, 1*, convened Seattle, Washington, 413-424, 1982.

Nabelek, J. L., Determination of earthquake source parameters from inversion of body waves, Ph.D. thesis, 346 pp., Mass. Inst. of Technol., Cambridge, 1984.

Niazy, A., An exact solution for a finite, two-dimensional moving dislocation in an elastic half-space, with application to the San Fernando earthquake of 1971, *Bull. Seismol. Soc. Am., 65,* 1797-1826, 1975.

Niazy, M., Source dynamics of the 1979 Imperial Valley earthquakefrom near-source observations (of ground acceleration and velocity), *Bull. Seismol. Soc. Am., 72,* 1957-1968, 1982.

Okubo, P. and K. Aki, Fractal geometry of the San Andreas fault system, *J. Geophys. Res., 92,* 345-355, 1987.

Okubo, P. G., and J. H. Dieterich, Effects of physical fault properties on frictional instabilities produced on simulated faults, *J. Geophys. Res., 89,* 5815-5827, 1984.

Olson, A. H., A Chebyshev condition for accelerating convergence of iterative tomographic methods - Solving large least squares problems, *Phys. Earth Planet. Inter., 47,* 333-345, 1987.

Olson, A. H., and J. G. Anderson, Implications of frequency domain inversion of earthquake ground motions for resolving the space-time dependence of slip on an extended fault, *Geophys. J. R. Astron. Soc., in press* 1988.

Olson, A. H., and R. J. Apsel, Finite faults and inverse theory with applications to the 1979 Imperial Valley earthquake, *Bull. Seismol. Soc. Am., 72,* 1969-2001, 1982.

Olson, A., J. Orcutt, and G. Frazier, The discrete wavenumber/finite element method for synthetic seismograms, *Geophys. J. R. Astron. Soc., 77,* 421-460, 1984.

Papageorgiou, A. S. and K. Aki, A specific barrier model for the quantitative description of earthquake faulting and the prediction of strong ground motion, I, description of the model, *Bull. Seismol. Soc. Am., 73,* 693-722, 1983.

Porcella, R. L., R. B. Matthieson, and R. P. Maley, Strong-motion data recorded in the United States, The Imperial Valley, California, Earthquake, October 15, 1979, *U.S. Geological Survey Prof. Pap., 1254*, 289-318, 1982.

Porter, L. D., Data processing procedures for mainshock motions recorded by the California Division of Mines and Geology strong-motion network, The Imperial Valley, California, Earthquake, October 15, 1979, *U.S. Geological Survey Prof. Pap., 1254*, 407-417, 1982.

Popov, M. M., and I. Psencik, Computation of ray amplitudes in inhomogeneous media with curved interfaces, *Studia Geoph. Geod., 22,* 248-259.

Prescott, W. H., N. E. King, and G. Guohua, Preseismic, coseismic, and postseismic deformation associated with the 1984 Morgan Hill, California, earthquake, *The 1984 Morgan Hill, California Earthquake, Spec. Pub. 68,* pp. 137-148, Calif. Div. of Mines and Geol., Sacramento, 1984.

Radbruch-Hall, D. H., Map showing recently active breaks along the Hayward fault zone and the southern part of the Calaveras fault zone, California, *U.S. Geol. Surv., Misc. Invest. I-813*, 1974.

Real, C. R., Ground rupture during the 1901 Parkfield earthquake, *EOS Trans. AGU, 66*, 982, 1985.

Rial, J. A., V. Pereyra, and G. L. Wojcik, An explanation of the USGS station 6 record, 1979 Imperial Valley earthquake: a caustic induced by a sedimentary wedge, *Geohys. J. Roy. Astron. Soc. Lon., 84*, 257-258, 1986.

Rice, J., Mathematical analysis in the mechanics of fracture, in *Fracture, Vol II*, H. Liiebowitz ed., pp. 191-311, Academic Press, New York, 1968.

Rice, J. R., The mechanics of earthquake rupture, in *Physics of the Earth's Interior,* Proceedings of the International School of Physics, pp. 555-649, North-Holland, Amsterdam, 1980.

Rice, J. R., and D. A. Simons, The stabilization of spreading shear faults by coupled deformation-diffusion effects in fluid-infiltrated porous materials, *J. Geophys. Res., 81,* 5322-5334, 1976.

Scholz, C. H., Scaling laws for large earthquakes, consequences for physical models, *Bull. Seismol. Soc. Am., 72,* 1-14, 1982.

Segall, P., and R. Harris, Earthquake deformation cycle on the San Andreas fault near Parkfield, California, *J. Geophys. Res., 92,* 10,511-10,525, 1987.

Segall, P. and D. D. Pollard, Mechanics of discontinuous faults, *J. Geophys. Res., 85,* 4337-4350, 1980.

Shakal, A. F., R. W. Sherburne, and D. L. Parke, CDMG strong motion records from the Morgan Hill, California earthquake of 24, April 1984, *Report 84-7,* Office of Strong Motion Studies, Sacramento, Calif., 1984.

Sharp, R. V., J. J. Lienkamper, M. G. Bonilla, D. B. Burke, B. F. Fox, D. G. Herd, D. M. Miller, D. M. Morton, D. J. Ponti, M. J. Rymer, J. C. Tinsley, J. C. Yount, J. E. Kahle, E. W. Hart, and K. E. Sieh, Surface faulting in the central Imperial Valley, The Imperial Valley, California, Earthquake, October 15, 1979, *U.S. Geological Survey Prof. Pap., 1254,* 377-384, 1982.

Shaw, P. R. and J. A. Orcutt, Waveform inversions of seismic refraction data and applications to young Pacific crust, *Geophys. J. Roy Astron. Soc., 82,* 375-414, 1985.

Sibson, R. H., Rupture interaction with fault jogs, in *Fifth Maurice Ewing symposium on earthquake source mechanics, series 6,* S. Das, J. Boatwright, C. Scholz eds., 157-167, 1986.

Sieh, K. E., Central California foreshocks of the great 1857 earthquake, *Bull. Seismol. Soc. Am., 68,* 1731-1749, 1978.

Singh, J. P., The influence of seismic source directivity on strong ground motions, *Ph.D. Dissertation,* University of California, Berkeley, California, 1981.

Smith, S. W., and M. Wyss, Displacement on the San Andreas fault subsequent to the 1966 Parkfield earthquake, *Bull. Seismol. Soc. Am., 58*, 1955-1973, 1968.

Spakman, W. and G. Nolet, Imaging algorithms, accuracy, and resolution in delay time tomography, in *Mathematical Geophysics*, 155-188, D. Reidel, Dordrecht, 1988.

Spudich, P. K. P., The DeHoop-Knopoff representation theorem as a linear inverse problem, *Geophys. Res. Lett., 7*, 717-720, 1980.

Spudich, P., Frequency domain calculation of extended source seismograms, *EOS Trans. AGU, 62*, 960, 1981.

Spudich, P., and R. J. Archuleta, Techniques for earthquake ground-motion calculation with applications to source parameterization of finite faults, in *Seismic Strong Motion Synthetics*, pp. 205-265, Academic, Orlando, Fla., 1987.

Spudich, P. and E. Cranswick, Direct observation of rupture propagation during the 1979 Imperial Valley, California, earthquake using a short-baseline accelerometer array, *Bull. Seismol. Soc. Am., 74*, 2083-2114, 1984.

Spudich, P., and L. N. Frazer, Use of ray theory to calculate high-frequency radiation from earthquake sources having spatially variable rupture velocity and stress drop, *Bull. Seismol. Soc. Am., 74*, 2061-2082, 1984.

Swanger H. J., and D. M. Boore, Simulation of strong-motion displacements using surface-wave modal superposition, *Bull. Seismol. Soc. Am., 68*, 907-922, 1978.

Takeo, M., An inversion method to analyze the rupture process of earthquakes using near-field seismograms, *Bull. Seismol. Soc. Am., 77*, 490-513, 1987.

Tchalenko, J. S., Smiliarities between shear zones of different magnitudes, *Geol. Soc. Am. Bull., 81*, 1625-1640, 1970.

Tchalenko, J. S., and N. N. Abrameseys, Structural analysis of the Dasht-e Bayaz (Iran) earthquake fractures, *Geol. Soc. Am. Bull., 81*, 41-60, 1970.

Thurber, C. H., Earthquake locations and three dimensional structure in the Coyote Lake area, central California, *J. Geophys. Res., 88*, 8226-8236, 1983.

Toppozada, T. R., Questioning the regular recurrence of Parkfield earthquakes, *EOS Trans. AGU, 66*, 982, 1985.

Trifunac, M. D., and F. E. Udwadia, Parkfield, California, earthquake of June 27, 1966: a three-dimensional moving dislocation model, *Bull. Seismol. Soc. Am., 64*, 511-533, 1974.

Tsai, Y. B., and K. Aki, Simultaneous determination of the seismic moment and attenuation of seismic surface waves, *Bull. Seisol. Soc. Am., 59*, 275-287, 1969.

Tse, S. T., R. Dmowska, and J. R. Rice, Stressing of locked patches along a creeping fault, *Bull. Seismol. Soc Am., 75*, 709-736, 1985.

Tucker, B. E., and J. L. King, Dependence of sediment filled valley response on input amplitude and valley properties, *Bull. Seismol. Soc. Am., 74*, 153-165, 1984.

Uhrhammer, R. A., and R. B. Darragh, The 1984 Halls Valley (Morgan Hill) earthquake sequence: April 24 through June 30, *The 1984 Morgan Hill, California Earthquake, Spec. Pub. 68*, pp. 191-208, Calif. Div. of Mines and Geol., Sacramento, 1984.

Vidale, J. E., and D. V. Helmberger, Elastic finite-difference modeling of the 1971 San Fernando, California earthquake, *Bull. Seismol. Soc. Am., 78*, 122-141, 1988.

White, B. S., R. Burridge, A. Noriss, and A. Bayliss, Some remarks on the Gaussian beam summation method, *Geophys. J. Roy Astron. Soc., 89,* 579-636, 1987.

Wong, T.-f., Shear fracture energy of Westerly granite from post-failure behavior, *J. Geophys. Res., 87*, 990-1000, 1982.

Wong, T.-f. On the normal stress dependence of the shear fracture energy, in *Earthquake Source Mechanics, Geophys. Monogr. Ser., vol. IV*, edited by S. Das, J. Boatwright, C. Scholz, pp. 1-11, AGU, Washington, D.C., 1986.

Wu, R.-S., and A. Ben-Menahem, The elastodynamic near field, *Geophys. J. Roy. Astron. Soc., 81*, 609-621, 1985.

Yoshida, S., A method of waveform inversion for earthquake rupture process, *J. Phys. Earth, 34*, 235-255, 1986.